CHARLES UNIVERSITY IN PRAGUE

FACULTY OF MATHEMATICS AND PHYSICS

DOCTORAL THESIS

Structure and properties of thin silicon films for solar cells

Studied by combined atomic force microscopy

by

Ing. Tomáš Mates

Prague, V/2006

A dissertation submitted in partial satisfaction of the requirements for the post-graduate degree of Charles University, Prague, Czech Republic

Structure and properties of thin silicon films for solar cells.

Supervisor:

RNDr. Antonín Fejfar, CSc.
Institute of Physics, Academy of Sciences of the Czech Republic

Consultants:

prof. RNDr. Ivan Pelant, DrSc.
RNDr. Jan Kočka, DrSc.
Institute of Physics, Academy of Sciences of the Czech Republic

Referees:

prof. RNDr. Tomáš Šikola, CSc.
Institute of Physical Engineering, Faculty of Mechanical Engineering
Brno University of Technology, Czech Republic

prof. RNDr. Vladimír Čech, Ph.D.
Institute of Materials Science, Faculty of Chemistry
Brno University of Technology, Czech Republic

Prague, May 2006

Acknowledgements

The major part of this work was done at the Department of Thin Films, Institute of Physics, Academy of Sciences of the Czech Republic in Prague. This concerns mainly the measurement results as well as the preparation of some samples. Other samples (especially the low temperature series) were deposited at the Institute of Physical Electronics, University of Stuttgart, Germany and at the Toppan Research Institute of Toppan Printing Co., Japan.

First of all I would like to thank my supervisor, Dr. Antonín Fejfar for his guidance and support during the research and writing of this thesis.

I would like to thank RNDr. Bohuslav Rezek, PhD. for his thoroughness and patience during the introduction to the AFM measurement techniques and image processing. I want to express my thanks to Dr. Jiří Stuchlík for the preparation of samples and various technical assistance. I would also like to thank Dr. Christian Koch from Stuttgart University and Dr. Manabu Ito from Toppan Printing Co. for the preparation of their samples, which were used in this work.

I am very grateful to all my colleagues from the Department of Thin Films who provided their results and contributed to the completion of this work. My thanks belong to Dr. Petr Fojtík for the SSPG measurements and help with LaTeX, Dr. Ha Stuchlíková for the conductivity and FT-IR measurements, Dr. Vladimír Švrček for the CPM measurements, Dr. Kateřina Herynková (Luterová) and RNDr. Martin Ledinský for the Raman measurements, Mgr. Ladislav Fekete for the help with AFM measurements, Mgr. Kateřina Kůsová for programming, Dr. Emil Šípek for the co-operation on combined AFM, Mgr. Kateřina Dohnalová for the assistance with chemicals, Dr. Vladimír Cháb, Dr. Jiří Slezák, Dr. Pavel Shukrynau, Mgr. Martin Švec and MSc. Aliaksei Vetushka for teamwork in the AFM laboratory. My big thanks go to our secretary Petra Šnajdrová.

I am also indebted to colleagues from other departments and institutions, especially to Ing. Ivo Drbohlav for the time he devoted to our AFM measurements, Dr. Karel Knížek for XRD measurements and his software Kalvados, Dr. Vladimír Vorlíček for the micro–Raman measurements, Dr. Anna Macková from Nuclear Physics Institute for the ERDA measurements, Andrea Mašková (Urbanová) from HVM Plasma for the help with Calotest experiment and Dr. Petr Klapetek from Czech Metrology Institute for his software Gwyddion.

I greatly appreciate the assistance of all colleagues during my stay in Japan in May 2003. First of all, I would like to mention my friend MSc. Shinya Honda, who devoted

me a lot of his time and later became an inspiring colleague at the Department of Thin Films. I also appreciate the co-operation of Dr. Manabu Ito, Kazuyoshi Ro and Shigenobu Yoneyama in the preparation of samples. Furthermore, I would like to thank Dr. Toshihiko Toyama, Dr. Riza Muhida from Osaka University and Dr. Chisato Niikura, Dr. Takuya Matsui, Dr. Hiroyuki Fujiwara and Prof. Akihisa Matsuda from AIST in Tsukuba.

It was a pleasure for me to have many fruitful discussions which stimulated my research activities. I gladly acknowledge the discussions with Dr. R.W. Collins from University of Toledo in Ohio on the evolution of roughness, with Dr. Julien Bailat, Dr. Corine Droz, MSc. Paula Bronsveld and Ondřej Čertík on the growth of μc–Si:H, with Dr. Michail Rakhlin from Stuttgart University and Dr. Pavol Šutta from University of West Bohemia in Pilsen on XRD measurements and with Dr. Sergej Filonovich on stress in the thin films.

My special thanks belong to Dr. Jan Kočka, head of the Department of Thin Films and all the laboratory staff for nice and friendly atmosphere.

Last, but not least, I would like to express great thanks to my parents, my wife and to the whole family for a great support during my doctoral studies.

Tuto práci věnuji svým prarodičům Josefu a Miroslavě Řeháčkovým ze Strašic za jejich vytrvalou podporu a obrovskou dávku životního optimismu. Dále ji věnuji své ženě Hedvice za vytvoření skvělého prostředí a za psychickou podporu.

Prague, May 2006 Tomáš Mates

Contents

1 Introduction 5
1.1 Photovoltaic solar energy conversion 5
1.2 Silicon solar cells 7
1.3 Outline of the thesis 9
Objectives of the thesis 10

2 Thin film silicon 11
2.1 Preparation by PECVD 12
2.1.1 Time 14
2.1.2 Temperature 15
2.1.3 Gases 16
2.1.4 Plasma 18
2.1.5 PECVD modifications 22
2.2 Preparation by other techniques 24
2.2.1 HWCVD 24
2.2.2 PVD 25
2.3 Macro–scale characterization 26
2.3.1 Thickness measurement 26
2.3.2 Conductivity measurement 26
2.3.3 Ambipolar diffusion length 27
2.3.4 Constant Photocurrent Method 29
2.3.5 Raman scattering 29
2.3.6 X-ray diffraction 32
2.3.7 ERDA and FT–IR 33
2.3.8 Calotest 34
2.4 Local probing 35
2.4.1 Micro Raman scattering 35
2.4.2 Atomic force microscopy 35
2.4.3 AFM image evaluation 37
2.4.4 Combined AFM 39
2.4.5 Cantilever artefacts 40
2.4.6 Cantilever force interactions 41

3 Study of microcrystalline silicon 43
3.1 Motivation 43
3.2 Structure of microcrystalline silicon 45
3.2.1 Cross-sectional measurements 45
3.2.2 Surface structure in AFM 47
3.2.3 Simple model of growth 50
3.2.4 Results of the model of growth 51
3.2.5 Anatomy of the grain 53

3.2.6 Surface roughness evolution 56
3.2.7 Growth process 57
3.2.8 Delayed nucleation 59
3.3 Properties of microcrystalline silicon 62
3.3.1 Local conductivity 62
3.3.2 Memory effect 63
3.3.3 Transport 64
3.3.4 Microcrystalline sample in detail 65
3.3.5 Guiding rule for μc–Si:H 67
3.3.6 Stress 68

4 Controlling the properties **73**
4.1 Motivation 73
4.2 Systemization of results 74
4.3 Substrates 75
4.4 Structure evolution in the thickness series at 250°C 76
4.4.1 Samples with r_H=21 (~4.5 % dilution) 77
4.4.2 Samples with r_H=32 (~3 % dilution) 82
4.5 Structure evolution in the thickness series at 75°C 88
4.6 Controlled transport in the dilution series at 80° C 94
4.7 Exploring the properties of the VHF temperature series 101
4.8 Exploring the properties of the RF temperature series 111
4.9 RF temperature series on plastic substrates 120
4.10 Test of increased deposition rate 122

5 Discussion **126**
5.1 General properties 126
5.2 Typical features of a–Si:H/μc–Si:H transition 127
5.3 Empirical estimate of the best sample 131

6 Final conclusions **132**

Bibliography **134**

About the author **150**
Curriculum vitae 150
List of publications 151

List of abbreviations and symbols:

Deposition	
RF, VHF	radio frequency (13.56 MHz), very high frequency
PECVD	plasma enhanced chemical vapor deposition
HWCVD	hot wire chemical vapor deposition
HPD	high pressure depletion
PVD	physical vapor deposition
$[H_2]$	gas flow of H_2 [sccm]
$[SiH_4]$	gas flow of SiH_4 [sccm]
c_{SiH_4}	silane concentration defined as c_{SiH_4}=[SiH_4]/([H_2]+[SiH_4])
r_H	hydrogen dilution defined as r_H=[H_2]/[SiH_4]
f_{exc}	excitation frequency of the plasma glow discharge [MHz]
P_{eff}	effective power coupled to the plasma: $P_{eff}=P_{applied}-P_{loss}$ [W]
p_{tot}	total chamber pressure [Pa]
r_d	deposition rate [nm/s]
t	duration of the deposition process [s]
T_S	substrate temperature [°C]
Properties	
AGS	average grain size (lateral) [nm]
α	optical absorption coefficient [cm^{-1}]
c_H	hydrogen content in the film [atomic %]
d	thickness of the deposited film [nm]
E_a	activation energy [eV]
γ	apex angle of the microcrystalline grain [°]
L_{diff}	ambipolar diffusion length by SSPG (parallel to the substrate) [nm]
L_{prec}	diffusion length of SiH_x precursors on the growing surface [nm]
σ_d	dark DC conductivity [$\Omega^{-1}cm^{-1}$]
σ_{ph}	photoconductivity [$\Omega^{-1}cm^{-1}$]
σ_0	dark DC conductivity prefactor σ_0 [$\Omega^{-1}cm^{-1}$]
σ_{RMS}	surface roughness by root mean square method [nm]
σ_r	total residual stress in the deposited film [GPa]
σ_{th}	thermal component of the residual stress in the film [GPa]
X_C	crystalline volume ratio [%]
V_{OC}	open circuit voltage of the solar cell [V]
J_{SC}	short circuit current of the solar cell [A]

Units	
W_p	Watt–peak (output of the solar module at standard conditions)
Materials	
a–Si:H	hydrogenated amorphous silicon
μc–Si:H	hydrogenated microcrystalline silicon
high p&P	sample prepared at high pressure and power
Measurement	
AFM	atomic force microscope
CPM	constant photocurrent method
d_{RCD}	Raman collection depth
ERDA	elastic recoil detection analysis
FT-IR	Fourier transform infrared spectroscopy
SEM	scanning electron microscope
SSPG	steady–state photocarrier grating technique
TEM	transmission electron microscope
XRD	X-ray diffraction
– (in tables)	no data (damaged sample, non–feasible measurement etc.)
Institutes	
FZÚ	Fyzikální ústav, Akademie Věd ČR, Praha
IoP (=FZÚ)	Institute of Physics, Academy of Sciences of the Czech Republic
AIST	Ntl. Inst. of Advanced Industrial Science and Technology, Tsukuba
FZ	Forschungszentrum, Jülich
IMT	Institute of Microtechnology, Université de Neuchâtel
IPE	Institut für Physikalische Elektronik, Universität Stuttgart
NREL	National Renewable Energy Laboratory, USA

Chapter 1

INTRODUCTION

Silicon – the most known and the 2nd most widespread element in the Earth crust – is still bringing new challenges. Although it is one of the most studied and used elements, there exist many open questions and there even may be some interesting properties or new forms of silicon we do not know about yet.

Thanks to the electronic industry and its rapid development in the second half of the 20th century, we can make our lives easier by enjoying a rich variety of electronic devices based on silicon components. The progress of these devices – increasing performance together with the decrease of their price – is mainly associated with the miniaturization and mass production, respectively. Both issues are of high importance. Miniaturization slowly brings the dimensions of some devices close to the nanometer–scale. By entering the field of nanotechnology we are in fact entering the world of new physical phenomena, most of which are still under intensive research. The mass production, on the other hand, causes a drastic decrease of the price, making most of the devices affordable.

1.1 Photovoltaic solar energy conversion

The increasing number of electronic devices produced by new technologies in highly industrialized countries lead to increasing energy demand. The ways of producing energy are, on the contrary, still very traditional – mainly based on burning fossil fuels like gas, oil or coal, with all negative effects involved. The increasing volume of greenhouse gases emissions and decreasing reserves of the fossil fuels do not meet the conditions for a sustainable growth, so the fast introduction of **renewable and environmentally friendly** energy supplies is inevitable. Solar, wind, hydro, geothermal and biomass energy are the major renewable sources expected to prevail over the fossil fuels in 30–50 years according to various energy scenarios, e.g. [1, 2]. Solar en-

ergy or photovoltaics (PV) has a big potential for a rapid growth, mainly because of its simplicity and worldwide applicability. The only drawback is the initial price of commercially available solar panels. However, the decrease to $\sim$ 20% of the price in 1980 [3] already makes the solar energy a suitable solution for the remote areas with no electric network. This currently refers to almost 1.6 billion people, mainly in the developing countries. The total electric power-generation capacity (based on all available sources, including fossil fuels) installed worldwide was about 3500 GW in 2003 and it is expected to increase to almost 7000 GW in next thirty years [4]. Half of the new capacity will be installed in the developing countries, so the need for cheap and preferably renewable energy sources is obvious. Moreover, these countries typically have very good insolation conditions, which favours the solar energetics. According to the optimistic PV market scenario, almost 656 GW_p of total solar power can be expected by 2030 if very large scale PV systems in the deserts are used [2]. [1] The annual statistics of International Energy Agency [5] indicate an impressive growth of the solar energetics with 0.1 GW_p installed solar power in 1992 to almost 2.6 GW_p in 2004.

Due to the intensive research effort of many laboratories and the companies involved in this field, there are many stimulating facts concerning the solar research, development and industry, some of them listed below:

- Energy payback time [2] of crystalline or polycrystalline solar cells has decreased to about 2–4 years and just to 1–3 years for the thin film solar cells [6], while most of the producers guarantee their modules for 25 years.
- Impressive progress in the solar cell efficiency (see Table 1.1).
- Designs of the solar panels for integration into modern buildings (e.g. Solartec, Roth & Rau).
- Flexible solar cell modules for special applications (e.g. United Solar - space research, VHF Technologies - portable electronic charger).
- Very large area depositions ($\sim$1 m^2) for cheap thin film solar cells (Kaneka, Unaxis).

[1]It is customary to cite the generation power of PV systems in Watt–peak, i.e., peak power under standard conditions [5]. Due to the changes of illumination and weather conditions, the real output averaged over the installed solar panels is reduced almost by an order of magnitude.

[2]The period of active use when the solar panel produces the same amount of energy as consumed for its preparation.

1.2 Silicon solar cells

For a further successful progress of the solar energetics we still need a lot of innovations leading, above all, to the competitive price of the solar cells and solar panels. Comparison of energy payback times shows that the thin film solar cells have potential for achieving low costs. The significant reduction of the raw material needs and faster production time make them an attractive alternative to the crystalline Si solar cells, although the efficiencies are still much lower (see Table 1.1). The theoretical limit for the efficiency of the single junction crystalline silicon solar cell given by the energy of its band gap is around 27% [7]. The disordered structure of the material in thin film solar cells leads to much lower efficiencies, however a significant improvements can be achieved by the application of a multi layered structure of stacked cells. So, the efficiency increase still remains to be an important task for the solar cell research. In the Table 1.1 the record efficiencies of the laboratory solar cells are summarized as of May 2003. Besides crystalline Si and thin film Si solar cells, there are also efficiencies of other types of solar cells based on materials like gallium-arsenide (GaAs), cadmium-telluride (CdTe) or copper-indium-gallium-diselenide ($CuInGaSe_2$). These materials can have very good electrical and optical properties, but they are suitable only for special applications, because their limited resources on Earth could make their future mass production problematic.

Laboratory size solar cells typically have an area in the order of cm^2. The upscaling for the industrial production of thin film solar cells usually leads to much larger substrates. The typical modules available commercially offer lower efficiencies: for example 12–15% in the case of crystalline silicon and 6–8% in the case of amorphous silicon solar cells. Since the efficiencies of laboratory cells are approaching the theoretical values, the main improvement probably lies in reducing the gap between the efficiency of commercial modules and laboratory cells. Recently, Kaneka Corp. [13] has reported record efficiencies of large scale thin film modules on glass substrates 91×45 cm^2: 8.7% for amorphous Si and 11.3% for micromorph (hybrid) Si, which uses a tandem cell concept of stacked amorphous (top) a microcrystalline (bottom) solar cells introduced by IMT Neuchâtel in 1994 [15].

As for the special applications, thin film amorphous solar cells on flexible substrates [16] have shown their potential in the space research, since they provide very good specific power/weight ratio in the range of 350–1250 W/kg, while the crystalline cells do not exceed the 100 W/kg.

Table 1.1: *Maximum stable conversion efficiencies of laboratory cells at standard conditions [5]. If no source is indicated, then after [4].*

Triple junction (GaAs) concentrator cell	35.2% (Spectrolab)
Crystalline solar cells:	
Monocrystalline Si cell	24.7% (Univ. of New South Wales [8])
Multicrystalline Si cell	19.8% (Univ. of New South Wales [8])
Thin film solar cells:	
$CuIn(Ga)Se_2$ cell	18.2% (NREL)
CdTe cell	16.0% (NREL)
Single junction amorphous Si	9.5% (IMT Neuchâtel [9])
Triple junction amorphous SiGe	13.0% (United Solar [10])
Thin films by new technologies:	
Single junction microcrystalline Si	10.1% (Kaneka [11])
Single junction microcrystalline Si	9.4% (AIST Tsukuba, 140°C [12])
Micromorph (hybrid) Si	12.0% (Kaneka [13])
Thin film monocrystalline Si	16.6% (IPE Stuttgart [14])
Organic solar cells	4% (Princeton, NREL)

The flexibility of the solar panels significantly broadens the range of applications. This probably gave rise to the idea of 25 μm thin monocrystalline Si selfsupporting films produced by a special layer transfer technique [14], showing that the demand for highly efficient and cheap solar cells brings the crystalline and thin film technologies even closer than we could imagine few years ago.

Unless some novel types of the solar cells appear (e.g. thin film silicon with large microcrystalline grains acting as concentrators of light and electrical current [17]), the most perspective way how to reach higher efficiencies is the multilayer structure (like a–Si:H and a–SiGe:H in triple junction amorphous solar cell or a–Si:H and μc–Si:H in micromorph or hybrid solar cell), exploiting the different band gaps of each layer for enhanced light absorption in a wider spectral range. Low temperature deposition on cheap substrates and high–rate deposition processes are explored in order to lower the costs per module/panel.

The choice of favourite material for the low–cost solar panels could be quite different even in few years if some emerging types of solar cells reach higher efficiencies. This might be the case of the organic solar cells, claiming up to 60% reduction of costs due to simpler production technology. If we analyse the efficiency data in a time scale [4], it is clear that the organic solar cells copy the trend of the amorphous silicon

solar cells, but with a 20 years' delay. Similarly, the solar energy research, development and industry are again just 20 years delayed compared to the well established and prospering wind energy [18].

1.3 Outline of the thesis

The main goal of this thesis is to study the intrinsic layer (i–layer) used in the thin film silicon solar cells. Quality of i–layer has a major impact on the performance of thin film solar cells. As explained in previous paragraphs, we are motivated by the usage of thin silicon film in solar cells on cheap (and even flexible) substrates. So, we mainly focused on the characterization of films prepared at rather low substrate temperatures (from 250°C down to 35°C) by the conventional Plasma Enhanced Chemical Vapor Deposition (PECVD). Most emphasis will be put on the characterization of samples prepared under different deposition conditions with the aim to understand the relation between the complicated microstructure and electrical properties of these intrinsic layers.

After the short introduction above to the silicon thin films in the context of solar cells and renewable energy sources, we move on to the *chapter two* starting with the overview of the most common methods of preparation of silicon thin films (Sections 2.1 and 2.2). Then we briefly present the characterization methods of these films categorized by the size of the measured area. In Section 2.3 named "Macro-scale characterization" methods for the determination of overall conductivity, diffusion length, crystalline volume fraction, crystallographic orientation and other properties are presented.

The second group of techniques (Section 2.4) is devoted to local probing, so the micro-Raman scattering is introduced and a special attention is paid to the atomic force microscope (AFM) and its modification – conductive AFM. In this section we also suggest a novel method for the evaluation of the lateral size of grains from the AFM images. For a clear description of the function of the AFM, conductive AFM and image evaluation, this section already includes the results obtained by the author.

Next, the whole *chapter three* contains author's original results, which were selected and arranged with the aim to present the microstructure and growth of mixed–phase Si films. We also propose a simple model of growth of microcrystalline grains and we focus on local electronic properties and add some comments to the residual stress in thin Si films. The samples in this chapter were prepared by PECVD at IoP in Prague. This chamber is directly connected to the Omicron AFM/STM microscope

enabling the measurements of in–situ films, so the samples are named "Stm #", where the # sign stands for the sequential number of the deposition.

In order to understand and control the properties of the thin film solar cells, we attempted to study the properties of several series of intrinsic Si thin films prepared by conventional PECVD. We focused on the evolution of structure, influence of microcrystalline grains on the transport properties and the change of properties with decreasing substrate temperature. The samples were prepared in three different laboratories mentioned in each section. A complex characterization of these series was performed in our group using the methods introduced in chapter two and the results make up the whole *chapter four*. The author's contribution was in the characterization of these samples by AFM in different modes and creating the final interpretation of results obtained by all available techniques.

A more detailed discussion of these results, as well as some more experiments with higher deposition rate, can be found in the *chapter five*. In the *last chapter* (Final conclusions) the most important findings and interesting results of the thesis are summarized and author's personal opinion about an outlook in this field is presented.

Objectives of the thesis

- Understand the growth of the thin silicon films with microcrystalline structure.
- Understand the transport in the intrinsic silicon films and its relation to the microstructure.
- Explore the behaviour of thin intrinsic films at very low substrate temperatures.
- Discuss the influence of the deposition conditions leading to the growth of the most suitable structure of μc–Si:H based solar cells.

Chapter 2

THIN FILM SILICON

Both amorphous silicon and microcrystalline silicon represent a wider class of materials, with properties strongly dependent on the deposition conditions. Hydrogenated amorphous silicon (a–Si:H) can be prepared by PECVD from pure gaseous silane (SiH_4). It was reported [19, 20] that the utilization of silane diluted in hydrogen leads to the growth of a–Si:H containing less defects. Device quality a–Si:H can be characterized by electronic defect density below 10^{16} cm^{-3} and under optimized deposition conditions, it can be prepared by several technologies. Hydrogenated microcrystalline silicon (μc–Si:H) is on the other hand known for its complicated microstructure, which can significantly vary with all the deposition conditions like dilution, pressure, plasma and substrate temperature. All these parameters will be addressed within this chapter.

Hydrogen contained both in a–Si:H and μc–Si:H terminates silicon dangling bonds and thus passivates the defects. Its importance can be illustrated by comparison with the polycrystalline silicon (poly–Si) – a material with much larger grains (μm – mm) grown at higher temperatures (T_S=600–800° C) or cast from melt. Due to high T_S, poly–Si contains no hydrogen. Although the poly–Si has very large grains, there still exist many grain boundaries . The post-deposition hydrogen plasma treatment is necessary to deliver some amount of hydrogen to passivate defects at the grain boundaries and thus improve the electrical properties. This refers both to films prepared in the vacuum by Low Pressure Chemical Vapor Deposition (LPCVD) [21, 22] and recently also by Atmospheric Plasma Chemical Vapor Deposition (APCVD) [23].

Microcrystalline silicon became especially attractive after realizing the fact that it does not suffer from the light induced degradation. This effect observed for the first time by Staebler and Wronski [24], seems to be an inherent property of amorphous silicon and it leads to the decrease of the efficiency of a–Si:H based solar cells by 10–

30% of the initial (as-deposited) value. Stability of μc–Si:H became a big motivation for the exploration of its the properties as a competing or complementary photoactive material.

Thin silicon films (amorphous or microcrystalline) exhibit the photovoltaic effect only in the 'p–i–n' structure. The impurities in the doped 'p' and 'n' layers increase the recombination and the disorder reduces the mobility of the charge carriers. So, the 'i' (intrinsic) undoped layer is essential both for the generation of carriers and their subsequent separation [25]. High solar cell efficiency requires good light absorption and electrical transport in the i–layer. The utilization of a μc–Si:H as an active layer in the solar cell is not so straightforward for two basic reasons [26]:

- μc–Si:H is a material with indirect band gap → low absorption, quite thick films are necessary (∼2 μm)
- complicated microstructure of μc–Si:H films (grains and grain boundaries) can deteriorate the transport properties of the material

Although the physical processes occurring in the microcrystalline silicon thin films are not fully understood yet, the real solar cells exhibit a photovoltaic effect with relatively high efficiencies. Furthermore, the band gap of ∼1.1 eV provides an enhanced absorption in the infrared region compared to the amorphous silicon with wider band gap ∼1.7 eV. So, the combination of a–Si:H based top cell and μc–Si:H based bottom cell, denoted as micromorph or hybrid structure is the way to cheap and highly efficient solar cells.

Due to the lower absorption coefficient of the μc–Si:H thicker layers ∼2 μm of μc–Si:H are needed to match the current generated by the a–Si:H layers in the micromorph solar cells. Amorphous silicon provides a sufficient absorption already at the thickness of 0.5 μm. Comparison of real solar cells produced by Kaneka [13] shows that light induced degradation resulted in efficiency drops of 18% for a–Si:H or 8% for micromorph solar cells proving the beneficial effect of incorporation of μc–Si:H.

2.1 Preparation by PECVD

The Plasma Enhanced Chemical Vapor Deposition (PECVD) is a glow discharge technique, based on a decomposition of a source gas containing silicon by means of plasma. This method, first reported by Sterling and Swann in 1965 [27], has several key deposition parameters which strongly influence the structure and quality of the deposited films. Only a narrow space of parameters leads to the microcrystalline or

polycrystalline structure, otherwise the film grows as amorphous. The key parameters will be reviewed within the Sections 2.1.1–2.1.4. The samples presented in this thesis were prepared by the PECVD, so the influence of the deposition parameters on the film properties will be shown and discussed in the Chapters 4 and 5.

First thin films with microcrystalline structure were prepared by Vepřek and Mareček by the transport chemical vapor deposition (CVD) in 1968 [28]. The working gas was pure hydrogen, introduced into the chamber through the high frequency (28 MHz) discharge, passing by silicon in the solid phase, probably creating gaseous silane (SiH_4) or its fragments. The silane was then decomposed on the surface of the substrates held at 600° C forming a thin μc–Si:H film. Due to relatively high substrate temperature, the films were deposited on sapphire substrate. The utilization of the glow discharge for more effective silane decomposition in PECVD technique [29, 30] at the beginning of 80's allowed decrease of the temperature down to 100–500°C and preparation of the films on relatively cheap substrates like glass. The μc–Si:H films were firstly used as doped (highly conductive) contact layers exhibiting much smaller optical absorption than a–Si:H films. Application of the μc–Si:H as photogeneration layer was firstly reported by Lucovsky and Faraji [31, 32] and the entirely microcrystalline silicon solar cells were fabricated by the IMT Neuchâtel in 1994 [33] using the very high frequency PECVD (Section 2.1.4). Since then, many laboratories studied this type of photovoltaic material using various methods for the preparation of the i–layer. The main advantage of preparation of microcrystalline silicon by PECVD is the well developed technology, which is already being used in industrial applications of a–Si:H in thin film devices, amorphous Si-Ge solar cells or Thin Film Transistor (TFT) displays. Although the production of solar cell panels based on microcrystalline silicon (see the Kaneka results in the Chapter 1) has already started, the parameter space of PECVD and its modifications is not completely explored up to now.

The principle of the PECVD is schematically shown in Fig. 2.1 with the experimental configuration of the chamber at the Department of Thin Films, IoP, Prague. The source gas (silane diluted by hydrogen) is introduced into the deposition chamber, where the plasma glow discharge is initiated between two planar electrodes. The discharge is typically maintained by the AC voltage in the radio frequency range. Our in–house built PECVD system is equipped with Thamway T161-5068A RF amplifier and T020-5068A matchbox. The range of frequencies is 10–110 MHz and maximum power is 100 W. The planar electrodes are circular. The cathode with 7 cm in diameter is fed with the RF signal (13.56 MHz) resulting in a DC self bias of around -120 V, while the anode holding the substrates is kept floating. The electrode distance

KNIHOVNA MAT.-FYZ. FAKULTY
Knihovna Fr Záviský (fyz. odd.)
Ke Karlovu 3
121 16 Praha 2

was always kept at 1.8 cm. The anode can be resistively heated and the substrate temperature T_S is monitored by a calibrated thermoresistor Pt 100. The composition of the source gas mixture (silane and hydrogen) as the key parameter is described in Section 2.1.3. The total pressure during the deposition was typically in the range of 10–100 Pa, but can be increased for example for achieving very high deposition rates (see 2.1.3).

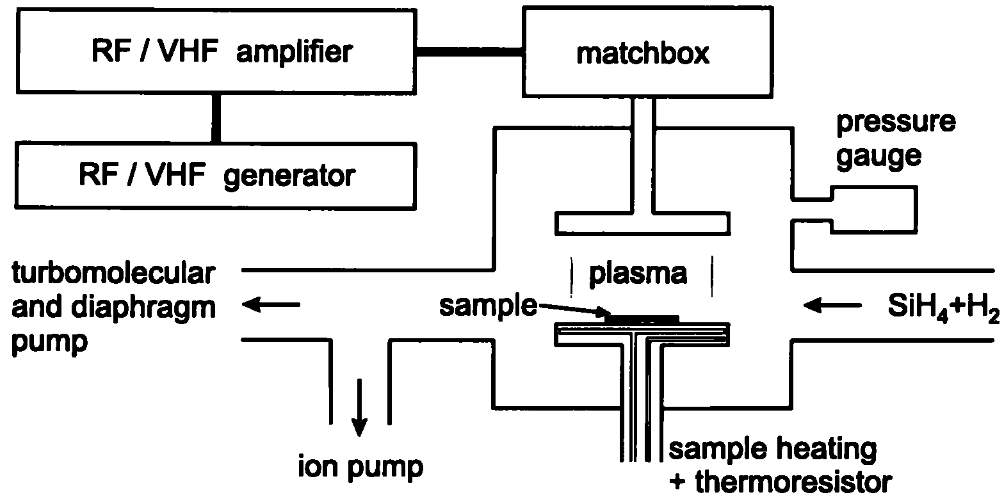

Figure 2.1: *Scheme of the PECVD deposition method.*

We will also show results of samples from other deposition systems used at Institute of Physical Electronics (IPE), University of Stuttgart and at Toppan Research Institute in Sugito-cho, Japan. These chambers are of the same type, capable of similar range of deposition parameters. The PECVD chamber in Toppan only differs in the cathode design – it is a shower electrode introducing the source gas mixture through the holes in the cathode. The shape is also circular with 6 cm in diameter.

2.1.1 Time

The duration of the deposition process is the simplest parameter, by which we influence just the thickness of the growing film. Deposition time is the ideal variable parameter for the preparation of a *thickness series*, i.e., the series of samples with different thicknesses. After the measurement of the film thickness, the deposition rate r_d can be evaluated:

$$r_d = \frac{d}{t} \quad [nm/s] \tag{2.1}$$

where:

- d thickness of the deposited film [nm]
- t duration of the deposition process [s]

The typical values of r_d for obtaining high quality μc–Si:H films are around 0.5 nm/s (the quality is reflected for example in the 9% efficiency of a single junction μc–Si:H solar cell). Just a small increase to $\sim$ 1.0 nm/s decreases the efficiency to 8% [34, 35] and it is supposed that with further increase of r_d the efficiency would decrease [36]. Recently, it has been reported that even at 3 nm/s, the efficiency of 8% can be achieved by conventional PECVD at high pressures [37] (Section 2.1.3). Very interesting is also the result of novel atmospheric plasma CVD method [38] obtaining deposition rates of 8 nm/s with an efficiency of 8.3%, but for the a–Si:H based solar cells. The parameters for the growth of microcrystalline structure by this method have probably not been studied yet.

The deposition of 2 μm thick i–layer at r_d=0.5 nm/s takes about 1 hour, while at r_d=10 nm/s the time needed for the preparation of the same layer drops down to $\sim$3 min. So, the increase of r_d while maintaining the quality of the films is an important goal for the PECVD based methods.

2.1.2 Temperature

The temperature of the substrate T_S is usually maintained by the resistive heating as shown in the Fig. 2.1. Before the deposition it serves for the cleaning purposes. Cleaning temperature is usually higher than the deposition temperature T_S in order to remove adsorbed species and prevent the contamination of working gases and growing thin film during the deposition process. The substrate temperature T_S has a direct impact on mobility of precursors on the surface promoting their diffusion, desorption and chemical reactions, thus influencing the structure and content of deposited thin film. To form the microcrystalline structure at lower temperatures, typically the dilution (Section 2.1.3) must be shifted to lower concentrations of silane.

For the amorphous silicon, the optimal substrate temperature was found to be around 250°C, where the defect density shows a minimum [39]. Similar temperature was also adopted for the deposition of microcrystalline silicon (e.g. [7]) and with decreasing T_S the defect density always increases [40].

T_S also influences the amount of hydrogen incorporated into the deposited film. This is one of the results being discussed in the Chapters 4 and 5, so here we just mention the fact that the amount of hydrogen increases with decreasing substrate

temperature both for amorphous silicon thin films prepared by PECVD [41, 42] and by HWCVD [43] as well as for μc–Si:H thin films prepared by PECVD [44, 45]. The bonding conditions and the total amount of hydrogen in the films are known to influence the light degradation of the a–Si:H thin films [41]: simply said – hydrogen seems to be responsible for the Staebler–Wronski effect.

However, for the industrial use of the cheapest plastic substrates (like polyethylene terephtalate – PET), the T_S ~250° C is still too high. Recently, an unexpected physical phenomena has been observed in connection with even lower substrate temperatures. Around the temperature of T_S ~140° C suppressed oxygen donor formation has been reported [12, 40, 46] by Nasuno et al. at AIST, Tsukuba. In these works the world record efficiency 9.4% of the single junction μc–Si:H solar cell has been achieved (Table 1.1). Schubert et al. at IPE, University of Stuttgart has extensively studied preparation of solar cells at very low deposition temperatures around and below 100° C, and also prepared the solar cell on plastic substrate at T_S=100° C with the efficiency of 6.3% [47]. Later it was also reported that even at temperatures around 80° C solar cells with high efficiencies can be prepared, when the deposition conditions are close to the boundary between a–Si:H and μc–Si:H growth [48].

2.1.3 Gases

Dilution

The composition of the source gas mixture is one of the key parameters of PECVD based processes. Usually, the dilution parameter is given as the concentration of silane c_{SiH_4} in the source gas:

$$c_{SiH_4} = \frac{[SiH_4]}{[H_2] + [SiH_4]} [\%] \tag{2.2}$$

where:

$[H_2]$ partial flow of the hydrogen [sccm]

$[SiH_4]$ partial flow of the silane [sccm]

To provide more graphical space in the region of small c_{SiH_4} values, which is of great interest since the a–Si:H / μc–Si:H transition occurs here, another measure of dilution – r_H is used [49]. The ratio r_H is defined as follows:

$$r_H = \frac{[H_2]}{[SiH_4]} \tag{2.3}$$

As seen from Eq. 2.3, the r_H is a dimensionless number. The exact relation between r_H and c_{SiH_4} is given by Eq. 2.4.

$$r_H = \frac{1 - c_{SiH_4}}{c_{SiH_4}} \approx 1/c_{SiH_4} \text{ (for } c_{SiH_4} \ll 1) \tag{2.4}$$

It has been reported that the utilization of silane diluted in hydrogen may bring beneficial effects to the structure and electronic properties of the wide band gap a–Si:H [50] as well of the standard a–Si:H [51]. The dilution ratio r_H between $5 < r_H < 13$ increases the band gap of the a–Si:H, while preserving its amorphous structure. At $r_H \sim 13$ some small crystallites may already appear in the film. Further increase of r_H (smaller concentration of silane c_{SiH_4}) leads to the change of the shape of crystallites. Firstly, the cones are observed at $r_H \sim 20$ and they are substituted by multiple columns separated by cracks at $r_H \sim 40$. At $r_H \sim 80$ the single columns over the whole film thickness are present. These r_H values refer to the work done at IMT Neuchâtel [52]. The other deposition conditions were T_S=225° C, plasma frequency 70 MHz, power of 7 W and pressure of 40 Pa. The observation of the transition between amorphous and microcrystalline growth is in agreement with results from other laboratories [49, 53, 54, 55].

Pressure

The typical total pressure in the PECVD method for the preparation of both amorphous and microcrystalline silicon thin films is in the range of 10–100 Pa [56]. At conventional deposition conditions (dilution, power) this results in relatively low deposition rate of about $r_d \leq 0.3$ nm/s. The increase of the r_d via higher plasma discharge frequency will be discussed in the Section 2.1.4. Another approach for achieving higher deposition rates lies in the employment of 2–5 times higher total pressure [57, 58], denoted as High–pressure silane–depletion (HPD) regime. Such a regime completely changes the processes in the plasma discharge, bringing more collisions among particles in the plasma and probably even creating some nanocrystalline clusters in the gas. The higher pressure further leads to the formation of narrower sheaths around the electrodes, thus reducing the energy of bombarding particles [59]. Besides the increased deposition rate, these effects may also beneficially promote the formation of the crystalline structure. The other important parameter closely connected to the pressure is the pd product [60]. The p is the total pressure and d is the distance between electrodes. Very high pressure p is used in HPD regime, where low enough electrode distance d as well as high enough plasma power must be set to prevent the powder formation [58, 61, 37, 62, 63].

Recent works of some laboratories show the results of the employment of the HPD regime: for example in the FZ Jülich [34] the pressure range from 200 up to 3000 Pa in the conventional RF PECVD system has been monitored and the pressure over 1000 Pa has been found necessary for high efficiency of the solar cells (over 8%) at high deposition rates r_d ~0.6 nm/s. The VHF PECVD system in IMT Neuchâtel [64] shows the deposition rate r_d ~2.5 nm/s and another VHF PECVD system in AIST Tsukuba [58, 65] even r_d ~3.8 nm/s for the deposition of the μc–Si:H thin film, both around the pressure of 300 Pa. However, the utilization of such an intrinsic layer in the solar cell required even higher pressures of ~ 900 Pa and resulted in the efficiencies of 8.2% at 2.1 nm/s or 7.9% at 3.0 nm/s [61, 37]. For comparison, the typical deposition rates of the samples within this work prepared by conventional PECVD are r_d ~0.2 nm/s at the pressure of 70 Pa (see Table 4.1).

2.1.4 Plasma

Power

The total power coupled to the plasma discharge has major impact on the decomposition and ionization of the source gas (silane and hydrogen). For a full description of the deposition conditions the value of plasma *power density* should be indicated. Power density is defined as the ratio of the plasma power over the area of the cathode. This parameter, taking into account the chamber geometry, characterizes the deposition conditions more precisely than just the value of plasma power and is thus essential for a meaningful comparison of samples prepared in different PECVD systems.

Under the conventional pressure conditions (see Section 2.1.3) the increase of the discharge power P_{eff} is usually reflected in the increase of the deposition rate r_d. By applying too high P_{eff}, the deterioration of the film crystallinity may occur [66, 67, 58], returning the microcrystalline growth back to amorphous. This is attributed to the bombardment by the high–energy particles created in the plasma with high degree of ionization [68]. To keep the high deposition rate for the growth of μc–Si:H and prevent the surface from this bombardment naturally leads to the increase of the total pressure in the HPD regime as shown in recent works [58, 37].

The typical values of the power density for the samples studied in this work were ~0.2 $W.cm^{-2}$. With the same equipment, the power density at the maximum available power 100 W would be roughly an order of magnitude higher.

As the powder formation at very high discharge powers is the main limiting factor for the further increase of the deposition rate, new ways of more effective plasma de-

composition are explored. Recently, an interesting result has been reported by AIST, Tsukuba using a novel design of cathode [62, 63]. It is shower head mesh electrode with a hollow-like discharge within the mesh. Improvements in the crystallinity as well as electrical properties have been achieved using the mesh electrode in the HPD regime (total pressure of 1240 Pa). The deposition rates reached 5.8 nm/s, however for the intrinsic μc–Si:H layer in the solar cell the r_d was decreased to 1.2 nm/s resulting in the efficiency of 8.1%. In August 2003, the $r_d \sim$10 nm/s has been announced for this type of deposition system [69]).

Frequency

As explained at the description of the PECVD principle at the beginning of this chapter, the plasma is usually generated in a capacitively coupled reactor by an AC electrical signal fed into the cathode. The standard excitation frequency f_{exc} of 13.56 MHz (denoted by RF PECVD) is sometimes substituted by very high frequencies (VHF PECVD) from 27.12 MHz to almost 200 MHz or even by microwave frequency 2450 MHz.

The excitation frequency f_{exc} has a major effect on the plasma discharge. Supposing the following conditions: conventional pressure ($\sim$ 70 Pa) and typical anode – cathode distance of 2 cm (both correspond to the typical deposition settings in our chamber), the frequencies f_{exc} >10 MHz cause the trapping of the positively charged ions "in the discharge", while the electrons having much higher mobility still follow the changes of the AC voltage. This trapping reduces the losses of ions (recombination on cathode) compared to a DC discharge and such a highly ionized plasma discharge provides enough reactive radicals to promote an effective deposition process. By applying the VHF frequencies f_{exc} >100 MHz, the same trapping effect occurs for electrons as they are prevented from reaching the electrodes. This leads to higher density of electrons within the discharge bringing more collisions with ions, thus producing high degree of ionization and making the whole deposition process more effective.

The first experiments with the VHF PECVD were done by Curtins et al. in IMT Neuchatel [70] in 1987 and a significant 5–10× increase of r_d in comparison with the conventional RF PECVD has been reported. The monotonic increase of the deposition rate with increasing f_{exc} has been then reported [71, 66, 47], reaching $r_d \sim$ 3.0 nm/s at f_{exc} =200 MHz. At higher frequencies f_{exc} more intensive ionization of the source gas occurs, reducing the impedance of plasma and thus enabling coupling of more power into the discharge. The enhanced ionization in the VHF range is attributed

either to the resonance effects as the excitation frequency f_{exc} becomes comparable with the frequency of electron collisions and neutral particles or to the interaction with the oscillating boundary of the cathode sheath as its effective velocity becomes comparable with the velocity of electrons (so called surf–riding of electrons). Further changes of the VHF plasma discharge include decreased sheath regions compared to RF discharge [72, 73]. This results in the reduction of the energy of ions impinging on the growing surface [47, 26]. This effect is independent of the chamber geometry and it was suggested [74, 75] that the values of excitation frequency $f_{exc} \geq 50$ MHz reduce the energy of the bombarding ions, thus preventing the formation of defects in the growing film. A similar effect can be achieved, to some extent, by a higher deposition pressure (see Section 2.1.3). Next consequence of the high degree of ionization at very high excitation frequencies f_{exc} is the increase of ion flux on the substrate [72, 73].

The comparison of f_{exc} =50 and 200 MHz [47] showed a substantial difference in the efficiency of the deposition process. Better gas utilization at higher excitation frequencies f_{exc} is also reflected in significant increase of the deposition rate r_d. The excitation frequency f_{exc} itself does not seem to have a major impact on the properties of the deposited film, this is mainly attributed to other parameters like pressure, power, dilution etc.

It should be noted that the proper impedance matching of the RF and VHF generator to the glow discharge is crucial for an effective transfer of the power ($P_{eff}=P_{applied}-P_{loss}$) into the plasma. Recent upgrade of our VHF PECVD equipment mainly focused on this problem. Several laboratories have reported the increase of r_d with increasing f_{exc}. However, the results significantly differ – both in the value of maximal r_d=1–3 nm/s) as well as in the f_{exc} of the maximal r_d (60–200 MHz) [47]. The common trend is the increase of r_d with increasing f_{exc} until the saturation is reached. This indicates the fact that all the silane precursors were decomposed (similar saturation of r_d is observed for increasing plasma power P_{eff}).

Finally, the trouble of the thickness inhomogeneity should be addressed, as this occurs mainly at the excitation frequencies f_{exc} above 60 MHz. When the VHF PECVD is up–scaled to the substrate dimensions of 1x1 m^2, the non-uniform film thickness may appear as a result of the interference of the VHF standing wave and cathode dimensions. The solution seems to be in a phase shifted multi–point feeding of the VHF power into the cathode to avoid standing wave formation. This does not refer to our PECVD system, since it is a laboratory size chamber with the electrode of 7 cm in diameter only.

Bias voltage

Basically, there are three possible settings of the bias voltage applied to the electrode with samples. In the following we suppose pressure ~10 Pa and RF discharge.

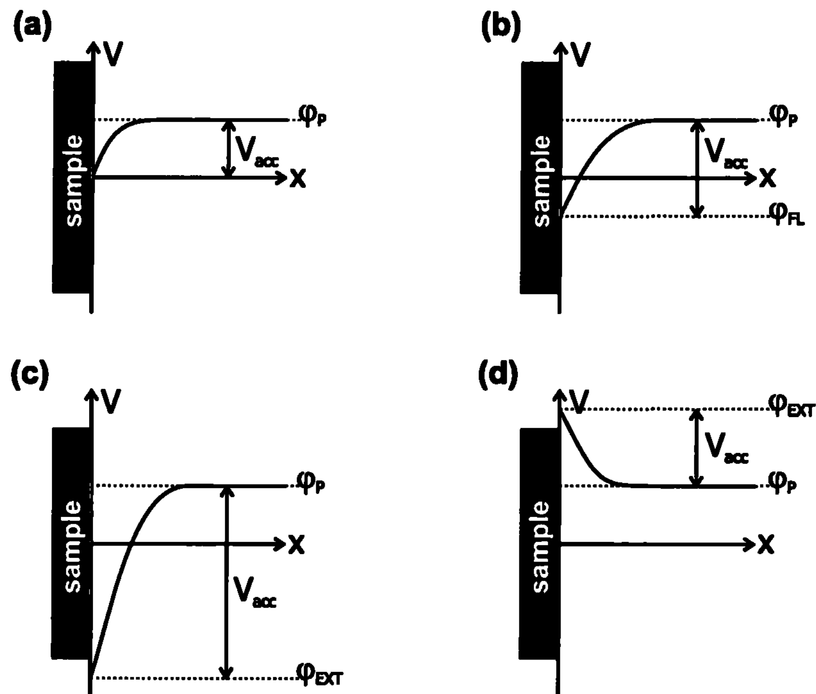

Figure 2.2: *Sketches of different potential distributions in the vicinity of the sample according to its electrical connection.*

- Firstly, the *electrode is grounded* – Fig. 2.2(a). The interaction of grounded substrate with the positive potential of plasma (φ_P) produces a **small voltage difference** in the order of tens of V depending on the values of power and pressure. The sample is then slightly affected by the bombardment of positive ions accelerated by the voltage $V_{acc} = \varphi_P$. The ion flux is relatively small since the whole chamber is typically grounded and serves as the anode too.

- Secondly, the *electrode is floating* – Fig. 2.2(b). In this setting the anode holding the samples is not electrically connected to any part of the deposition chamber. As in the case of an insulator, which develops negative potential due to different mobilities of electrons and ions in the RF discharge, the floating substrate is also charged up to a **negative** potential (φ_{FL}). The voltage $V_{acc} = \varphi_P$-φ_{FL} is then attracting the positive ions in the vicinity of the sample, which are known to have an effect on the film structure due to their higher mass.

- Thirdly, the *electrode is biased by an external source* – Fig. 2.2(c). In the case of a conductive substrate, the DC voltage source can be used. If a **negative** potential (φ_{EXT}) is applied to the substrate, it results in the same situation as described in the case of the floating electrode. Here, the effect of ion bombardment can be most pronounced, since the accelerating voltage is $V_{acc} = \varphi_P$-φ_{EXT} and can be precisely controlled.

  By applying the **positive** potential (φ_{EXT}) to the substrate, the ion bombardment of positive ions is suppressed and electrons prevail, accelerated by the voltage $V_{acc} = \varphi_{EXT}$-φ_P (Fig. 2.2(d)). Due to smaller mass of electrons, their bombardment does not affect the surface structure, but may slightly increase the substrate temperature. However, if the plasma is highly ionized and contains enough negative ions, they may also become an important factor influencing the structure of the growing film.

When the *substrate is not conductive*, only AC voltage (typically RF) can be applied, which leads to the formation of a negative voltage on the substrate surface, i.e., another cathode is introduced into the discharge. The final effect of the RF substrate bias is then comparable to the case of negative voltage on a conductive substrate. For all the samples in this work we used the floating sample setup (Fig. 2.2(b)). There was just one exception – sample Stm 108 (Section 3.2.7) was grounded.

It was reported [76, 77, 58] that the crystallinity of the films deposited by PECVD is sensitive to the potential difference V_{acc} between plasma and sample. The crystallinity has deteriorated at higher values of V_{acc} representing higher bombardment of positive ions.

However, there exist also other results on the influence of ion bombardment, reported for the conventional pressure values around 60–80 Pa. The energy of ions was found beneficial for the initial growth and formation of the crystalline structure [78, 79]. Yet these works refer to the crystalline volume fractions X_C between 20–50%, while the works in the previous paragraph refer to X_C between 60–90%. So, it seems that the ion bombardment is to some extent beneficial during the nucleation and film formation, while for the further growth it may not be needed.

2.1.5 PECVD modifications

The modifications of PECVD were developed for various purposes, typically to bring unique properties of deposited film or to excel in a certain deposition parameter.

That is why there are so many modifications available today, a detailed overview of which can be found for example in [36].

Modulating the amplitude of the VHF frequency by a square wave with frequency between 1–400 kHz is suggested for the prevention of powders [80, 81]. This approach was proposed by MVSystems, Inc. and is called Pulsed PECVD. The frequency of 68 kHz was found optimal concerning the properties of the films (efficiency of single junction nc–Si:H solar cell was 7.5%), while the deposition rate was increased up to 1.0 nm/s. Both authors claim much higher gas utilization ratio approaching 40% compared to about 15% for conventional continuous PECVD technique.

Closed chamber cyclic chemical vapor deposition (CCC-CVD) using standard PECVD discharge with additional feature – intermittent gas supply was also developed for more efficient gas utilization [82].

To promote the crystallization even at low temperatures and simultaneously obtaining relatively large grains, two step process called nanocrystal seeding NC–CVD [83] was proposed. In the case of [84], the very thin ($\sim$ 5 nm) μc–Si:H layer at very high r_H=300 (c_{SiH_4}=0.3%) was used to promote the formation of microcrystalline structure thus avoiding the amorphous incubation layer.

Atmospheric pressure PECVD with rotary electrode aims to reach very high deposition rates using a simple design avoiding the vacuum equipment. The deposition rate up to 10 nm/s can be reached [38].

Other modifications include methods like Electron Cyclotron Resonance CVD (ECR–CVD) or related Microwave PECVD (MW PECVD), Plasma Beam Deposition (PBD) using arc discharge, Ion Beam Deposition (IBD) operated at very low pressures etc. Post deposition techniques like Rapid Thermal Annealing, Pulsed Laser Annealing or Solid Phase Crystallization belong to another subgroup, where μc–Si:H is prepared by crystallization of a–Si:H film.

It is worth mentioning that our recent study of wide band gap a–Si:H films lead to an interesting finding – we succeeded in the crystallization of amorphous film at room temperature with the help of lateral electric field and presence of Ni upper electrode [85, 86].

2.2 Preparation by other techniques

2.2.1 HWCVD

One of the interesting alternatives of PECVD seems to be the hot–wire chemical vapor deposition (HWCVD) based on a catalytic decomposition of silane or silane + hydrogen mixture at a resistively heated filament. This method is sometimes also denoted as catalytic chemical vapor deposition (Cat-CVD). The introduction of HWCVD refers back to 1979, when it was proposed and patented by Wiesmann et al. [87]. Relatively simple setup is used for HWCVD: the source gas or mixture of gases is introduced along the resistively heated element at a temperature of ~1500 °C, where a catalytic cracking reactions occur and the reactive species are then transported to the substrate, where they contribute to the film growth. This method is also compatible with relatively low substrate temperatures $T_S \sim$ 150–400° C, so the utilization of cheap substrates like glass is feasible. The substrate is virtually free from ion bombardment and there are no major obstacles when scaling up the deposition system.

The possibility of relatively high growth rates r_d has attracted much attention and first device quality a–Si:H films have been reported in 1986 [88], but it took about a decade until the HWCVD a–Si:H solar cells have reached 10% initial efficiency [89]. The important question was the suitability of HWCVD for the preparation of high quality microcrystalline silicon thin films for solar cells. Recent HWCVD results of a n–i–p substrate type μc–Si:H based solar cell indicate the conversion efficiency of 9.1% [90, 91, 92]. During the exploration of HWCVD method some modifications appeared, similar to the modifications of PECVD. This is for example the two step process technique using two different dilution ratios. Firstly, a lower concentration of silane $c_{SiH_4} \sim$ 2% is used for the stimulation of the crystalline growth and after a certain time, the concentration is increased to $c_{SiH_4} \sim$ 5–8% to achieve higher deposition rate [93, 94].

The high growth rates r_d for HWCVD films were reported to be r_d=1.1 nm/s at 170–400 °C [95] or 0.85 nm/s at 200 °C and 1.1 nm/s at 500 °C [47]. These values were an order of magnitude higher than for conventional PECVD, but the previously described HPD regime of PECVD method (Section 2.1.3) has shown the same range of r_d.

2.2.2 PVD

The physical vapor deposition is based on a different principle. Instead of a chemical reaction, this technique exploits the physical processes, which are driven by the ionized particles in the plasma glow discharge – electrons and ions. Negative voltage applied to the electrode with source material in solid phase (Si wafer) causes the bombardment of positive ions. The material is thus sputtered and settles down to the chamber walls and also to the electrode with substrates optionally biased to attract the ionized species. Sputtering is in principle a non–equilibrium process, which means that films produced by this technique contain a lot of structural and electronic defects. This is not a big issue for highly conductive metallic films, but in the case of semiconductors it seems to be a major obstacle. However, the research of Si films prepared by PVD was motivated by the strong points of this method, i.e., high deposition rate r_d and easy up–scaling.

Magnetron sputtering with DC voltage was used in 1995 [96] for the preparation of polycrystalline silicon films with mean grain diameter of 40 nm at T_S=470° C. Since DC votage requires the usage of doped silicon target, for the production of i–layers, AC voltages of either RF [97, 98, 99, 100], VHF [101, 102] or microwave [103] frequencies were used. A different composition of working gas (Ar + H_2) is used for PVD instead of SiH_4 + H_2 for PECVD. However, the presence of hydrogen also facilitates the formation of crystalline structure at lower temperatures as in the case of PECVD.

There exist also various PVD modifications. Introduction of seeding layers made of μc–Si:H [96] or pure Cu [104] promotes the formation of crystalline structure. Utilization of pulsed DC source [105, 106] aims to achievement of high deposition rates r_d, which was supposed to be the main advantage of magnetron sputtering. However, reported values of r_d=0.2–1.5 nm/s are comparable with recent versions of PECVD employing VHF frequencies and HPD regime. Thus, one of the strong points of PVD simply vanishes.

2.3 Macro–scale characterization

To examine the properties of the deposited films we employ several macroscopic techniques. Overview of the diagnostics techniques used in our laboratory and typical results for a–Si:H and μc–Si:H can be found for example in [107, 108].

2.3.1 Thickness measurement

Routine measurement of thickness d for comparison purposes are often performed by surface profilometers. We used Tencor AlphaStep 100, which provides thickness d of deposited films with less than 10 % error. The measurement requires a clear step between the film and the substrate.

2.3.2 Conductivity measurement

One of the basic electronic characteristics of thin Si films is the value of dark conductivity σ_d. For the measurement of σ_d two coplanar stripes made of metal with a low work function (e.g. Ag, Cr or Ti) are evaporated (Fig. 2.3). The influence of the depleted region can be neglected for a–Si:H. The sample is placed into the vacuum chamber providing electrical and optical shielding. By applying DC voltage U the value of dark conductivity σ_d can be determined from Eq. 2.5:

$$\sigma_d = \frac{I_d w}{U l d}, \tag{2.5}$$

where I_d is the measured current, U the applied DC voltage, d the thickness of silicon film, w the distance between contacts, and l the length of the contacts. Fig. 2.3 shows the utilization of bottom contacts. They may give rise to inhomogeneous structure of the Si film, so it is useful to verify the σ_d also with the top contacts.

The measurement of σ_d is feasible only if the conductivity of the underlying substrate is much lower than σ_d of the Si film itself. This is valid for glass (Corning #7059) with typical dark conductivity around 10^{-14} $\Omega^{-1}cm^{-1}$. With the introduction of plastic substrates (PET, Section 4.9) we checked their native dark conductivity σ_d reaching the value of 10^{-13} $\Omega^{-1}cm^{-1}$, which is low enough to perform electrical measurements of deposited thin Si films typically exhibiting values in the 10^{-6}–10^{-7} or 10^{-9}–10^{-10} $\Omega^{-1}cm^{-1}$ range for amorphous or microcrystalline samples, respectively.

For thin Si films, a similar conductivity measurement at defined illumination conditions (AM1.5) can be performed, providing the value of photoconductivity σ_{ph} [56].

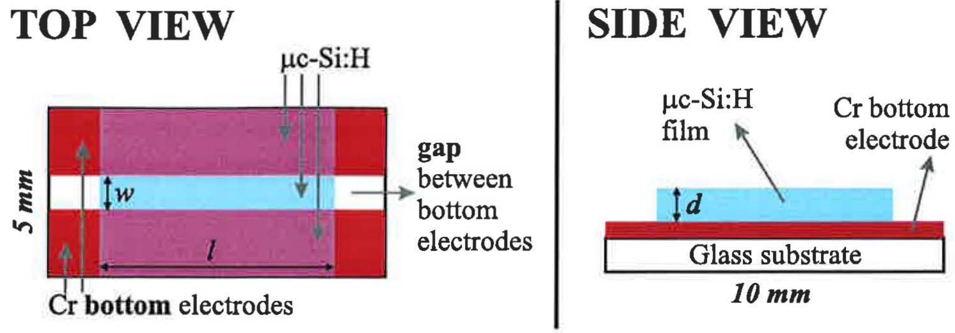

Figure 2.3: *Typical design of thin Si film sample deposited on glass with a pair of Cr bottom electrodes.*

This property is beyond the scope of this thesis and will be mentioned just briefly [109, 110] during the interpretation of results (Section 4.7).

Activation energy and conductivity prefactor

The value of σ_d itself does not provide much information about the electronic quality of the studied material. For a more precise estimation of the presence of impurities, the values of activation energy E_a and dark conductivity prefactor σ_0 are useful [56]:

$$\sigma_d(T) = \sigma_0 \exp(-E_a/kT), \tag{2.6}$$

where k is Boltzmann's constant and T is the absolute temperature.

Activation energy E_a of the dark conductivity σ_d indicates the energy difference between the Fermi level and the conduction or valence band for electron or hole transport, respectively. In the case of intrinsic material, the value of E_a should correspond to the half of the band gap value. Any shift of Fermi level caused by the impurities is thus reflected in the change of E_a. In Section 3.3.5 we propose a simple guiding rule (based on E_a and σ_0) for the estimation of quality of electronic transport in μc–Si:H.

2.3.3 Ambipolar diffusion length

The Steady–state Photocarrier Grating (SSPG) measurement [111] gives a very useful value of ambipolar diffusion length L_{diff}, which directly reflects the electronic transport in the thin film [112]. During the SSPG measurement (Fig. 2.4(a)), the sample is illuminated by two coherent light beams forming interference fringes on the sample. By the absorption of this light pattern, the sample contains periodically distributed areas with higher and lower carrier concentrations (Fig. 2.4(b)) affecting the photoconductivity of the sample. Diffusion currents driven by the concentration

gradient tend to blur this pattern. Electrons and holes move as neutral pairs in the presence of internal field (ambipolar diffusion). The diffusion process is furthermore limited by the lack of carriers and so the SSPG L_{diff} reflects the transport properties of minority carriers. These carriers are responsible for the photovoltaic effect in semiconductors and so L_{diff} can be used as a measure of the quality of the photovoltaic material, which is in close relation with the solar cell performance [113].

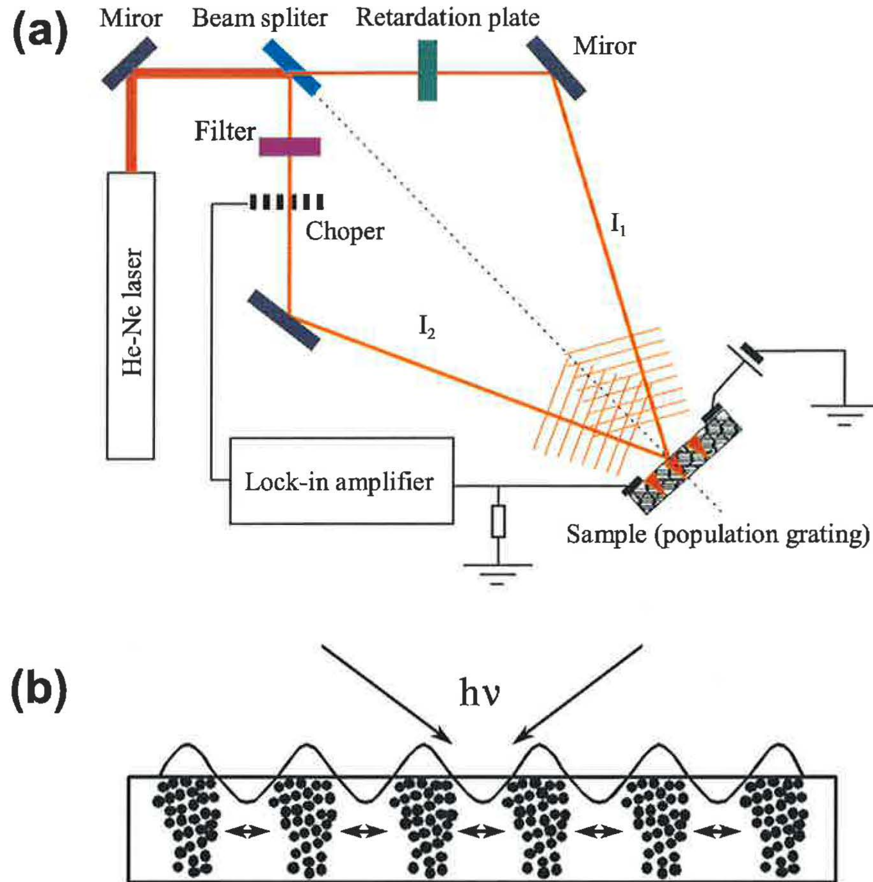

Figure 2.4: *Experimental arrangement of the SSPG method (a) and carrier grating inside the sample illuminated with two interfering beams (b).*

The L_{diff} of device-grade a-Si:H grown by PECVD is typically 100–150 nm, L_{diff} of μc–Si:H is slightly higher, typically in the range of 200–1000 nm [86].

SSPG measures the diffusion length L_{diff} parallel to the sample substrate. Another diffusion length – perpendicular to the substrate – can be measured by Surface Photovoltage (SPV) method [114]. In our group we compared values measured by SSPG and SPV in order to demonstrate the anisotropy of thin Si films [115]. Since the SSPG measurement is experimentally easier to perform and our recent results [116] on record μc–Si:H solar cells [117] indicate that a good photovoltaic material reveals

roughly identical values of parallel and perpendicular L_{diff}, we will use the L_{diff} by SSPG in the following chapters to demonstrate the quality of electronic transport.

2.3.4 Constant Photocurrent Method

Numerous methods provide the information about the density of states $N(E)$ within the band gap [56]. Constant Photocurrent Method (CPM) developed in our group at the Institute of Physics in Prague utilized the fact that the absorption coefficient α is proportional to $N(E)$. In photoconductive materials, like in thin Si films, σ_{ph} is in relation with the generation rate, which is further proportional to the product of α and light flux. By adjusting the light intensity to keep the σ_{ph} constant, the relative value of α is obtained [118]. Later, the concept of "absolute CPM method" [119, 120] was suggested, when both relative absorbance and the absorbance/transmittance ratio are detected simultaneously. The absolute scale of the absorption coefficient α is then obtained by using Ritter–Weiser formula [121]. Evaluation of the CPM spectra ($\alpha(E)$) provides two basic sample characteristics:

- Firstly, the states within the band gap indicate the presence of impurities. A measure of impurity level is provided by the value of α at certain energy ([118] suggests 1.2 eV , while [67] 0.8 eV).
- Secondly, the shape of the curve, i.e., direct visualization of the shape and position of the band edge can help to identify the structure, since the CPM spectra for crystalline Si, μc–Si:H and a–Si:H differ significantly [122].

2.3.5 Raman scattering

In case of a mixed–phase and fully microcrystalline Si, it is possible to estimate the crystalline volume fraction by using the Raman spectroscopy. The sample is illuminated by the laser light with a certain frequency, which undergoes an inelastic scattering generating phonon(s). The amount of energy loss is then reflected in the shift of frequency, which is characteristic of each material, its structure and chemical bonds.

The LO–TO phonons in the Raman spectrum of crystalline Si are indicated by a sharp peak around 520 cm^{-1}, while for the amorphous Si a much broader peak is found around 480 cm^{-1}. There are several slightly different procedures for the evaluation of crystalline volume ratio X_C. The a–Si:H and μc–Si:H parts in Raman spectra are fitted either with Lorentzian [75] or Gaussian [124, 125, 126] peak shapes and the

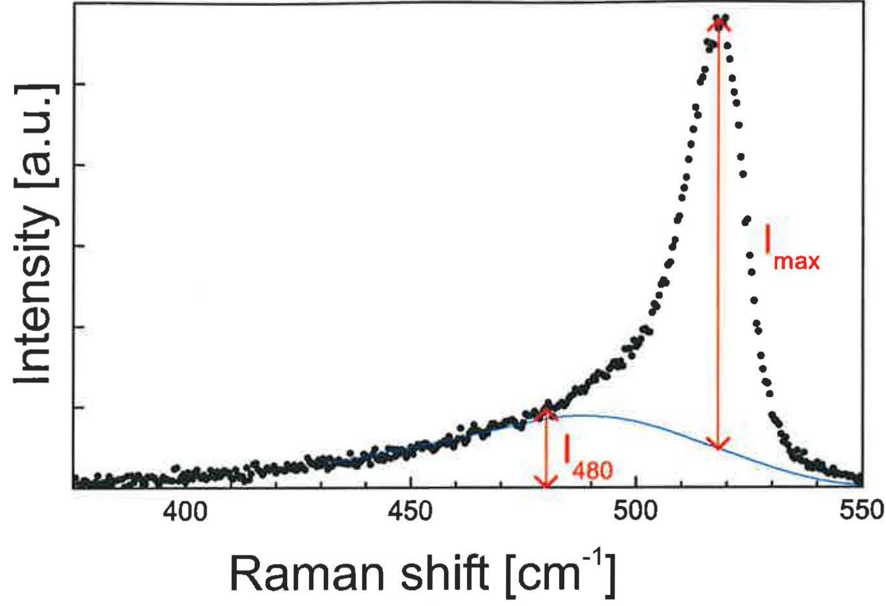

Figure 2.5: *Graphical illustration to the empirical evaluation of film crystallinity (Eq. 2.7) from the Raman scattering spectra. After [123].*

integrated intensities are put in the formula similar to Eq. 2.7. We have evaluated the crystallinity from peak height values at 480 cm^{-1} (I_{480}) and ~520 cm^{-1} (I_{max}) in the Raman spectra. The crystalline volume ratio X_C (also denoted as crystallinity) was calculated by the empirical formula 2.7 [127], graphically shown in Fig. 2.5, for all the samples in this work.

$$X_c = \frac{I_{max}}{I_{max} + 1.25 \times I_{480}} \tag{2.7}$$

where:

I_{max} crystalline phase contribution represented by the maximum ~520 cm^{-1}

I_{480} amorphous phase contribution taken as the intensity at 480 cm^{-1}

1.25 empirical correction coefficient taking into account the differences of their effective cross-sections in Raman scattering

The value I_{max} is always taken as the maximum value around 520 cm^{-1} with the subtracted amorphous contribution (Fig. 2.5), even if the peak is shifted to smaller or higher values. The I_{480} value represents the intensity of Raman signal at 480 cm^{-1}.

This procedure provides quite reliable results on highly crystalline films (X_C above ~60%) and is very easy to use. However, for samples with expected low crystalline fraction (X_C below ~60%) we obtained too high values, so the evaluation procedure using multiple Gaussian peak fitting is now under an intensive study [123, 128, 129].

There are two basic effects contributing to a possible shift of the crystalline peak around 520 cm^{-1}. The first one is the built–in microstress (residual stress), which is represented by dilated or contracted lattice parameter. Negative value of σ_r indicates compressive and positive σ_r tensile stress [130, 131].

$$\sigma_r[GPa] = -0.27(\omega_{max} - \omega_0)[cm^{-1}] \tag{2.8}$$

where:

σ_r total residual stress in the deposited film [GPa]

ω_{max} position of the maximum of crystalline peak

ω_0 position of crystalline peak for stress–free sample (c–Si wafer)

The second contribution to crystalline peak shift is caused by the phonon confinement effect in the small nanometer–scale crystallites present in the material [132, 133, 134]. Table 2.1 shows expected peak shifts as a function of size of crystallites after the model in [134]. The numbers demonstrate that the crystallites larger than ~10 nm have a minor impact on the shift of crystalline peak in Raman spectra.

Table 2.1: *Overview of crystalline peak shift in Raman spectra caused by the presence of small crystallites. After the model in [134].*

Crystallite size [nm]	2.2	3.0	4.0	6.0	8.0	10.0	20.0
Peak shift [cm^{-1}]	-5.69	-3.48	-2.20	-1.16	-0.73	-0.52	-0.17

Modified Raman setups may provide additional information, like bi–facial Raman measurement or utilization of different wavelengths with different penetration depths [135, 123, 128]. The penetration or Raman collection depth d_{RCD} is the maximum depth from which the signal is collected [136]:

$$d_{RCD}[nm] = \frac{10^7}{2\alpha[cm^{-1}]}, \tag{2.9}$$

where α is absorption coefficient for the given laser wavelength evaluated for example from CPM.

Taking into account the given value of d_{RCD}, the crystallinity X_C may not refer to the whole thickness of the Si film. The interpretation of X_C is even more difficult for mixed–phase samples [129], since the d_{RCD} is a function of α, which is different for a–Si:H and μc–Si:H. For all the Raman measurements within this work we used the continuous–wave argon ion laser at the wavelength of 514.5 nm (green), which provides a penetration depth d_{RCD} ~90 nm. For special purposes (Fig. 3.29) we performed the measurement with the wavelength of 647.1 nm (red) and d_{RCD} ~360 nm.

2.3.6 X-ray diffraction

For microcrystalline or polycrystalline samples, more information can be obtained about their inner structure than just one number X_C. X–ray diffraction (XRD) measurement is not commonly used for the detection of X_C, although such an evaluation procedure was proposed [137]. XRD is typically employed for the study of crystallographical orientation and estimation of crystallite size.

For the XRD measurements in this work we used the X–ray powder diffractometer Bruker D8 in Bragg–Brentano configuration [138]. The sample is exposed to the incident X–ray beam under the angle θ. If the Bragg's law is fulfilled (match of structural plane distance and angle θ with the X–ray wavelength), an elastically scattered (diffracted) beam with high intensity can be measured under the same reflection angle θ. During the measurement, a selected range of the angle θ is scanned and the intensity of the diffracted beam is recorded providing an XRD pattern. The positions of peaks in the XRD pattern are typical of each crystalline material.

Polycrystalline materials provide patterns with more peaks of different intensities indicating possible preferential structure. Typical peaks of μc–Si:H are (111), (220) and (311). The (220) seems to be the most suitable preferential structure with regard to the photovoltaic properties [56, 139].

A simple evaluation of the XRD pattern can be done by the Sherrer formula [138, 140], which attributes the broadening of peaks to the presence of crystallites smaller than ~200 nm.

$$D = \frac{k\lambda}{(2w)\cos\theta}, \tag{2.10}$$

where:

D	lateral dimension of an average crystallite
k	constant, $k = 2\sqrt{ln2/\pi} = 0.939437$
λ	wavelength of the incident X–ray, here: λ=0.154056 nm
$2w$	full width at half maximum of the diffraction peak
2θ	diffraction angle (position of the maximum of the Gaussian fit)

Since the Bragg–Brentano configuration provides the information about the crystalline structure only in the parallel plane to the substrate, the value D is a good estimate just for crystallites of spherical shapes. In the case of columnar, conical or needle-like crystallites, this D may be misleading.

The broadening of XRD peaks represents, in fact, two contributions – presence of small crystallites (D smaller than ~200 nm as in Eq. 2.10) and microstress σ which

is understood as dilatation or contraction of the lattice parameter, in other words microdeformation of the crystalline planes. It was suggested ([141] and references therein) that the presence of small crystallites is responsible for the Gaussian peak shape, while the microstress leads to the Cauchy shape peak broadening. The pseudo-Voigt function containing both components was proposed for more precise analysis of XRD peaks. After such a peak fitting (using e.g. [142]), the further evaluation aiming for the separation of both contributions (D and σ) is done by the construction of Williamson–Hall graph $Y_{WH} = f(X_{WH})$ [138]:

$$X_{WH} = \sin\theta \qquad Y_{WH} = \frac{(2w)\cos\theta}{\lambda} \tag{2.11}$$

The meaning of variables is identical with Eq. 2.10. From a linear fit of the plot $Y_{WH} = a + bX_{WH}$ the coefficients a and b are obtained and finally the crystallite size D and microstress σ can be evaluated:

$$D = \frac{k}{a} \qquad \sigma = eE_f = \frac{b\lambda}{4}E_f \tag{2.12}$$

where e is the micredeformation and E_f is the Young modulus of the film. For Si film we adopted the value E_f=169 GPa obtained for Si wafer [143]. All the XRD grain sizes in this work were obtained from Eq. 2.12

2.3.7 ERDA and FT–IR

The amount of hydrogen is another very important feature of deposited thin Si films. The key effect of hydrogen on structural and electronic properties will be shown and discussed in detail in the next chapters. From the list of several methods used for the detection of hydrogen content c_H [56] we used the following ones:

Hydrogen content by FT–IR

Fourier–Transformed Infrared Transmittance (FT–IR) spectroscopy is the most common method used for the detection of hydrogen content c_H due to its experimental convenience. The c_H value is proportional to the integrated absorption coefficient at 640 cm^{-1} and provides the information about the amount of hydrogen, which is chemically bound in the studied material. Details of the experimental setup are given in [144].

Hydrogen content by ERDA

Elastic Recoil Detection Analysis (ERDA) is semi–destructive absolute method detecting all the hydrogen inside the film, i.e, including the molecular one. So, the values of c_H by ERDA are typically higher than the values of c_H obtained by FT–IR [53, 90]. The studied sample is irradiated with highly energetic heavy ions at grazing incidence scattering out the atoms of the sample. Identification of elements is based on various masses, which reveal different energies and times–of–flight in the detection system with fixed flight path.

2.3.8 Calotest

Calotest [145] is an easy mechanical trick to obtain the thickness profile on just one sample. A rotating sphere is pressed on the sample with the normal force derived from the weight of the sphere (Fig. 2.6(a)). The rotational motion of the sphere abrades the sample and creates a spherical crater. In the optical microscope image of the crater (Fig. 2.6(b)) the dark central area represents the substrate and the brighter ring the thin film. The unabraded surface of the thin film can be clearly identified due to its characteristic roughness which contrasts with the crater unidirectionally scratched due to the steel ball rotation.

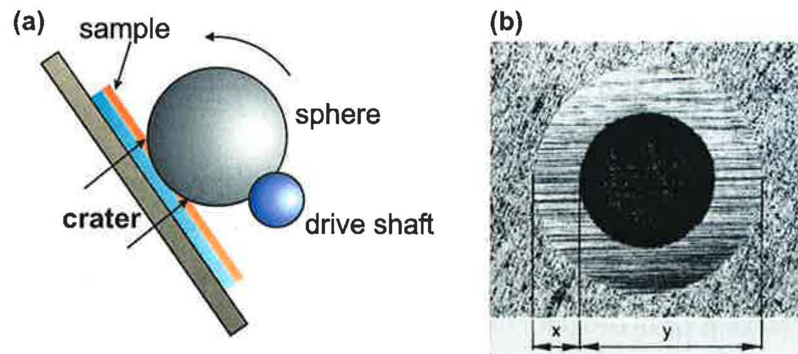

Figure 2.6: *Principle of the Calotest method (a) and top view on the crater created in the thin film. In our measurements, a sphere of 49 mm in diameter was used.*

2.4 Local probing

2.4.1 Micro Raman scattering

Micro–Raman represents a modification of standard Raman spectroscopy with beam focussed to a spot with 2 μm in diameter to study crystallinity at different positions on sample controlled by the optical microscope. We have exploited this method during the study of the depth profile obtained by Calotest (Section 3.2.1).

2.4.2 Atomic force microscopy

Atomic Force Microscope (AFM) introduced by Binnig et al. in 1986 [146] is the main diagnostic technique used in this work. AFM belongs to a large family of scanning probe microscopes that gradually evolved from the first one – Scanning Tunneling Microscope (STM) introduced by Binnig and Röhrer in 1982 [147].

AFM provides illustrative topography information about the surface of almost any type of material within the field of view from $\sim$100$\times$100 μm down to the atomic level. The principle of the AFM microscope is shown in Fig. 2.8. The sample is scanned by a small cantilever holding a sharp tip. Typical length of the cantilever may vary between 100–300 μm and its width about 30 μm. At the end of the cantilever is a pyramidal tip approximately 15 μm high, with the apex angle around 25°. Such a microprobe is sensing attractive or repulsive forces of different origin (atomic, electrostatic, magnetic) in the order of 10^{-9} – 10^{-5} N causing its deflection. The deflection is most often detected by the laser beam reflected from the back side of the cantilever onto a position sensitive detector. During the measurement the sample or cantilever is moved in X–Y plane by piezoelectric actuators. The whole image is then created in the computer by putting line–scans together.

The simplest AFM measurement is the contact mode measurement based on repulsive forces when the cantilever (13-75 kHz, see Table 2.2) and the sample are in the direct contact. The AFM measurement can be also performed in non–contact or semi–contact (tapping) mode utilizing more advanced detection of interaction forces. Here, the cantilever is oscillated close to its resonance frequency (75–330 kHz) and the shift of frequency or amplitude of these oscillations is monitored.

Standard contact mode AFM measurement produces two signals – *Local height* obtained as the motion of Z–piezo element compensating for the surface protrusions during the scan. Due to electronic and mechanical imperfections of the feedback loop, not all the surface protrusions are reflected in the Z–piezo signal, so the cantilever

exhibits also some deflection, which is then plotted as the *Deflection, Normal force* or *Topography.* The proportion of data between these two signals can be adjusted by the feedback loop gain. In the case of high gain the measurement is close to the ideal constant–force mode, while with very low gain it approaches the ideal constant–height mode.

The deflection signal image resembles the surface structure being illuminated from the left or right, depending on the scan direction. Similar image can be also obtained directly from the local height image by applying partial derivation along the X–axis. All the AFM images in this work are shown in the deflection signal due to its illustrative character.

The optical detection of the cantilever deflection is the most common and convenient one. Although it provides high precision, the cantilever and sample are exposed to quite intensive illumination, which may produce artefacts (e.g. in electrical measurements [148]) when semiconductor cantilevers are employed. This is, unfortunately, the case of most commonly used cantilevers – they are micromachined from Si or Si_3N_4 [1]. The overview of basic types of cantilevers provided by a major manufacturer is given in Table 2.2. There exist cantilevers with different lengths and spring constants suitable for different measurement modes as summarized in Table 2.2. All the types of cantilevers can optionally have a reflective coating on the back side (typically made of Al), ~25 nm thick conductive coating made of Pt or wear resistant ~100 nm thick diamond coating and many more.

Table 2.2: *Overview of different types of cantilevers used in the AFM. Typical cantilever specifications are provided by the manufacturer.*

Canti-lever type	Length [μm]	Width [μm]	Thickness [μm]	Spring constant [N/m]	Resonance frequency [kHz]	Application
Cont	450	50	2	0.2	13	Contact mode
FMR	225	28	3	2.8	75	Force modulation
NCL	225	38	7	48	190	Non-contact mode
NCH	125	30	4	42	330	Non-contact mode

[1]Today, there are about 20 producers of various AFM cantilevers worldwide, see for example www.nanosensors.com.

2.4.3 AFM image evaluation

For the evaluation purposes, the AFM topography pictures are usually processed to provide some numerical characteristics of the surface. Most often, the standard RMS roughness (Root Mean Square) defined by Eq. 2.13 [149] is evaluated:

$$\sigma_{RMS} = \sqrt{\frac{\sum_{i=1}^{N}(Z_i - Z_\phi)^2}{N}} \quad [nm] \tag{2.13}$$

where:

N number of the data points in the measured image

Z_i absolute height at the ith point [nm]

Z_ϕ average height of all the data points in the measured image [nm]

The number N indicates the fact that the AFM images are, regrettably, limited to a certain number of data points given by the measurement settings and the microscope hardware and software capabilities. Typical resolutions used in this work are 400×400 points in the case of the images by UHV AFM microscope and 256×256 points for the ambient AFM microscope images.

The σ_{RMS} value characterizes the surface in the vertical scale only. There may exist surfaces with similar σ_{RMS} values (samples with thickness 200 nm and 1500 nm in Fig. 4.4), but having very different structures. The need for an additional value characterizing the lateral structure is obvious. There is, unfortunately, no standard method yet, so various definitions of different characteristics can be found in the literature [46].

Since the surfaces of a–Si:H and μc–Si:H films exhibit rather flat amorphous background and circular protrusions of μc–Si:H grains, we attempted to characterize the grains by their typical diameter size. Most suitable method for this seems to be the utilization of Power Spectral Density Function (PSDF) obtained as a result of the Fast Fourier Transformation (FFT) of the AFM local height image. The one–dimensional PSDF plot is obtained by using the radius in reciprocal space as the spatial frequency and radially averaging the two–dimensional FFT image [149]. The PSDF can be used for the characterization of lateral dimensions of surface structures [150, 151] and is often provided as built–in function of the software for AFM image processing [152]. Significant peaks in the PSDF plot correspond to dominant surface features (Fig. 2.7(a)) as they were decomposed into certain frequencies during the FFT procedure. The assignment of the peaks to real lateral dimensions is given by

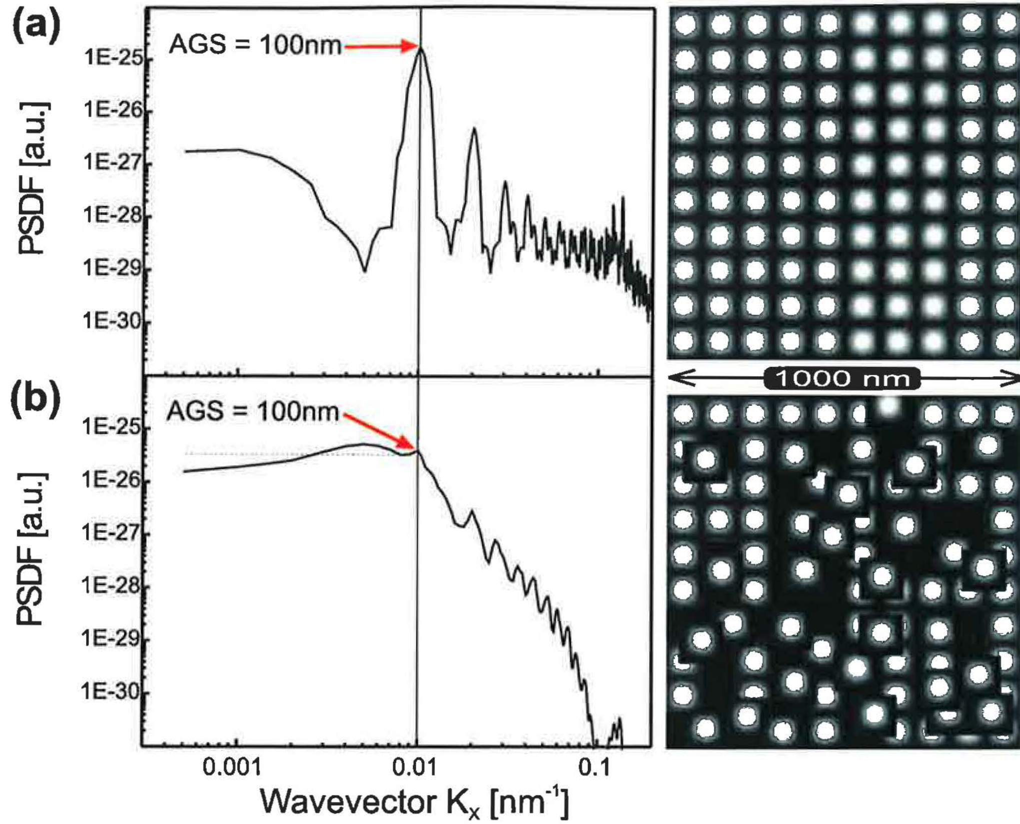

Figure 2.7: *Determination of AGS from PSDF plots of two synthetic surfaces. Values on the X-axis are already divided by the factor of $2\pi 10^9$ (see Eq. 2.14)*

Eq. 2.14. For the characterization of our thin Si films we denote this typical lateral feature as average grain size (AGS):

$$AGS = 2\pi.10^9/K_{AGS} \qquad [nm] \tag{2.14}$$

where:

AGS	average grain size [nm]
K_{AGS}	wavevector value of the significant peak in PSDF

In the case of surfaces with randomly distributed grains the lower frequencies may exhibit a plateau in the log-log plot of PSDF. The significant peak of dominant surface features is found close to the high-frequency-end of this plateau, where the PSDF values start to decrease (Fig. 2.7(b)).

Due to the fact that the AFM image is sampled by a limited number of data points, the PSDF has a given bandwith. The largest detectable feature corresponds to the scan size and the smallest one is given by (scan size) / (half of data points).

For example, the minimal feature, which can be revealed by a 1 μm scan with 400 data points, is 1000 nm/(400 pts/2)=5 nm.

2.4.4 Combined AFM

There exist numerous variations [153] of the scanning probe microscope based on the detection of different signals. For the characterization of electrical properties on nano- or micro-scale with direct correlation with topography features, the concept of combined AFM is suitable [154]. The measurement principle is quite simple: besides the standard AFM topography measurements, the STM electronics is employed, thus "combined AFM". The cantilever, which must be conductive, is scanning in contact mode the topography of the sample and simultaneously detecting the current passing through the sample. The most critical part is the amplification of very small current signals. To highlight the capability of the instruments, some manufacturers (Veeco) call this combined mode Conductive AFM (C–AFM) or Tunneling AFM (TUNA), when current values are sensed in nA or pA range, respectively.

Basic requirements of combined AFM are conductive cantilevers (standard Si cantilever with conductive PtIr coating, highly doped Si cantilevers also work for highly conductive samples) and sample with an electrode. In the study of thin Si films we used the bottom electrode (Fig. 2.8) to probe the electrical properties perpendicular to the substrate.

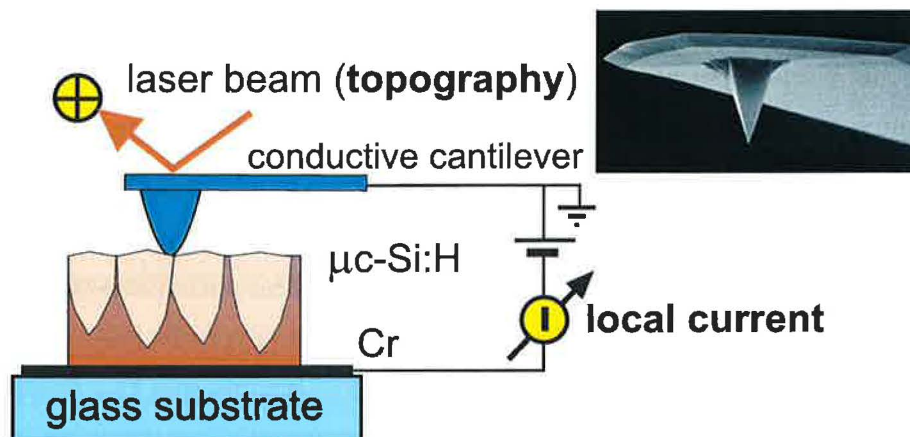

Figure 2.8: *Principle of the combined Atomic force microscope and SEM image of the pyramidal tip.*

This means that the topography and local current images obtained by combined AFM always show the thin Si film *on the bottom electrode.* Here, the film may not reveal the same structure as the film grown directly on glass (Figs. 4.13 & 4.14).

The topography images by air AFM were measured *between the bottom electrodes* (Fig. 2.3). These standard topography images refer to the proper part of the sample, which is characterized by other techniques, and so they were then used for the evaluation of RMS roughness. The combined AFM images provide only an additional information about the structure local electrical properties of the film grown on the electrode. The AFM images in this work were obtained at IoP in Prague by Veeco Explorer (air AFM) or by Omicron UHV AFM/STM (combined AFM, Fig. 2.9).

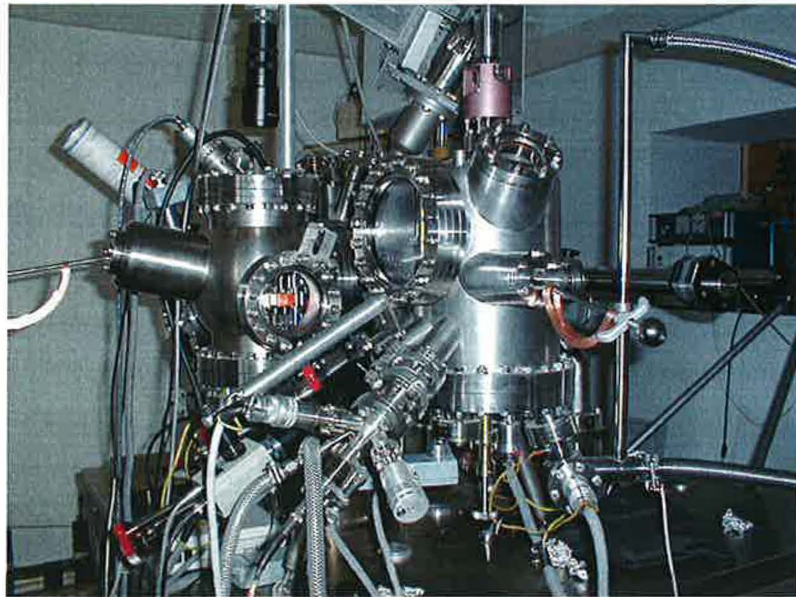

Figure 2.9: *View of the ultra high vacuum apparatus, which includes AFM and STM microscopes (Omicron) connected to the in–house built PECVD deposition chamber.*

2.4.5 Cantilever artefacts

The brand new cantilever should provide a lateral resolution of ~10 nm – this is the standard tip radius guaranteed by the manufacturers. Every further coating increases the radius. During the scanning, the tip typically becomes less and less sharp, which is reflected in appearance of doubled edged, pyramidal or other suspicious features repeating in the scanned image. When this happens, the cantilever must be replaced, because there is no way to sharpen the tip again.

However, during the measurements we experienced a few exceptions. The cantilever may attach some adsorbates or clusters at the end of its pyramidal tip by scanning some soft or dirty surface. This decreases the resolution of the final image. By chance, we observed an unusual effect – sharpening of the tip by scanning, see

Fig. 2.10. By scanning over a bigger protrusion (e.g. μc–Si:H grain) the adsorbed clusters of material were removed and the original sharpness of the cantilever restored as seen again in the upper part of Fig. 2.10 exhibiting much better resolution on the amorphous tissue.

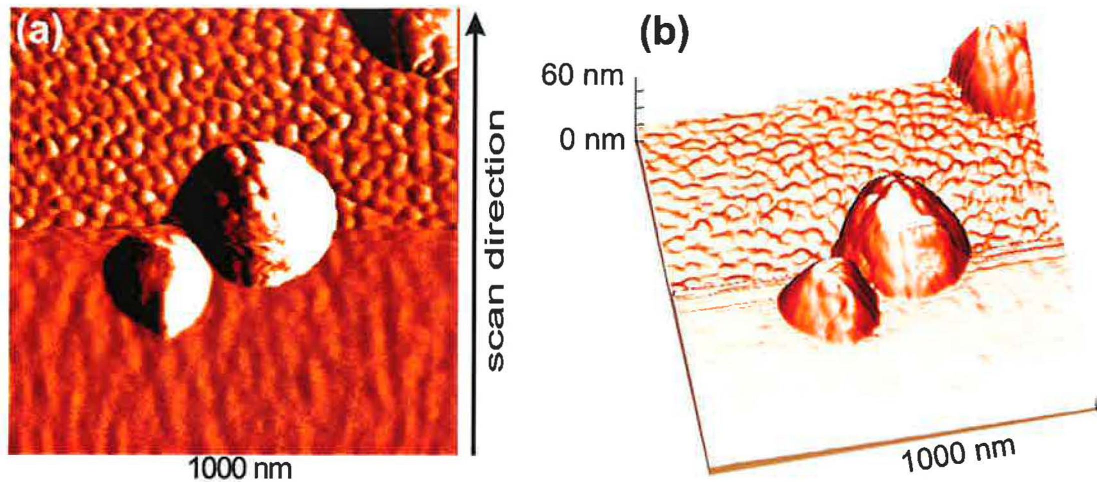

Figure 2.10: *Removal of adsorbates on the tip by scanning over a bigger protrusion (μc–Si:H grains) shown in (a) topography and (b) 3D view.*

Local current images can reveal also some types of artefacts. Most frequently we faced these two problems: Firstly, the wear off of the metal coating deposited on the standard body of Si cantilever, which makes the reproducibility of subsequent measurements difficult. The second one is the reliability of the current measurements on very rough surfaces, where the tip–surface contact area is changing and the local current map may provide apparent contrasts, which are nothing but a product of topography induced artefacts [155, 156].

2.4.6 Cantilever force interactions

Different types of cantilevers enable the measurement of various force interactions [157]. In the case of conductive cantilever and applied voltage the total force includes repulsive or attractive (van de Waals) force and Coulomb force. If the cantilever is less sharp, than a larger area must be taken into account in the consideration of a micro-capacitor defined by the tip and sample. If the capacitance of this system is higher, more charge can be concentrated and a stronger electrostatic force is detected as shown in Fig. 2.11 for the broken cantilever.

According to our experience, the measurement of the force curve under different bias voltages can provide a good check of conductive behaviour of the cantilever–

sample system. This is typically the first pre–measurement verification whether the cantilever is conductive (properly electrically attached, has enough of the conductive coating, etc.) and that the sample is ready for conductivity measurement (proper electrical connection, not too much oxidized surface, etc.).

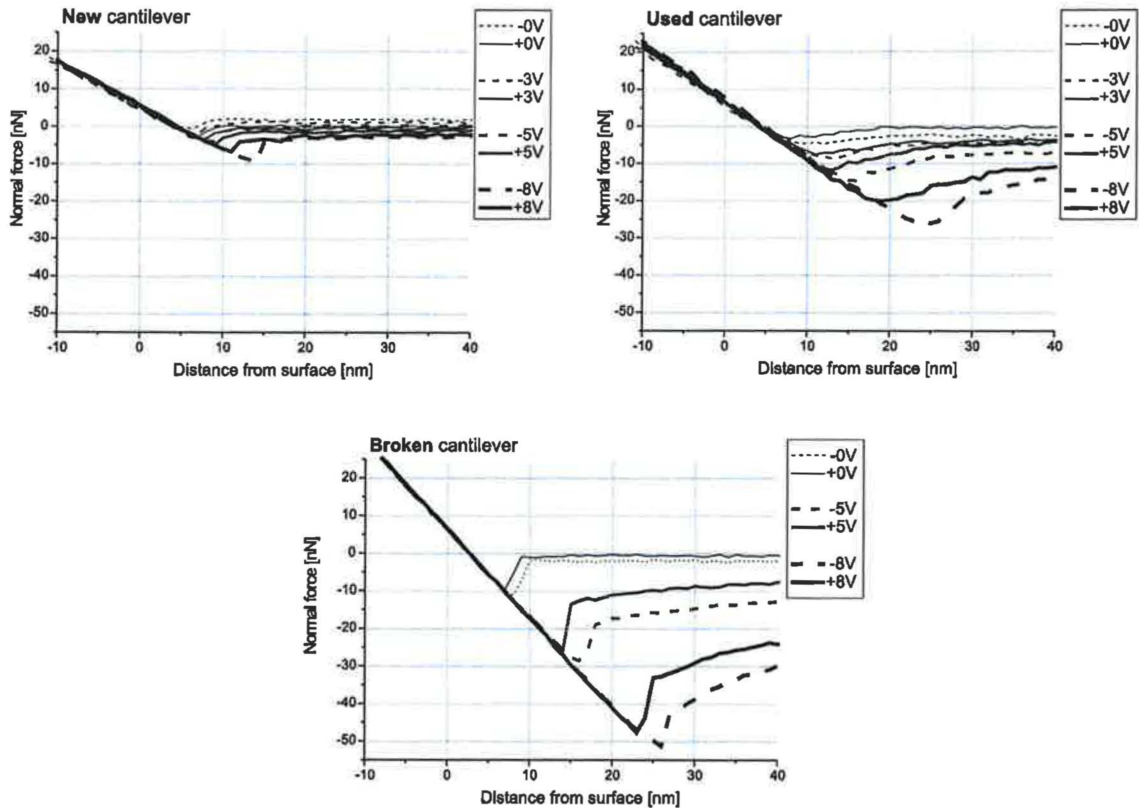

Figure 2.11: *Force interaction curves of* new, used *and* broken *cantilever on the surface of the 35° C sample of the VHF temperature series (Fig. 4.28). The cantilever (75 kHz, see Table 2.2) was made of highly doped silicon with no conductive coating.*

Chapter 3

STUDY OF MICROCRYSTALLINE SILICON

3.1 Motivation

In this chapter we will present the selected results obtained on our samples. We will put them into the context of previously published results (TEM cross–sectional images). These selected results will present interesting features of structure of μc–Si:H and will serve as supporting facts for the introduction of our model of growth (Section 3.2.3). We will also introduce a simple guiding rule (Section 3.3.5) to monitor the quality of μc–Si:H films based on our observations of their local structure and transport properties.

While the so-called "device–grade" a–Si:H is a well defined material [56], μc–Si:H represents quite a wide class of materials. This is due to the complicated heterogeneous microstructure of μc–Si:H, which consists of a mixture of crystalline grains, grain boundaries and a–Si:H "tissue" (Fig. 3.1).

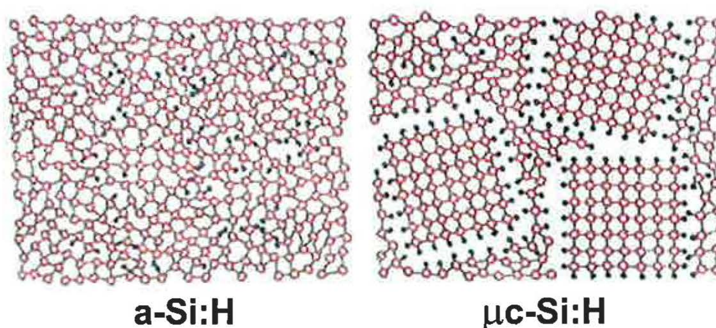

Figure 3.1: *The structural model of amorphous and microcrystalline Si after [12].*

However, μc–Si:H is still quite closely connected to a–Si:H. It can be prepared in the same deposition system by a small change of one deposition parameter – typically of hydrogen dilution r_H [52]. The TEM cross–sectional pictures of microcrystalline grains [158, 159] (Fig. 3.2) indicate that μc–Si:H may contain smaller or bigger grains mixed with various amounts of a–Si:H depending on film thickness and deposition conditions. The growth of μc–Si:H is, moreover, strongly influenced by the substrate [160]. It usually starts as the a–Si:H incubation layer (Fig. 3.3) with the thickness of few nm to 0.5 μm [82, 160].

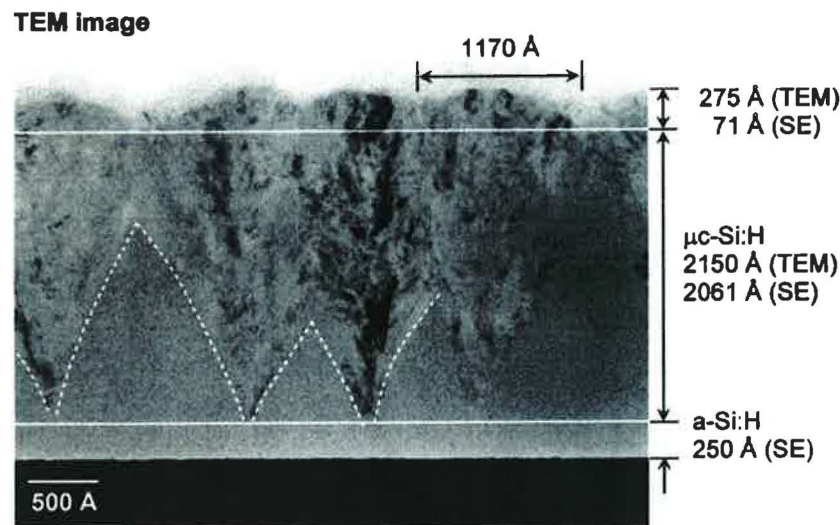

Figure 3.2: *Cross-sectional TEM image showing the evolution of microcrystalline grains in the real sample. This TEM micrograph was published by Dr. H. Fujiwara in [158] and here we show it with his kind permission.*

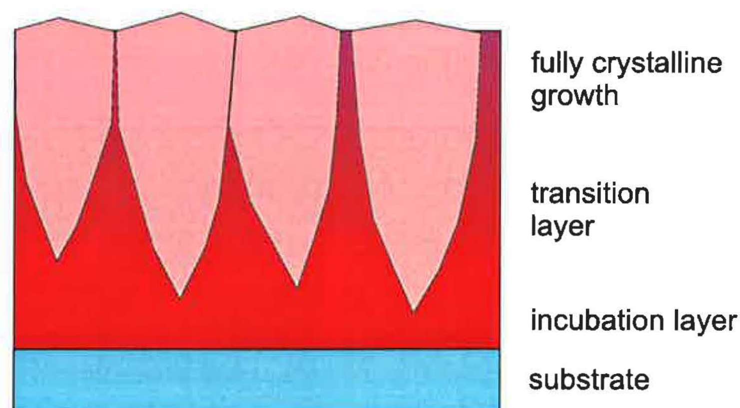

Figure 3.3: *Cross-sectional scheme summarizing the TEM observations (for example in Fig. 3.2) with the description of the growth stages.*

3.2 Structure of microcrystalline silicon

3.2.1 Cross-sectional measurements

Microcrystalline silicon thin films are known to have complicated inner structure. Even a simple observation of the surface of the a–Si:H and μc–Si:H samples by a naked eye or by the optical microscope (see Fig. 3.4) reveals significant differences in the light reflection, indicating glossy surface for a–Si:H and rough for μc–Si:H.

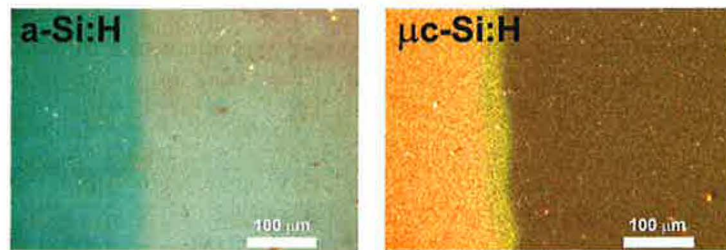

Figure 3.4: *Surface images by the optical microscope showing different reflectance of glossy a–Si:H and matt μc–Si:H samples. Each picture shows Si film deposited on Cr electrode (left part) and directly on glass (right part).*

In previous works, we performed studies of μc–Si:H using combined AFM microscope to visualize the surface of μc–Si:H films with high lateral resolution [154, 155, 156]. We attempted to measure the coexistence of microcrystalline and amorphous phases and after several experiments, we successfully detected the microcrystalline grains embedded in amorphous matrix. The utilization of local current enabled us to observe high contrast (about two orders of magnitude) between the crystallites and amorphous tissue with a resolution of 10 nm. However, the origin of this contrast needed an explanation based on the knowledge "what is below" the surface measured by AFM. Two approaches are possible for the study of structure below the surface:

- Probe the properties of one sample at different depths.
- Prepare a series of samples with the same deposition conditions, but with different thickness.

We used the first approach [161] to test the sample from the previous work by combined AFM [154]. This sample has similar deposition conditions to the sample Stm 147 (Table 3.5), i.e., there is ~100 nm thick a–Si:H sublayer in order to delay the nucleation within the 500 nm thick μc–Si:H top layer. Because the nucleation density on a–Si:H is very low, the growth results in a very thick transition layer and the

"surface crystallinity" as observed by AFM was about 40%. We have used Calotest (Section 2.3.8) to abrade a spherical crater into the sample as shown in Fig. 3.5(a). We also used a surface profiler across the crater to verify the dimensions observed by the optical microscope. Then we used the largest field of view of the ambient AFM microscope in the non–contact mode to obtain the detail of the surface shown in Fig. 3.5(b). It is interesting to see that the AFM topography image also reveals a contrast between the thin amorphous silicon sublayer and the μc–Si:H layer on top of it. This is probably due to different friction coefficients of these two silicon phases. Moreover, as seen in the AFM line profiles, there seems to be a change of slope on the boundary between NiCr and silicon layers, probably due to different abrasion speeds of the two materials.

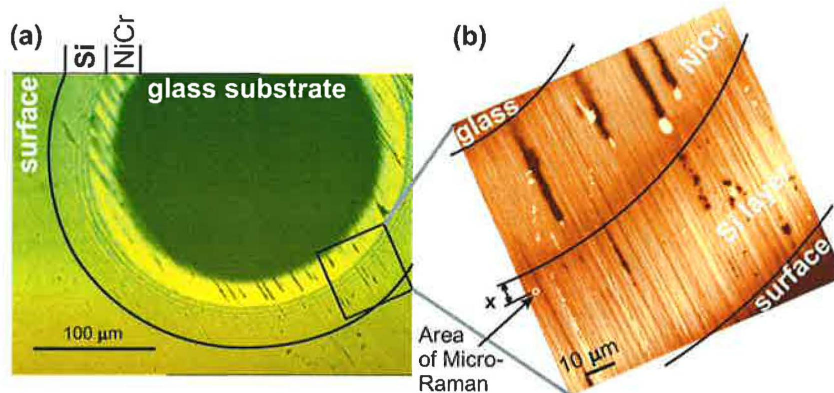

Figure 3.5: *Topography picture taken by (a) optical microscope and (b) AFM with very large field of view. The "Area of Micro–Raman" label indicates the spot size used in the measurements in Fig. 3.6.*

Such an abraded structure provides a unique insight in the structure of the deposited film – for some measurements it is in fact a "thickness series" in just one sample. To detect the properties in different thicknesses we have used micro-Raman spectroscopy (Section 2.4.1) to study crystallinity at different positions on the crater wall. An example of the spot size is indicated in the AFM image in Fig. 3.5(b). The observed Raman spectra are shown in Fig. 3.6(a) together with the distance **x** from the NiCr/Si boundary. Local crystallinity X_C values are plotted as a function of distance **x** in Fig. 3.6(b). The crystallinity exhibits a monotonous increase within the film and a plateau on the surface of the film. There is just one exception – the second curve from the top (dashed in Fig. 3.6(a)) shows much lower crystalline Si component than expected. This is due to a scratch, where the beam recorded spectra from deeper (and thus more amorphous) part of the sample.

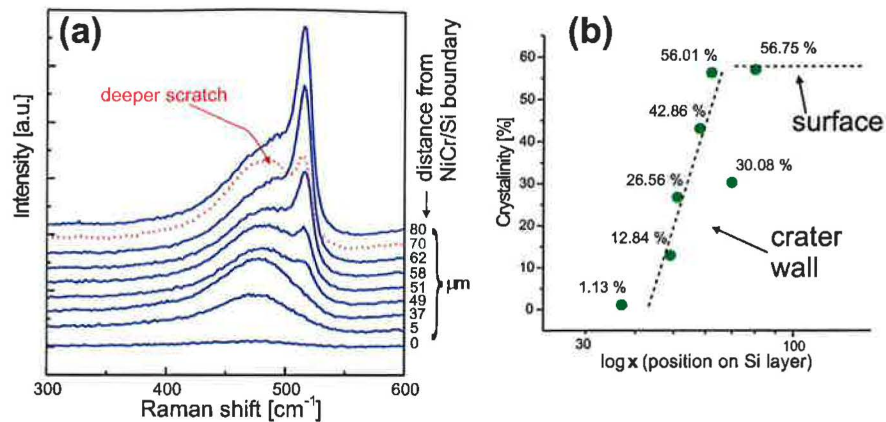

Figure 3.6: *Micro-Raman spectra (a) recorded at various positions in the abraded crater. Spectra are vertically shifted for clarity. Local crystallinity (b) derived from the spectra in (a) as a function of the position* x *on the Si layer (Fig. 3.5).*

The experiment with the spherical crater depth profiling brought a clear proof of thickness inhomogeneity, indicating an increasing portion of microcrystalline phase with increasing film thickness. This finding agrees well with the TEM cross-sectional picture (Fig. 3.2). Even though we obtained a thickness series within one sample, the dimensions of the crater are too small to allow our standard photoelectrical experiments. For this purpose a thickness series of samples prepared under same deposition conditions seems to be more suitable.

3.2.2 Surface structure in AFM

As the next step we decided to study a–Si:H and μc–Si:H thin films by AFM (Section 2.4.2). Before doing so, we employed Scanning electron microscopy (SEM) with high resolution in a comparative measurement examining AFM for a possible occurrence of artefacts. This test was done with the special sample Stm 108 (Section 3.2.7). The SEM measurements were performed at the Institute of Scientific Instruments, AS CR, Brno. AFM topography was then measured in our group by ambient AFM Veeco Dimension 3100 in tapping mode using standard non–coated Si cantilever. The images obtained in the tapping mode fully correspond to the contact mode measurements provided that a similar cantilever was used.

Fig. 3.7 shows a perfect agreement of the grain shapes, typical diameters and also details of the inner structure of grains. The distribution of grains on the surface is slightly different due to different position on the sample. Both images (SEM and

AFM) were processed by the edge enhancement procedure for easier comparison. The original SEM image was published in [162].

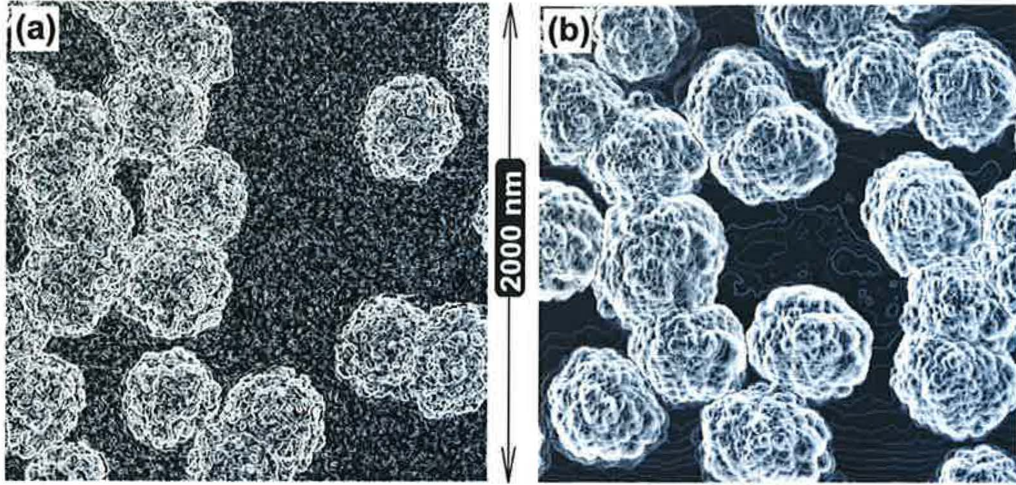

Figure 3.7: *Comparison of two different microscope techniques: (a) High resolution SEM and (b) AFM of a mixed-phase sample Stm 108.*

We continued this study with several thickness series. We started with the series prepared at the conditions optimized for the amorphous silicon films, which particularly means T_S=250° C. The microcrystalline growth was obtained by the dilution closer to the μc–Si:H boundary, i.e., lower concentration c_{SiH_4} (Tables 4.2 & 4.2).

The key observation for the introduction of the model of growth appeared after we evaluated the samples of the thickness series prepared at slightly different deposition conditions – the main difference was in quite low T_S=75° C. This low substrate temperature has turned out to be very suitable for obtaining quite large grains (Fig. 3.8) at given deposition conditions (Table 4.6).

At the lowest thickness (100 nm sample in Fig. 3.8) the microcrystalline grains are seen as isolated roughly circular objects. At the medium thickness (450 nm) many grains have already collided and form an irregularly connected network of grains. At the highest thickness the surface of the sample is fully covered by the microcrystalline grains. While the boundaries of isolated grains are circular, after the grain collision they are approximately straight (see the bold lines in the Fig. 3.8). The radii of the grains are to some extent proportional to the film thickness. Finally, the straight grain boundaries are approximately perpendicular to the lines connecting the grain nuclei, bisecting the distance between these nuclei. This opens a question if the grains could be approximated by some simple shape, for example by the cones and if their tops have some simple shape too.

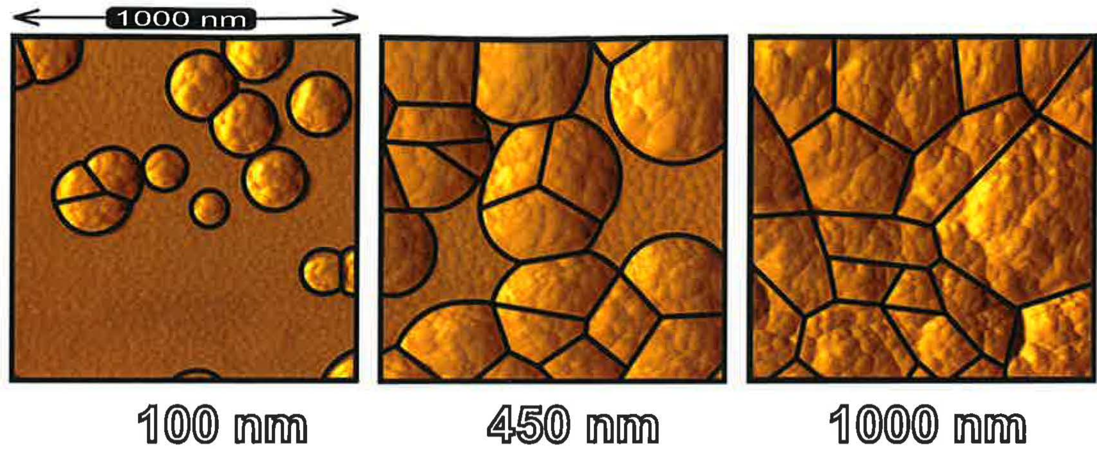

Figure 3.8: *Key observation of the straight grain boundaries (highlighted by solid lines) on the samples of the thickness series prepared at 75° C. Numbers under the pictures indicate the film thickness. Original topography data in Fig.4.13.*

To answer this, we took several AFM line profiles over the microcrystalline grains and attempted to fit them. The profiles shown in Fig. 3.9 come from the measurement of a special sample Stm 108 (Section 3.2.7), where we succeeded to obtain very nicely isolated grains. No matter the differences between the special sample Stm 108 and other samples, the AFM line profiles over the grains reveal the same shapes including the samples at T_S=75° C, for which we have also performed fits with similar results. The line profiles of Stm 108 are intentionally selected since the largest size of grains provides best precision of fits. It is more than clear that the shapes of the fits in Fig. 3.9 are circular arcs. Only the profile of the largest grains slightly deviates from

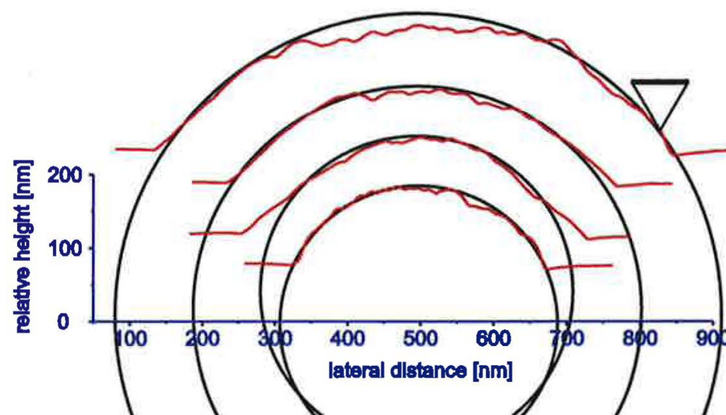

Figure 3.9: *Fits of the AFM line profiles over the grains of the sample Stm 108 show circular shapes of the grain tops. The small triangle in the right part of the image represents the approximate shape of the tip of the AFM cantilever.*

the spherical shape, i.e., in the middle of the largest grain in the Fig. 3.9 the signs of flattened top can be seen. The flattening would correspond to the grain size exceeding the precursor diffusion length, when the grain surface interior is no longer influenced by surrounding amorphous surface [17].

Inspired by the AFM surface observations in Figs. 3.8 and evaluation of the line profiles in Fig. 3.9 we have introduced a simple growth model describing the behaviour of microcrystalline grains during the growth of the μc–Si:H [163]. The first results comparing the artificial surfaces (from the growth model) and the real surfaces measured by AFM appeared in [164]. In this model, each grain is represented by a spherically capped cone with a fixed apex angle (Fig. 3.10). Similar conical structures of microcrystalline grains have been proposed earlier for example in [82, 165, 166]. It should be noted that we use the term "grain" to denote the microcrystalline regions which are in fact aggregates composed of nanometer sized crystallites. We will address this terminology in detail and clarify the question of grains in μc–Si:H in Section 3.3.4.

3.2.3 Simple model of growth

The geometrical model for the growth of μc–Si:H grains is shown in Fig. 3.10. The boundaries divide the sample area into the natural neighbourhoods available for the growth of each grain [163]. At a certain thickness, the whole surface plane is covered by the crystalline grains tiling the sample in so called Voronoi tessellation. The growth of the grains in the network of the Voronoi neighbourhoods is the simplest possible description of the growth starting from the randomly distributed nuclei [167]. The Voronoi tessellation is a mathematical answer to the question of "What are the natural neighbours in a random network?" and thus provides a universal description for many phenomena in fields as diverse as the growth of polycrystalline materials, geological formations, biological structures, cosmology and even marketing studies. It is the simplest of so called adjacency network structures and it seems to be well suited to describe the μc–Si:H growth features. We have used the Voronoi network geometry to simulate an evolution of the μc–Si:H properties during its growth. The model has only two fitting parameters:

- the nucleation density (grains per μm^2)
- the apex angle γ of the cone (Fig. 3.10).

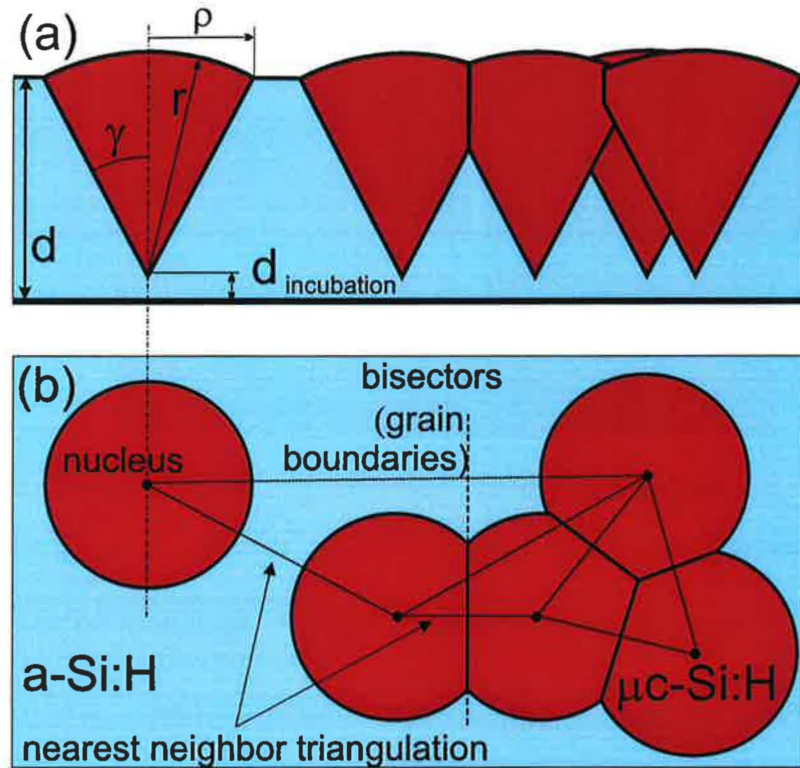

Figure 3.10: *Model conditions: (a) cross-sectional scheme and (b)top view of several conical grains showing the definition of apex angle and formation of straight grain boundaries as a consequence of the nearest neighbour (Delaunay) triangulation.*

3.2.4 Results of the model of growth

We have used the growth model to predict the surface topography and trends of conductivity and roughness of μc–Si:H films [163]. In Figs. 3.11 and 3.12 we present the simulated surface topographies and roughness values, respectively [164].

We attempted to describe the features of one of the thickness series, the characteristics of which are presented in the Section 4.5. The corresponding topographies of the real samples is shown in the Fig. 4.13 and the roughness values in the Fig. 4.16. As the fitting parameters, the following values were selected:

- nucleation density 40 grains per μm^2
- apex angle $\gamma = 20°$
- nucleation at the substrate surface ($d_{incubation}$=0 nm).

The model of growth described above is the simplest possible description and upon a close inspection of the topography images we can identify growth features in which the growth of real samples differs from the model simulation. For example, the model

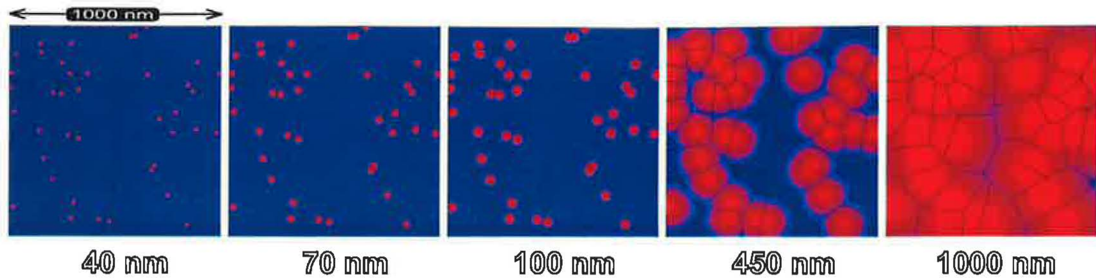

Figure 3.11: *Model surfaces computed by the growth model to fit the RMS roughness of the real samples of the thickness series at 75° C (Fig. 4.13).*

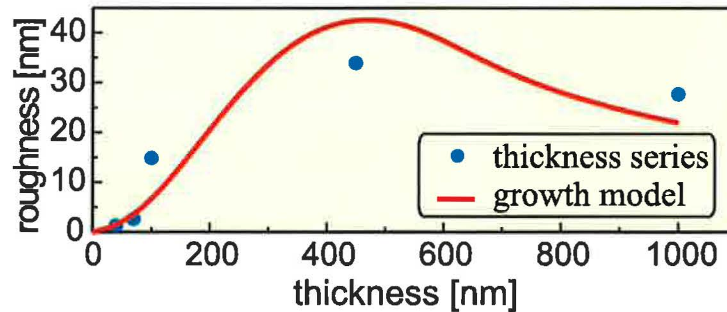

Figure 3.12: *Surface roughness measured by AFM for the samples of the thickness series at 75° C (circles, Fig. 4.13) together with the result of simulation by our model of growth (solid line, Fig. 3.11).*

does not take into account the fact that some grains nucleate later during the growth of the film and they are observed in AFM as circular grains with smaller diameters. In the growth model we assume the simplified condition, when the *nucleation* process takes place *at one level* only (Fig. 3.13(a)). The grain apex angle γ also seems to change within the film thickness (Section 3.2.5). Furthermore, we have neglected the existence of the incubation layer, since there were no experimental data available. The AFM observation of the real samples (Fig. 4.13) indicates that at the thickness of 40 nm there are already the first grains visible and the incubation layer thickness $d_{incubation}$ is relatively low compared to the thickness of the samples.

In spite of its simplicity the model leads to the simulated surface structures remarkably similar to the actually observed surfaces and to successful predictions of the evolution of sample crystallinity, conductivity, percolation threshold and surface roughness – the results shown in Fig. 3.12 are in agreement with a common trend of roughness evolution described in the Section 3.2.6. Let us now examine the assumptions on which the model of growth was based.

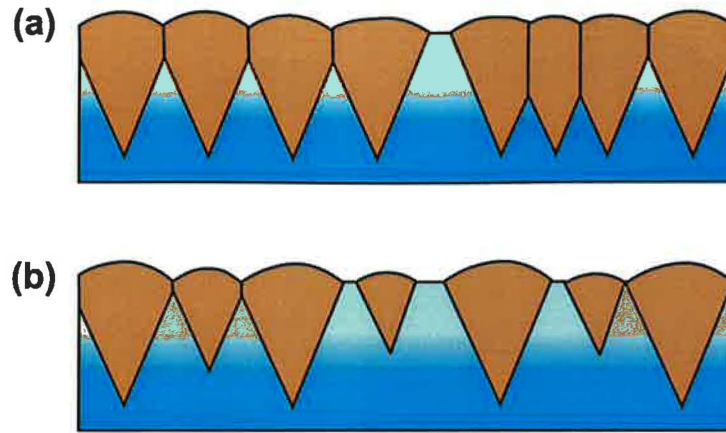

Figure 3.13: *Cross-sectional scheme of the mixed–phase Si film, where the grains nucleated (a) at* ***one level*** *only and (b) at* ***more levels****.*

3.2.5 Anatomy of the grain

We first used the AFM images of the samples of thickness series at 75°C (Fig. 4.13 and also the right column in Fig. 3.14) to make a reconstruction of the cross-sectional shape of the grain [17, 162]. From each AFM image at the certain film thickness we took the diameter of the largest grain assuming that this could be the maximum size to which the grain would grow without the influence of other grains. This maximum grain dimensions were put into the same scale and placed at the corresponding thickness level of the scheme. The result of such a reconstruction is shown in the Fig. 3.14. The same reconstruction was also done for the thickness series prepared at 250°C with a similar result. The cross–sectional scheme clearly shows that the **grains evolve in two distinct stages**: an expansion stage followed by an elongation stage.

At the largest thickness the grains already collided and filled the whole surface and the grain radii were extrapolated using the Voronoi construction. Yet even at this thickness, the remaining surface of the grain is spherical.

In spite of a more complicated development of the grain shape, the model of the Voronoi network for the grain neighbourhoods remains valid. The only difference from the simple geometry shown in Fig. 3.10 is the rate with which the grains fill the neighbourhoods available for their growth.

All the grains observed on the surface of samples with a given thickness have nearly identical diameters (Figs. 3.14 & 4.13) and so we can conclude that they nucleated simultaneously near the substrate surface. However, the center of the spherical cap does not coincide with the grain nuclei positions as the model shows in the Fig. 3.10. This disagreement is clearly seen in the Fig. 3.15, where the complete circles fitting

Figure 3.14: *Reconstruction of the cross-sectional shape of the microcrystalline grain based on the AFM surface pictures. The X:Y axis ratio is real, i.e., 1:1.*

the AFM line profiles are shown. This behaviour was observed for more series of samples and results in more pronounced shape of the grain top sphere due to its smaller diameter.

Other consequence of this more complicated shape of the grains is the evolution of the apparent apex angle with film thickness. The apparent apex angle was evaluated from the AFM surface pictures as a corresponding angle γ provided that the grains would grow according to the model conditions (Fig. 3.10) with zero $d_{incubation}$. The values of the apex angle for 5 different thicknesses corresponding to the samples and levels depicted in the Fig. 3.14 are given in the Table 3.1. The plot of the apparent apex angle γ for many grains of different series of samples is in the Fig. 3.16. The solid line in this graph highlights the maximum apex angle values for each thickness, which would again correspond to the ideal growth conditions for a single grain. The apex angle first increases with the growing sample thickness (fast growth of the grain caused probably by relatively high supply of precursors), passes through a maximum and then slowly decreases (competition and influence of other grains, limited supply of precursors).

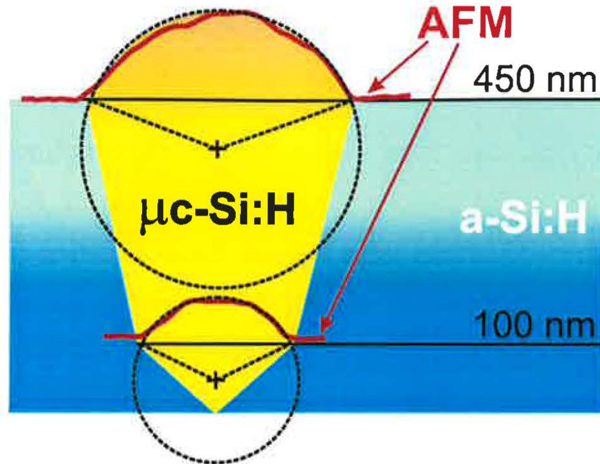

Figure 3.15: *Real AFM line profiles (thick line) of the local height together with the cross–sectional schetch of a single microcrystalline grain. The X:Y axis ratio is 1:1.*

Table 3.1: *Apparent apex angles corresponding to the grain surface dimensions at different thicknesses as shown in Fig. 3.14.*

Thickness	40, 70	100	450	1000
Apex angle γ	36.5	48.7	23.9	15.4

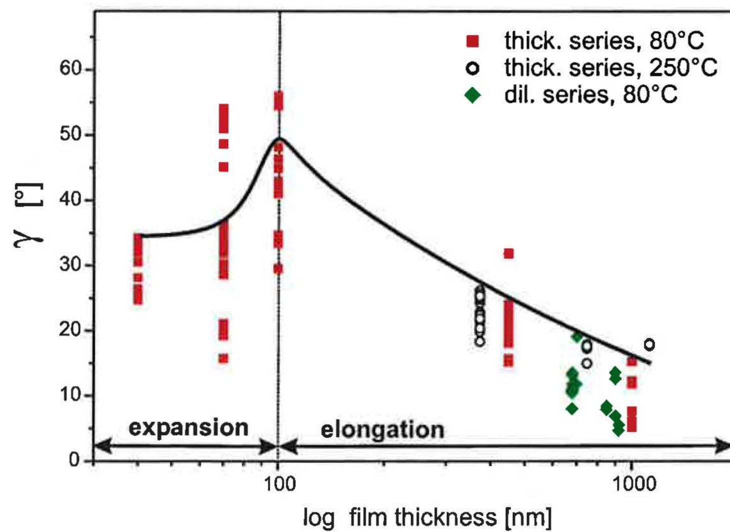

Figure 3.16: *Apparent apex angle evolution with the film thickness corresponding to two stages of growth – expansion and elongation – indicated in the Fig. 3.14.*

3.2.6 Surface roughness evolution

The most used numerical value derived from the topography image is the surface roughness σ_{RMS} (Section 2.4.3). As the roughness is very illustrative and sensitive way to detect the transition from a–Si:H to μc–Si:H structure, it is useful to mention the basic stages of growth of microcrystalline silicon thin films. Fig. 3.17 shows the cross–sectional sketches of the mixed–phase films at different thicknesses. The bold solid lines above the surface are real AFM line profiles taken from the AFM images of the samples in Section 4.5 (Fig. 4.13). The evolution of the structure is reflected in the values of roughness (Fig. 3.12) and it undergoes the following stages:

- First, the surface contains mainly the amorphous phase resulting in a small roughness (70 nm).
- Then, the *surface roughening* appears for the mixed–phase, in which microcrystalline grains are surrounded by amorphous tissue (450 nm).
- Finally, the *surface smoothing* appears as the microcrystalline grains cover the entire surface (1000 nm).

In Fig. 3.12 there is a clear maximum of RMS roughness at the thickness of 450 nm. The existence of peak in roughness is a common feature of the mixed phase material reported by many researchers, e.g. by Collins at al. [168]. The sensitivity of roughness to indicate the a–Si:H/μc–Si:H transition will be exploited mainly in the Chapter 4 in the complex characterization of series of samples prepared at different deposition conditions.

Since the σ_{RMS} is a statistical measure, its value and precision is dependent on a proper selection of the scan area.

As we are studying the material with amorphous phase having small roughness and also the microcrystalline grains with sizes up to hundreds of nanometers, the selection of a representative field of view is not so easy. The increase of the scan size usually increases the roughness [150], but after reaching some critical field of view, the roughness saturates. For example, the roughness of a–Si:H saturates already at the scale of 100×100 nm [149].

For the comparison purposes we have chosen one fixed field of view (1000×1000 nm) and we present all the AFM images with this scan size. This value is a good compromise between the precision of the roughness value and the fine details of the surface. For the a–Si:H or fully μc–Si:H surfaces, the relative error of σ_{RMS} is far below 10%, only in the case of mixed–phase samples it can reach ~30 %.

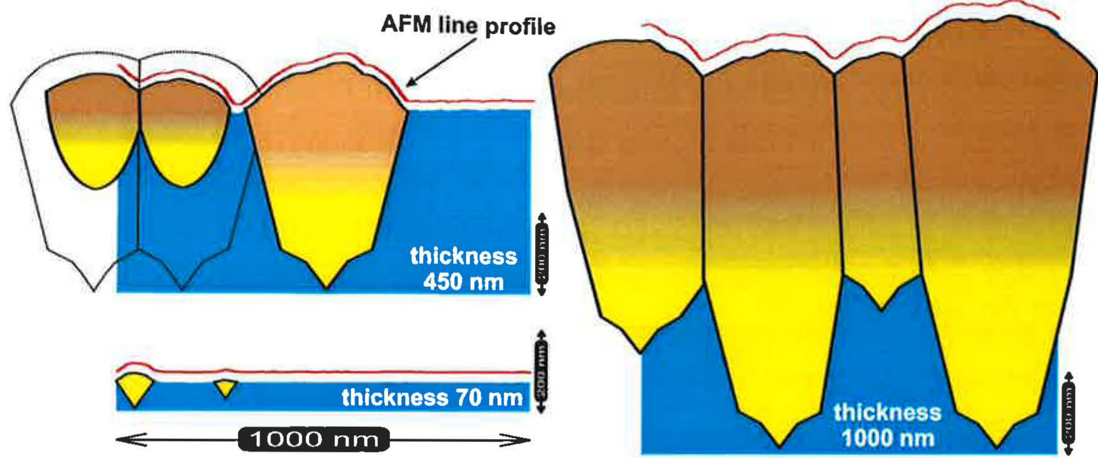

Figure 3.17: *Real AFM line profiles in the demonstration of the surface roughness evolution of μc–Si:H as a function of film thickness. The X:Y axis ratio is 1:1.*

3.2.7 Growth process

Conical grains with spherical caps would grow in the mixed–phase Si film as a result of different growth rates v_a and v_c of the amorphous and microcrystalline phases, respectively. The cone angle γ (measured from the cone axis, see Fig. 3.10) is given by the formula $cos\ \gamma = v_a/v_c$, i.e., the higher the growth rate of the microcrystalline phase v_c, the bigger the apex angle γ. In the limit case of $v_a \sim v_c$, the apex angle γ would approach zero (the grains would look like needles).

The key observation came from the study of the surface by AFM. We have noticed that at the edge of large microcrystalline grains the surface of surrounding amorphous phase often exhibits a small depression. This observation was very clear in the case of the specific sample Stm 108, where the amorphous phase was very smooth. Deposition conditions of the sample Stm 108 are given in the Tables 3.2 and 3.3.

Table 3.2: *Deposition parameters of the specific sample Stm 108. The value of* d *represents the total sample thickness including 100 nm a–Si:H sublayer.*

Sample	d [nm]	dil. r_H	T_S [°C]	f_{exc} [MHz]	P_{eff} [W]	p_{tot} [Pa]	$[H_2]$ [sccm]	$[SiH_4]$ [sccm]
Stm 108	750	32	250	13.56	19.0	70	50.0	1.6

The example of such an observation is shown in the Fig. 3.18, where two different places of the specific sample sample Stm 108 are shown in local height and topography signals. In the local height image the plane of the zero height was shifted to match the level of the surrounding amorphous phase. Then the darker surrounding area around the white cross-section of the grain shows nicely the symmetrical depression and its

Table 3.3: *Additional deposition parameters of the specific sample Stm 108.*

Average deposition rate r_d	~0.19 nm/s
Plasma power density	~0.30 W/cm^2
Substrate potential	**grounded**

Table 3.4: *Summarizing table of the surface properties measured in different places on the sample Stm 108.*

Sample	RMS [nm]	AGS [nm]
Stm 108 [Fig.3.18(a)]	18.4	400
Stm 108 [Fig.3.18(b)]	26.6	510
Stm 108 [Fig.3.7(b)]	38.1	500

lateral features. The grains appear white because their heights exceed the color data range of the image. For the comparison purposes, the standard topography images of the same area were added as insets in the middle of the Fig. 3.18.

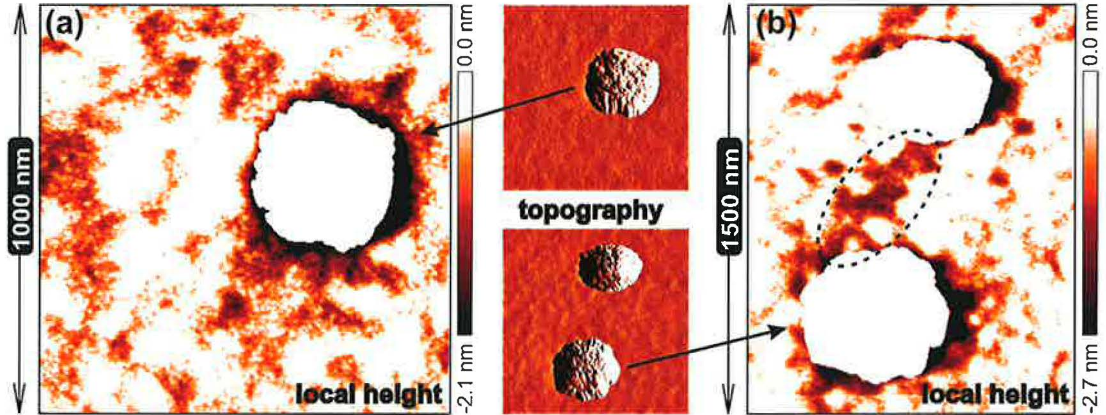

Figure 3.18: *Topography and local height images of the sample Stm 108: (a) shows the neighbourhood of one grain and (b) shows another place with two grains of similar size. The smaller inset images show the standard topography of the same area.*

The sample Stm 108 was the only sample that we present in this work, which exhibited surprisingly flat amorphous phase. The only different deposition condition (compared to other samples prepared in the same chamber) was the grounded substrate holder (Table 3.3 vs. 4.1). The very flat a–Si:H neighbourhood helped with the fits of the grain profiles (Fig. 3.9) and made it possible to provide the first empirical estimation of the diffusion length L_{prec} of precursors on the Si surface.

The amorphous surface depression may be understood as a capture of the diffusing growth precursors [68] from the vicinity of the grain by the microcrystalline surface growing faster. In such a case the logarithmic plot of depression vs. distance from the grain edge would give straight lines with slopes indicating the diffusion length of precursors L_{prec} on the growing surface. We analysed the line profiles in all directions from the grain edge to avoid any artefacts possibly introduced either by the AFM cantilever or sample non–homogeneity. From these plots we made the following **estimation of L_{prec}=(60±30) nm** [17, 162]. In the case of very large grains the signs of flattened tops can be observed (for example the top profile in the Fig. 3.9). The flattening would correspond to the situation, where the grain size is surpassing the precursor diffusion length L_{prec} and the grain surface interior is then no longer influenced by surrounding amorphous surface. Another interesting visualization of the growing process consequences can be seen in the Fig. 3.18(b), where the dashed ellipse shows a shallow valley. We attribute its presence to the lack of growth precursors between two neighbouring grains.

3.2.8 Delayed nucleation

There are the two basic parameters determining the growth of microcrystalline grains: nucleation density and grain apex angle. Both were mentioned as the fitting parameters of our model of growth (Section 3.2.3). Although there is not much data that would give a clear meaning to the values of apex angle γ, we speculate that γ is mainly determined by the amount of silane radicals and corresponding surface reactivity, i.e., it is in close connection with c_{SiH_4} and to some extent also with excitation frequency f_{exc} and applied power P_{eff}.

On the other hand the nucleation density seems to be dependent mainly on the substrate material and its chemical and electrical properties. Comparison of Si films deposited on glass and metal coated glass is shown in Fig. 4.9 and Figs. 4.13 & 4.14.

In this section we demonstrate how we attempted to prepare large microcrystalline grains that were essential for the study of their growth in previous sections. Prior to the deposition of the main μc–Si:H layer, we introduced the a–Si:H sublayer, which suppresses the influence of substrate and also decreases the nucleation density [154, 169]. This naturally lead to the lateral growth of grains resulting in their bigger sizes. This trick with a–Si:H sublayer was used for the sample Stm 108 (Figs. 3.7 & 3.18) and three samples (Stm 144, 147 & 151) of a small thickness series presented in this section (Table 3.5). All these samples were prepared by conventional PECVD

at T_S=250° C at conditions similar to samples in Section 4.4.1. The different modes of growth were achieved just by the change of the dilution parameter from r_H=12 (a–Si:H sublayer) to 21 (μc–Si:H layer). Later, when we started to study the samples prepared at T_S ~80° C, we found that lower T_S also decreases the nucleation density and leads to the growth of large grains as well (Fig. 3.8). A brief overview of the structure of three samples with a–Si:H sublayer should demonstrate how the typical growth of μc–Si:H structure looks like, even if it was slowed down.

Table 3.5: *Overview of the properties of the samples with delayed nucleation. The values of* d *represent the total sample thickness including 100 nm a–Si:H sublayer. For deposition conditions see Table 4.2.*

Sample	d [nm]	RMS [nm]	AGS [nm]	L_{diff} [nm]	σ_d $[\Omega^{-1}cm^{-1}]$
Stm 151	270	8.3	154	125	1.85×10^{-10}
Stm 147	650	28.9	374	185	1.9×10^{-8}
Stm 144	1200	26.4	439	207	6.4×10^{-7}

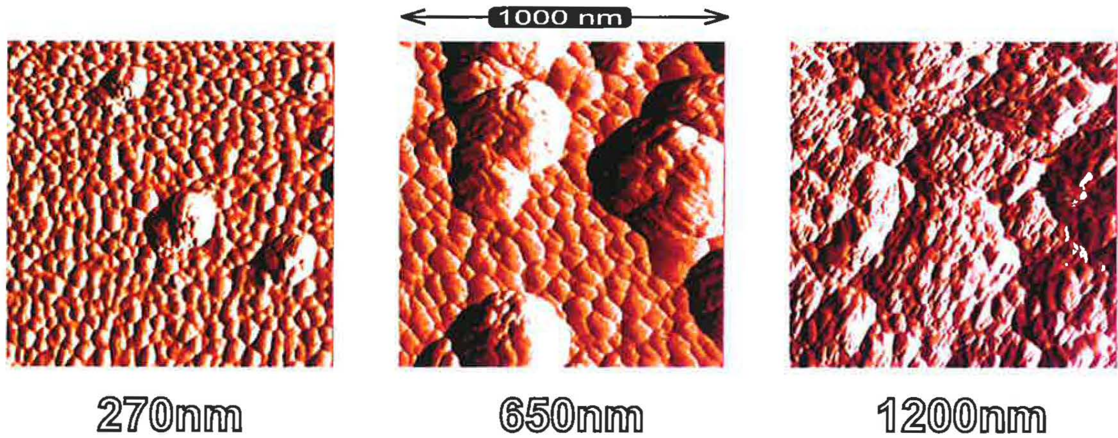

Figure 3.19: *AFM images of the samples with delayed nucleation. Numbers below the images indicate the total sample thickness including the a–Si:H sublayer.*

Two structural phases can be seen in the AFM topography images (Fig. 3.19). At small film thickness (270 nm) the amorphous phase is dominant. Only a few grains are located on the surface of this sample – seen as larger shadowed circular protrusions. By the usage of combined AFM producing topography image and map of local currents we have shown that these protrusions correspond to microcrystalline grains [154]. The local current map of the 270 nm sample (Stm 151) is shown on a larger scale in Fig. 3.22. With increasing thickness (650 nm, sample Stm 147) the grains increase

their size and finally the whole surface is covered with microcrystalline grains – here observed at 1200 nm (Stm 144).

The plots of the absorption coefficient α obtained from the CPM measurements are shown in the Fig. 3.20. Starting with the 270 nm sample, the CPM spectrum shows a typical response of a–Si:H – high absorption above 1.8 eV accompanied by a broader band gap. The second sample (650 nm) exhibits amorphous–like response below 1.8 eV, while above 1.8 eV the values of α are slightly decreased, following the typical μc–Si:H values. This sample combining both amorphous and microcrystalline features nicely demonstrates the mixed–phase, which is also seen in the AFM image (Fig. 3.19). The microcrystalline structure prevails in the case of 1200 nm sample with typical μc–Si:H CPM spectrum [122]: α above 1.8 eV is smaller compared to a–Si:H but still higher than for c–Si; below 1.8 eV, α follows the values typical for single crystal silicon with narrower band gap ~1.1 eV.

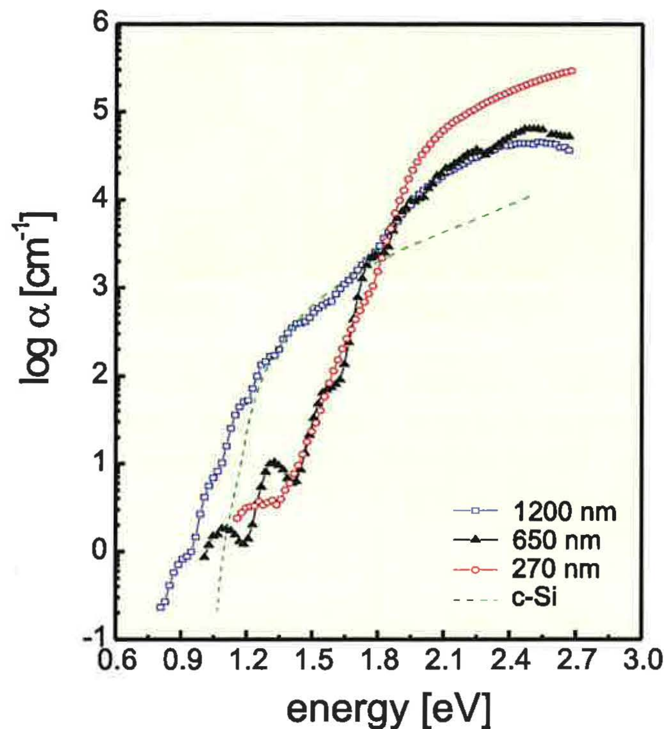

Figure 3.20: *CPM spectra of the sample of the thickness series with a–Si:H sublayer.*

Based on AFM and CPM data we conclude that **the a–Si:H/μc–Si:H transition appears in the range of ~500–800 nm** of film thickness. This represents a 400 nm shift to to higher film thickness compared to the samples without the a–Si:H sublayer. We will discuss the impacts of the presence of a–Si:H sublayer in Section 5.2 in the comparison with the data from other thickness series.

3.3 Properties of microcrystalline silicon

3.3.1 Local conductivity

Dark conductivity (σ_d) is easily obtained macroscopic characteristics. However, its values may be subject to many effects. In [108] we have shown that defective a–Si:H may reach even $\sigma_d \sim 10^{-2}$ $[\Omega^{-1}cm^{-1}]$, which is very misleading compared to typical $\sigma_d \sim 10^{-6}$ $[\Omega^{-1}cm^{-1}]$ of μc–Si:H films.

For a proper understanding of the electronic properties of the sample, additional data from other measurement methods are thus needed. This can be Raman crystallinity X_C, optical absorption coefficient α from CPM [170], diffusion length L_{diff} from SSPG etc.

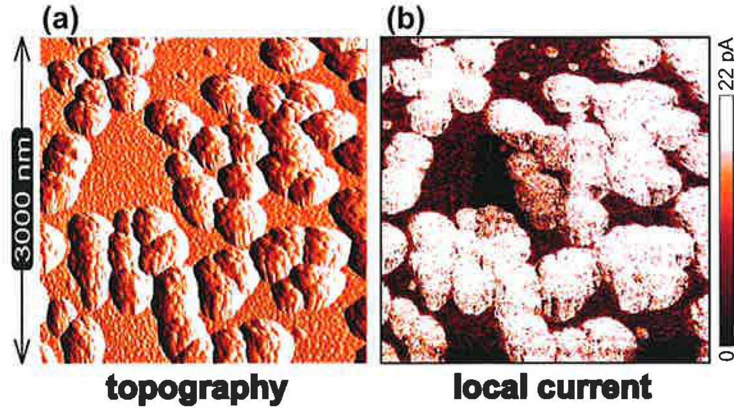

Figure 3.21: *Surface topography of the Ge08 sample with thickness 450 nm (Section 4.5) on a larger field of view. Topography (a) shows microcrystalline grains and amorphous tissue. The identification of grains (brighter areas) is possible in the local current map (b) measured at bias voltage of +8V.*

To understand the general electrical properties of μc–Si:H films, we came with the idea of local electrical probing with conductive AFM cantilever (Section 2.4.4). Such a combined AFM measurement simultaneously provides a map of topography and local current [154, 155, 156]. Combined AFM of mixed phase Si films reveals additional information and enables a proper identification of topographical features. This is possible due to a large difference in conductivity between a–Si:H and μc–Si:H, which creates the contrast in the map of local current (Fig. 3.21). However, the general relationship between the values of local current and σ_d of the whole film is not yet fully understood. The local current is influenced by many material and instrumental factors. The material-induced factors are the presence of native oxide on the surface, thickness of the thin Si film, arrangement of grains in the film, presence

of the incubation layer etc. The instrumental part is influenced by the bias voltage applied, speed of scanning, quality (conductivity) of the tip etc.

The first measurement of combined AFM of mixed phase film was performed in UHV environment [154] with the in-situ sample, bias voltage of 3V and local currents in the ~0.1 nA range. Fig. 3.21 shows the combined AFM measurement of ex-situ sample, where the voltage of 8V gave rise to the local currents in the ~10 pA range. Due to the development of sensitive current detection, it is possible to perform the combined AFM of thin Si films even in ambient conditions. The measurement performed in air reveal currents of ~10 pA at 2V bias voltage [171]. This is comparable with the typical values of STM measurements on Si films [172], which means that the combined AFM is measuring the tunneling current flowing through the native oxide on the surface of Si film.

Comparison of typical local current values of a-Si:H and μc-Si:H (Table 3.6) reveals only 3-5 times higher values for μc-Si:H. This is in disagreement with the macroscopic σ_d providing difference of 4 orders of magnitude. The explanation is based on the geometrical setups of the measurements: The macroscopic σ_d is measured parallel to the substrate plane and the a-Si:H incubation layer does not affect σ_d, which reflects the conductivity of the interconnected network of grains on the surface. The local current measurement is performed in perpendicular direction. The local current is limited by the presence of a-Si:H incubation layer, which prevents the microcrystalline grains from the direct contact with the bottom electrode.

Table 3.6: *Experimental local current values for a-Si:H and μc-Si:H structures on different samples evaluated from combined AFM measurements at various conditions.*

Conditions	a-Si:H	μc-Si:H
UHV, in situ sample, 3V	3 pA	20 pA
UHV, ex situ sample, 8V	5 pA	20 pA
air, 2V	0.01 pA	0.04 pA
air, 3V	0.1 pA	0.4 pA

3.3.2 Memory effect

During the combined AFM measurements on different fields of view we have observed an interesting behaviour of thin silicon films. After scanning the surface with the applied bias voltage a local change of electronic properties was induced. This change is then detected as a decrease in the local current values (Fig. 3.22) and also

as a difference in surface potential [173]. For the detection of memory effect we also employed a unique AFM technique [173] detecting three different surface features in one measurement - topography and local current in contact mode and surface potential in spectroscopic regime.

Upon a closer look on Fig. 3.21(b) a less brighter area of about 1000×1000 nm could be found in the middle of the local current map of local current. This is the manifestation of an unintended memory effect. The previously scanned smaller field of view is a typical measuring procedure. We aimed to obtain a standard scan size of 1000×1000 nm for the comparison purposes. However, it has turned out that this particular sample includes much larger grains worth measuring on a larger scan size. This lead to the result shown in the Fig. 3.21.

However, the physical mechanism of memory effect occurring both on surface of a–Si:H and μc–Si:H remains an open question. There are two possible explanations: Local anodic oxidation (supported by the decrease of current in the spot of previous measurement) and charge trapping (supported by a not detectable change of topography). Recent experiments indicate that the memory effect occurs also in the ambient AFM in air [174] and the results of surface potential measurements (Kelvin probe microscopy) support the charge trapping mechanism. The effect is stable for hours and can be "erased" by illumination [174]. The memory effect has been found proportional [175] to *voltage* applied between sample and cantilever and to *time* for which the surface was in contact with the cantilever, i.e., the decrease of local current is more pronounced when the area is scanned repeatedly (Fig. 3.22). Due to the recent findings about the reversibility of this process we expect this effect to become an interesting candidate for the information storage applications.

3.3.3 Transport

Microcrystalline Si is supposed to have a semi–ordered structure, i.e., the medium range order (Fig. 3.1(b)), while the amorphous silicon exhibits none or very short range order as depicted in Fig. 3.1(a). According to this scheme it is clear that the μc–Si:H will never reach 100% crystallinity.

Theoretical description (percolation theory) of a heterogeneous system composed of conductive particles in a non–conductive matrix predicts a sharp rise in conductivity at about 33% volume concentration of the particles. Such threshold was observed for doped μc–Si:H samples [176, 177]. However, for all the samples prepared in this work, we found the percolation threshold around X_C=65%. Our modelling shows that

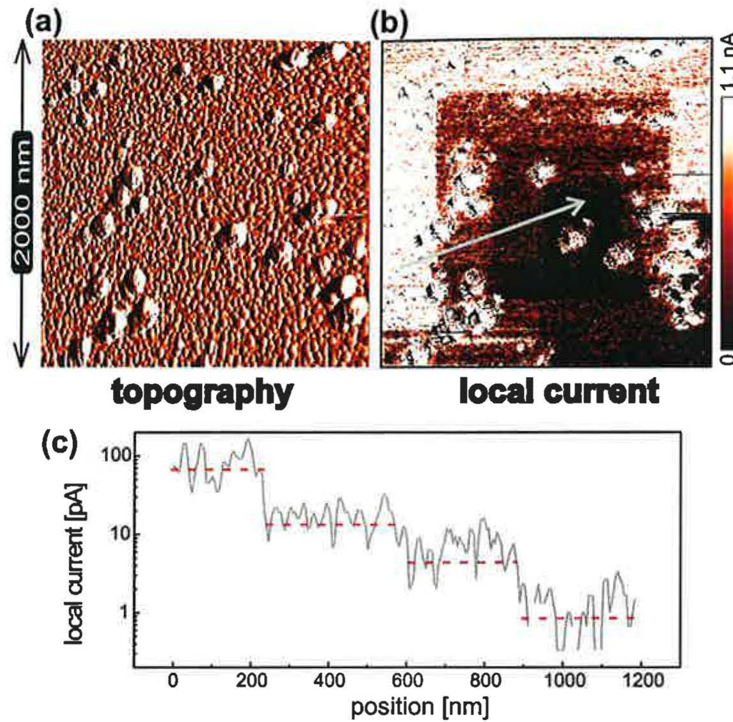

Figure 3.22: *Topography (a) and local current (b) images showing multiple memory effect on sample Stm 151 (270 nm thickness, Table 3.5). Line profile (c) shows the shows logarithmic plot of current along the arrow in (b).*

such a shift can be explained by the addition of a grain boundary on the surface of each grain, so that grains actually never touch directly (Fig. 3.23). This indicates the importance of grain boundaries which are, in fact, controlling the transport in the μc–Si:H films. Later, it will be shown that the grain boundaries are made of a–Si:H rich in H and various impurities.

3.3.4 Microcrystalline sample in detail

The complicated inner structure of completely microcrystalline surface has been measured by combined AFM in the case of 950 nm thick sample (Fig. 3.24) prepared on the bottom electrode. This sample was prepared under the same deposition conditions as the sample Stm 148 (1000 nm thickness, details in the Table 4.2). At such thickness, the surface of μc–Si:H samples is composed of large grains (conglomerates, aggregates) with diameters of 300-500 nm. Analysis of PSDF (Section 2.4.3) of the topography of this sample (Fig. 3.24(a)) reveals AGS=425 nm. The zoomed map of local current (Fig. 3.24(b)) provides better lateral resolution and shows small grains (crystallites) of 15-30 nm in size. This is even more evident in the plot of profile

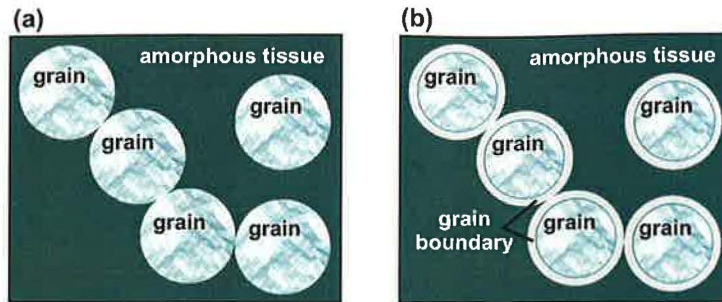

Figure 3.23: *Schematic picture of microcrystalline grains in amorphous tissue (a) and microcrystalline grains surrounded by grain boundaries which avoid a direct contact of these grains*

in Fig. 3.24(c). Based on this observation, we introduced the nomenclature of *small grains* and *large grains*, which will appear in the following text. The term "grain" without any specifying adjective will always refer to large grain (aggregate).

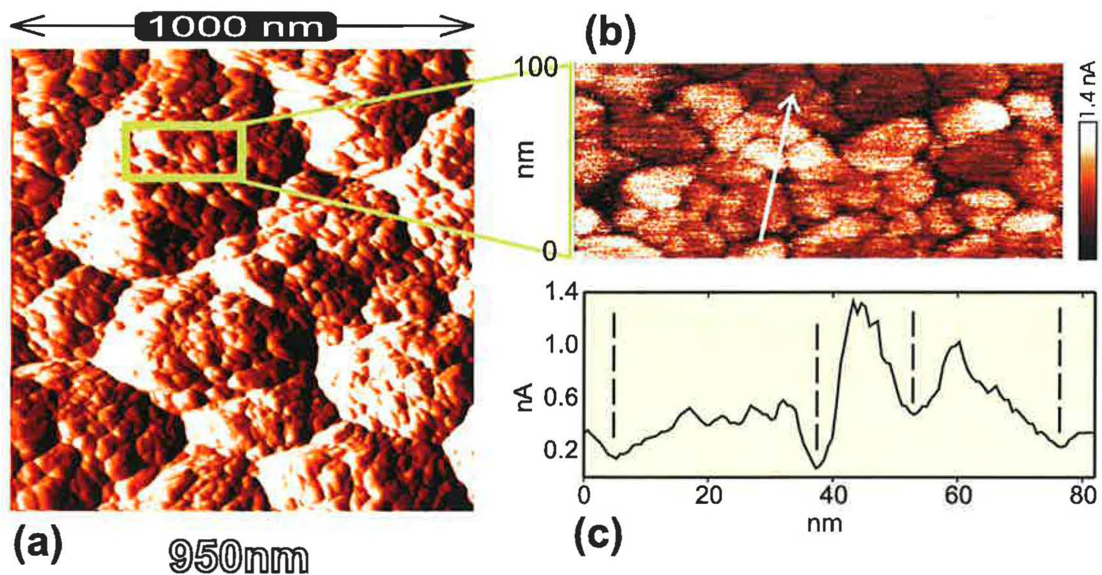

Figure 3.24: *Combined AFM measurement of the sample Stm 140 showing (a) surface topography together with (b) map of local currents of the selected region (highlighted rectangle in (a)) and the local current line profile (c) corresponding to the arrow in (b).*

The comparison of TEM pictures (Fig. 3.2) and combined AFM measurement (Fig. 3.24) brought us to the cross–sectional sketch of μc–Si:H shown in Fig. 3.25. The sizes of small grains and large grains are in agreement with results of AFM and TEM observations [178] and with the XRD data of our samples (Chapter 4). This sketch is valid for the explanation of transport properties and formation of large

grain boundaries at a certain thickness (e.g. ~600 nm). However, the spherical shape of small grains is most probably wrong.

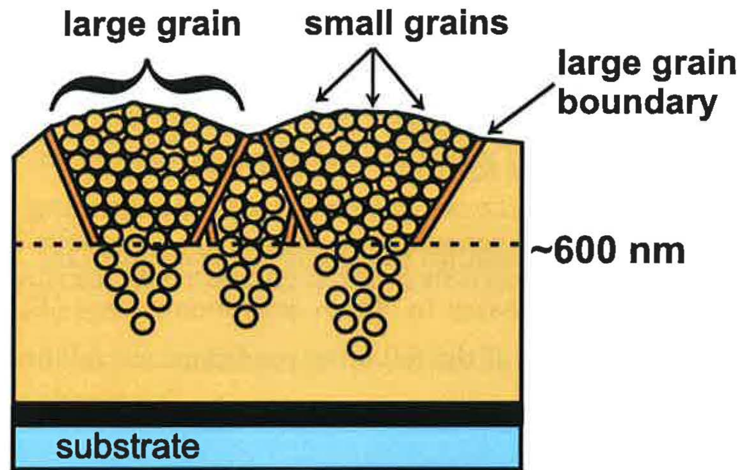

Figure 3.25: *Sketch of the mixed phase Si film showing both small and large grains participating in the formation of the structure.*

Recent cross-sectional TEM studies of the large grains show no detectable amount of a–Si:H inside of the large grains [159, 179]. Moreover the TEM pictures reveal non–spherical shape of the small grains. So, these small grains could be in fact just tilted crystallographic planes of microcrystalline structure. This would explain their detection by XRD (crystallographically sensitive method) and would also support the fact that these small grains have no influence on the transport properties [180, 110]. The sketch of tree–like inner structure of large grains thus seems to be a more precise description [181].

3.3.5 Guiding rule for μc–Si:H

The major role of large grain boundaries on the transport properties of thin Si films was clearly demonstrated, for example, by C. Droz et al. from the Neuchâtel group. They compared the structure of deposited films, evaluated the L_{diff} and proposed the following empirical relationship [135] for mixed phase Si films:

$$L_{diff} = \frac{1}{3} \sim \frac{1}{2}\ AGS \tag{3.1}$$

where:

L_{diff}	ambipolar diffusion length by SSPG (parallel to the substrate) [nm]
AGS	lateral average grain size [nm], according to Eq. 2.14

This relationship suggests to have as large grains as possible for the best transport properties. This is valid if the quality of the grain boundaries remains preserved with the increase of the grain size. However, this is not true for all the samples we have measured up to now. With the change of any deposition parameter, there is always some change of the quality of the large grain boundary.

Based on the analysis of structure and transport properties of several series of samples prepared by PECVD, we introduced a simple **guiding rule** [180] for the detection of large grain boundaries that limit the transport (Eq. 3.2). For the application of this rule it is necessary to obtain activation energy (E_a) and conductivity prefactor (σ_0) – see Eq. 2.6. If the following conditions are fulfilled:

$$\sigma_0 \geq 100\ \Omega^{-1}cm^{-1}, \qquad E_a \approx 0.5\ eV, \tag{3.2}$$

then the μc–Si:H sample should be free of defective large grain boundaries and exhibit good transport properties. This rule is valid for the μc–Si:H sample above the percolation threshold, i.e., with crystallinity of $X_C \geq 65\%$. The μc–Si:H film, which was utilized in the single junction solar cell with record efficiency ([12] in Table 1.1) exhibited the values of σ_0=127 $\Omega^{-1}cm^{-1}$ and E_a=0.49 eV. This guiding rule will be used as one of the characterization methods (Sections 4.4–4.8) to determine the sample with best transport properties suitable for the i–layer of a thin film solar cell.

3.3.6 Stress

During the study of several series of sample we had to face the peeling–off problem (Fig. 3.26). This unpleasant phenomenon is a nightmare of every thin film deposition, since it disables any further measurements. Most often, the thin films peel–off immediately after venting the deposition chamber. If they are stable for at least one week then they typically do not exhibit any peeling at all. There is no clear recipe how to avoid it, since the peeling of the film is a result of several independent factors. The basic ones are:

- too high residual stress (σ_r) in the deposited film
- poor adhesion to the substrate

In this section we will address a few issues concerning the stress in thin films. We observed that films with higher thickness exhibit a higher percentage of peeled–off samples. Recently, we introduced rough substrates (σ_{RMS} ~90 nm), which helped relax the stress and prevented even 30 μm thick films from peeling–off .

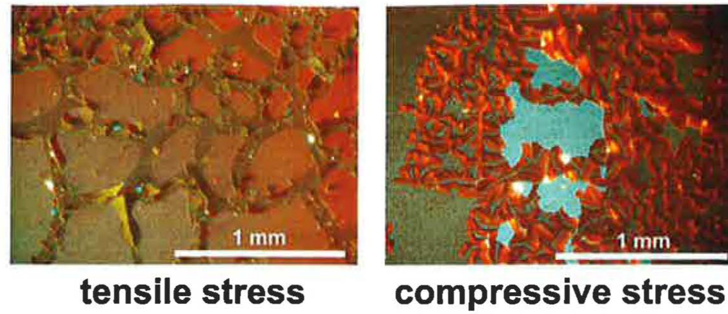

Figure 3.26: *Surface pictures by optical microscope showing the consequences of too high values of internal stress leading to the destruction of films.*

Theoretical background

Before the results on our samples will be presented, we will shortly review the theoretical issues connected with the evaluation of stress. At the macroscopic scale, the general definition of strain and stress is as follows:

$$\sigma = E_f \epsilon, \qquad \epsilon = \frac{\Delta l}{l} \tag{3.3}$$

where:

σ	total residual stress in the film [Pa]
E_f	elastic (Young's) modulus of the film
ϵ	strain of the film
Δl	change of the object dimension
l	dimension before the load was applied

At the atomic level, the strain represents the relative microdeformation, i.e., change of the lattice constant. By multiplying the micro–strain ϵ by E_f, the micro–stress can be obtained.

Three following methods are typically used for the evaluation of stress in thin films:

- bending of a long flat substrate on which the thin film was deposited
- broadening of the peaks in XRD patterns
- shift of the peak in the Raman spectra

Since these methods are based on different principles, let us shortly discuss how to understand the results obtained by each method. The sample bending method provides a value of total residual stress σ_r in the film, since the substrate curvature shows the stress provided by the whole thin film. It means that both a–Si:H and μc–Si:H structures contribute to this total stress value.

In this work we present a unique combination of stress data evaluated from XRD patterns and Raman spectra. Both methods are non–destructive and can be applied to thin films deposited on standard substrates. However, these **stress** values are obtained indirectly **from the response of the crystalline phase only**. In the case of XRD patterns the σ_r is obtained from the broadening of peaks (Section 2.3.6), while for the Raman spectra the σ_r is evaluated from the shift of the crystalline peak (Section 2.3.5). Raman measurement characterizes the film within the penetration depth d_{RCD}, which is dependent on the laser wavelength. On the other hand, the XRD provides values, which refer to the whole thin film. Now it is clear that the values of residual stress are difficult to compare between these three methods.
Residual stress σ_r in thin films may have several different contributions [182, 183]:

- thermal stress (σ_{th}) – caused by the difference of the thermal coefficients of the film and substrate [184]:

$$\sigma_{th} = (\alpha_s - \alpha_f)(T_{room} - T_{deposition})\frac{E_f}{1 - \nu_f} \tag{3.4}$$

  where α_f and α_s are thermal expansion coefficients of the film or substrate, respectively, T_{room} and $T_{deposition}$ are the temperatures of measurement and deposition, E_f is the elastic (Young) modulus of the film and ν_f is the Poisson's ratio of the film

- interfacial stress – caused by the differences in structural properties of the film and substrate

- intrinsic (inner) stress – result of the growth process, which has created atomic scale disorder. Typically, the tensile stress reflects the presence of structural defects (voids) and columnar structure [185]. The compressive stress is associated with the presence of contaminants.

The Eq. 3.4 is constructed to keep to the stress sign convention, which is "−" for compressive and "+" for tensile stress. Typical constants used in this work are taken from [143, 186]: E_f=169.2 GPa, ν_f=0.278.

Results of measurements
With all this in mind, let us have a look at the data measured on our samples. The Figs. 3.27, 3.28 & 3.29 show the value of residual stress σ_r present in the microcrystalline grains of the thin Si films. The XRD data refer to the entire grains, while Raman data indicate the σ_r in their upper ~100 nm. All figures represent the series

of samples described in Chapter 4. Here, it is enough to comment that in all series the a–Si:H/μc–Si:H transition (highlighted by a grey stripe) is crossed.

In the works, where the sample bending method was used [187, 53, 188], the σ_r values reached compressive stress around 1 GPa. This value itself cannot be compared, but in all these works a peak in σ_r for the mixed–phase samples was observed. In the case of all our samples we observe increased values for the mixed–phase samples. Since the values and type of σ_r may significantly differ with deposition and also measurement conditions [136], it is not much surprising to find the high tensile stress for our samples. Interesting is the fact that also the σ_r in microcrystalline grains only also exhibits some changes within the transition zone.

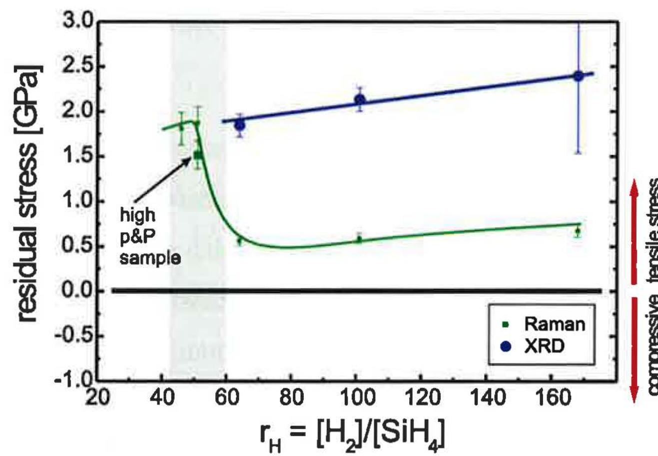

Figure 3.27: *Residual stress in the thin Si films of the dilution series at 80° C (Section 4.6) evaluated from XRD patterns and Raman spectra.*

The comparison of XRD and Raman data in the figures is a sort of probe to different depths. In both Figs. 3.27 and 3.28 the σ_r is always higher for the entire grains (XRD) than for the top 100 nm part. This means that the conical parts of grains close to the substrate, which are in touch with a–Si:H phase are exposed to the tensile forces, i.e., the a–Si:H deposited at 80° C probably tends to shrink and thus dilates the μc–Si:H structure.

High T_S is often the source of the thermal component σ_{th}. Using Eq. 3.4 with α_f=2.57 10^{-6}/°C for μc–Si:H (adopted from c-Si [189, 190]) and α_s=4.6 10^{-6}/°C for Corning 7059 [191] for the highest $T_{deposition}$=250° C we get σ_{th} ~ -0.1 GPa. In case of a–Si:H film (α_f=4.4 10^{-6}/°C [192]) on Corning 7059 the σ_{th} is even lower ~ -0.01 GPa. It is clear that the thermal component σ_{th} cannot be responsible for the values observed in Figs. 3.27– 3.29. The increase of σ_r at lower T_S also eliminates the importance of σ_{th}.

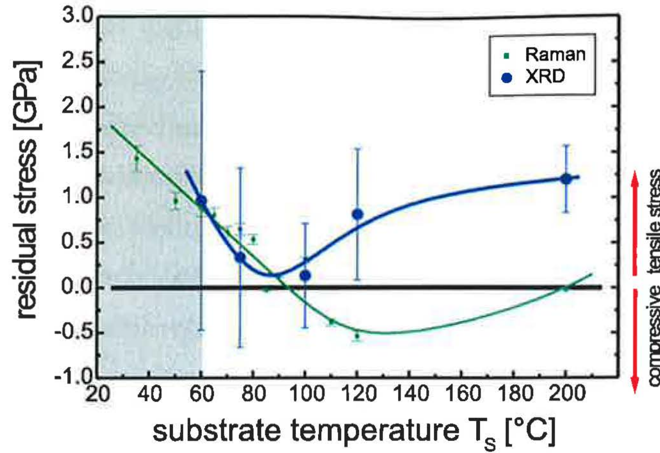

Figure 3.28: *Residual stress in the thin Si films of the VHF temperature series (Section 4.7) evaluated from XRD patterns and Raman spectra.*

Figs. 3.28 & 3.29 show that the shift to the mixed–phase structure (with typically larger or even isolated grains) gives rise to the tensile σ_r. On the other hand, at higher T_S, when the grains are in touch and compete with each other, the compressive stress appears. Slightly higher values of σ_r for the red laser probing deeper (d_{RCD} ~360 nm) compared to our standard green laser measurement (d_{RCD} ~90 nm) is in agreement with the data published in [136]. The visual check of the samples of these three series, revealed the peeling–off in case of three samples with $T_S \geq 190$ °C (Fig. 3.29). These are the only samples with higher values of compressive stress, which seems to be more critical for the peeling–off, as concluded in [53].

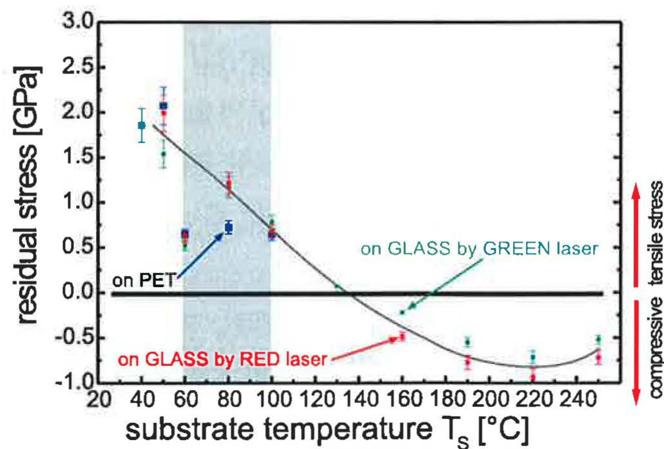

Figure 3.29: *Residual stress of the thin Si films of the RF temperature series (Section 4.8) evaluated from Raman spectra. The figure shows σ_r of Si films on PET substrate and glass evaluated from two measurements with different penetration depths d_{RCD}.*

Chapter 4

CONTROLLING THE PROPERTIES

4.1 Motivation

To control the resulting properties of the silicon thin films several major parameters of the deposition process can be tuned. For the demonstration of the role and influence of the key deposition parameters we will show several series of samples prepared by Plasma Enhanced Chemical Vapour Deposition (PECVD) technique, which was used in this work.

To keep the production costs competitive, there seem to be two key parameters worth attention in the case of conventional PECVD. First, the deposition at low substrate temperatures ($T_S \leq 100°$ C) slightly reduces the deposition time and costs and mainly opens the way for the plastic substrates, which are interesting not only for their low price but also for their mechanical properties (flexibility). Second, further reduction of the production costs could be achieved via substantial increase of the deposition rate r_d. All these issues are addressed within this work, the deposition at lower substrate temperatures (Sections 4.7 & 4.8) and a test of the higher deposition rate (Section 4.10).

The structure of the μc–Si:H film has a direct impact on the electronic properties of the film. To see the influence of the structure only, we attempted to study several thickness series of samples (section 4.4). Some selected samples prepared in the meantime were already described in the previous chapter 3 highlighting some special features of the a–Si:H and μc–Si:H material. The first two thickness series were deposited at higher substrate temperature (250° C), while for the third one we decreased this temperature to ~80° C only (section 4.5). We continued with the dilution series at the low substrate temperature (section 4.6) and we expanded the study

of the amorphous and microcrystalline Si films by two series with variable substrate temperature prepared in two different deposition systems (sections 4.7 and 4.8).

4.2 Systemization of results

All the series crossed the border between amorphous and microcrystalline growth. The mixed phase samples are marked by extra grey stripe in the graphs.

The review of properties usually starts with the sample *crystallinity data* (X_C) from the Raman scattering (Section 2.3.5) together with the values of *dark conductivity* σ_d (Section 2.3.2). The comparison with *CPM data* (Section 2.3.4) confirms the estimated structure and additionally provides a measure of defects in the sample. The *AFM* (Section 2.4.2) was performed on Si films grown on glass in the middle of the stripes of bottom contacts, see Fig. 2.3. The combined AFM, measured above the bottom electrodes, gives the additional information on relation between microstructure and its local conductivity. The *surface RMS roughness* (Section 2.13) taken from air–AFM measurements is then shown together with the *ambipolar diffusion length* L_{diff} from SSPG (Section 2.3.3). We also attempt to correlate the lateral *AGS* - Average Grain Size (Section 2.4.3) with the values of SSPG L_{diff}. Finally we judge the quality of deposited films and their transport properties using L_{diff} together with the values of *activation energy* E_a and *conductivity prefactor* σ_0 (Section 2.3.2). The combined plot of E_a and σ_0 in a special scale will graphically emphasize the samples fulfilling the conditions of our suggested *'guiding rule'* (Section 3.3.5) for the samples with expected good transport properties. In special cases we would show some details concerning the structure of samples, namely preferential crystallographic orientation and typical size of crystallites obtained from the analysis of XRD patterns (Section 2.3.6). Finally, for a better understanding of the behaviour of some samples, the amount of hydrogen incorporated in the films detected by ERDA and FT–IR (Section 2.3.7) had to be taken into account. The lines in the graphs are added as a guide for the eye.

Based on all the described characteristics we will always try to suggest the **'BEST SAMPLE'** of the series, i.e., the sample with the best structural and electric properties that we expect would work as the best i–layer in the thin film Si solar cell. Such a sample would be denoted by the dashed circle or elipse in the presented graphs.

4.3 Substrates

The basic parameter of the sample is the substrate material used to hold the thin film. The most common type of substrate is *glass* because of its low price and availability. Specialized types of glass were developed for the deposition of solar cells – the best known and most used is Corning #7059 glass capable of T_S up to 800° C. All the substrates in this work indicated as glass always refer to Corning #7059.

Another type of cheap substrate is steel or stainless steel, which is widely used for depositions of films with special mechanical properties. However, high conductivity of steel does not allow to study electrical properties of the deposited films. With the aim to study really cheap substrate materials suitable also for electrical applications we employed 0.2 mm thick PET foil, which, on the other hand, imposes quite strong restrictions of T_S values (typically T_S must not exceed 100° C). To measure some properties, like hydrogen bonding by infrared spectroscopy, single crystal silicon substrate is required too. Substrates were cleaned in the ultrasonic bath for few minutes and then degassed in UHV just before the deposition of Si film.

In one deposition run we usually deposit Si film on several pieces of different substrates (some substrates are bare, some are covered with bottom electrodes – see Fig. 2.3) to be able to perform a complex characterization of the films by several diagnostic techniques introduced in the Sections 2.3 and 2.4.

4.4 Structure evolution in the thickness series at 250°C

The series of samples with variable film thickness were deposited by varying deposition time. All the samples undergo the same deposition conditions, so we can suppose that the nucleation density, deposition rate and surface chemical reactions would be the same. The key deposition parameters are listed in the Tables 4.2 and 4.4. As we aimed to study the properties of μc–Si:H samples, we adjusted the value of hydrogen dilution r_H to 21 (4.5%) or 32 (3%), respectively, to achieve the growth of the μc–Si:H structure. For a typical a–Si:H sample the value of r_H would be 12 or less as we used in Section 3.2.8 to introduce a–Si:H sublayer.

The samples of the thickness series at T_S=250° C (Section 4.4) were prepared in the PECVD chamber at the Department of Thin Films, IoP in Prague. They are denoted as "Stm #", where the # sign stands for the sequential number of the deposition.

Tables 4.2 and 4.4 show the main deposition parameters. The thickness of deposited films given in the first column was measured by the contact profilometer (Section 2.3.1). The Table 4.1 provides more parameters of the deposition and also shows the deposition rate r_d – an averaged value of the samples with identical r_H. Most of the results of these two thickness series at 250° C were not published, but they are consistent with the data of similar thickness series published earlier [169, 108].

Table 4.1: *Additional deposition parameters of the samples of two thickness series at 250° C. Main deposition parameters are in Tables 4.2 & 4.4.*

Average deposition rate r_d	~0.17 nm/s for r_H=21
	~0.12 nm/s for r_H=32
Plasma power density	~0.23 W/cm^2
Substrate potential	U_{fl}
Cathode peak to peak voltage	~550 V
Cathode bias voltage	~-150 V

4.4.1 Samples with r_H=21 (∼4.5 % dilution)

Table 4.2: *Overview of the main deposition parameters of the samples of the thickness series at 250° C with r_H=21.*

Sample	d [nm]	dil. r_H	T_S [°C]	f_{exc} [MHz]	P_{eff} [W]	p_{tot} [Pa]	$[H_2]$ [sccm]	$[SiH_4]$ [sccm]
Stm 166	200							
Stm 164	500							
Stm 148	1000	21	250	13.56	9.0	70	38.4	1.8
Stm 146	1500							
Stm 134	2200							

As seen from the Raman crystallinity data in Fig. 4.1 (X_C column in Table 4.3), most of the samples with 4.5 % dilution show rather high crystalline volume fractions. Only the thinnest sample Stm 166 (200 nm) exhibits evidently smaller crystallinity around 70 %, while all the thicker samples approach the saturated value between 85 and 90 %. The dark conductivity σ_d shows the same trend - smaller value ∼ 10^{-10} $\Omega^{-1}cm^{-1}$ for the thinnest sample and values above σ_d above 10^{-7} $\Omega^{-1}cm^{-1}$ for all the other samples. The saturated values of X_C and σ_d with increasing film thickness indicate that these samples consist of one major phase – microcrystalline silicon.

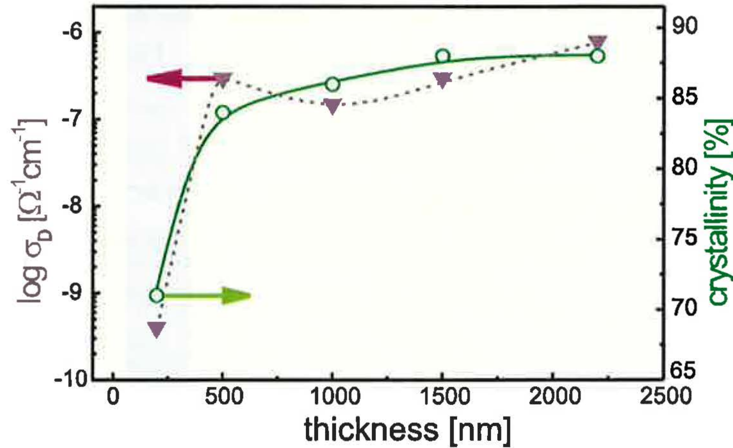

Figure 4.1: *Crystalline volume ratio (X_c) together with values of dark conductivity (σ_d) of the samples of the 250° C thickness series at r_H=21.*

Further support for the estimation of sample structure comes from the measurements of absorption coefficient α by the Constant Photocurrent Method (CPM) (Section 2.3.4). In the Fig. 4.2, all the samples with thickness above 1000 nm follow a slightly shifted trend compared to the single crystal Si indicated in the figure by the

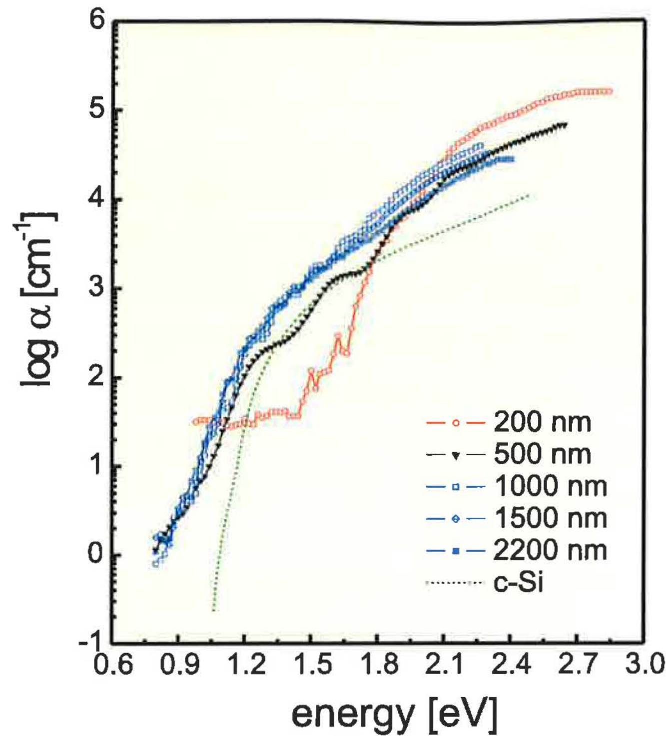

Figure 4.2: *CPM spectra of the samples of the 250° C thickness series at r_H=21.*

dashed line. Using the knowledge of CPM spectra of typical a–Si:H and μc–Si:H samples [122], we can identify the samples above 1000 nm to be microcrystalline and the thinnest sample Stm 166 (200 nm) to be amorphous. The CPM spectrum of sample Stm 164 (thickness 500 nm) clearly differs from the spectrum of thicker samples in the range of 1.2–1.8 eV. This indicates some type of combined a–Si:H and μc–Si:H response, which occurs for the mixed–phase structure.

Let us look at the AFM topography pictures of the samples (Fig. 4.3) to confirm the estimations of the structure based on X_C, σ_d and CPM spectra.

Topography of first two samples is shown in the standard field of view 1×1 μm, while the next three ones are shown in a larger scale, i.e., 2.5×2.5 μm. No matter what the measured area is, the surface images clearly show the same type of structure for the samples Stm 134, Stm 146 and Stm 148 (thickness 2200, 1500 and 1000 nm), a bit more rough for the latter one. The sample Stm 164 (500 nm) reveals a similar surface structure consisting of smaller grainy objects homogeneously distributed all–over the entire surface. According to the values of X_C and σ_d in Fig. 4.1, this type of structure could be assigned to μc–Si:H. In the case of the thinnest sample Stm 166 (200 nm), the surface exhibits a different structure consisting of rather large circular objects and smoother surrounding area. Previous combined AFM measurements of similar sam-

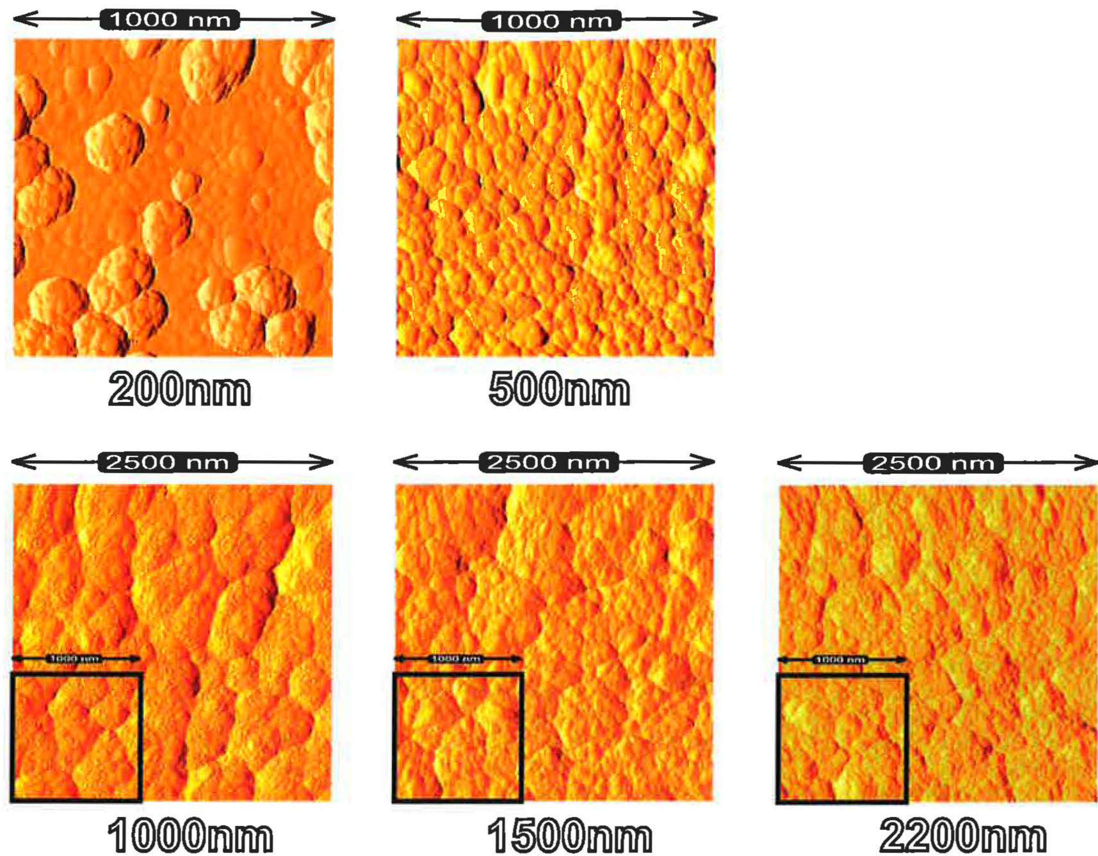

Figure 4.3: *AFM images of the samples of the 250°C thickness series at r_H=21. Numbers below the images indicate the thickness of each sample. Note the different fields of view used for the first and second row.*

ples [154] indicate that this is the mixed–phase structure composed of microcrystalline grains surrounded by amorphous tissue. So, for the series with **fixed 4.5 % dilution (r_H=21) and variable film thickness, the transition from amorphous to microcrystalline structure occurs in the range of 100–350 nm.**

Fig. 4.4 shows the plot of the surface roughness values evaluated from the AFM images in Fig. 4.3 (always from the 1×1 μm field of view). The transition to μc–Si:H structure occurred around the thickness of 350 nm and so the plot of roughness shows just one value for the mixed phase (sample Stm 166 (200 nm)). For the sample Stm 164 (500 nm) with fully microcrystalline surface, the coalesced grains create smoother surface (σ_{RMS} ~8 nm). The last three samples (1000, 1500 and 2200 nm) exhibit more roughened type of microcrystalline structure with σ_{RMS} ~20 nm. This is probably a result of the competition among grains during their further growth: while the 1×1 μm image of 200 nm thick sample shows ~15 grains with an average diameter of ~180 nm (AGS column in Table 4.3), the same area of the samples above

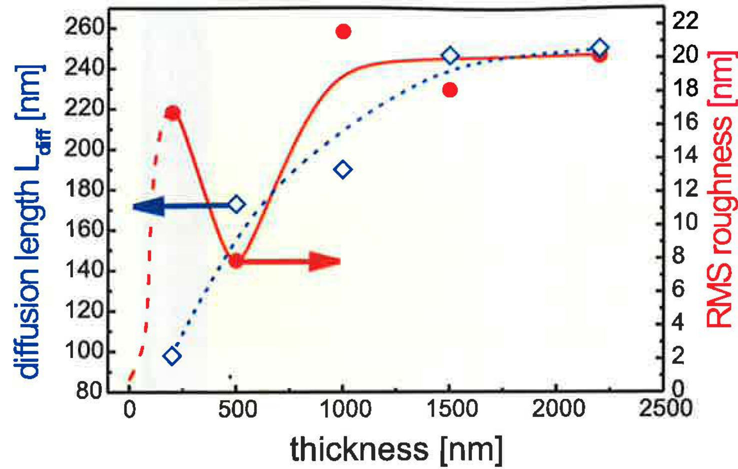

Figure 4.4: *Surface RMS roughness together with ambipolar diffusion length (L_{diff}) of the samples of the 250°C thickness series at r_H=21.*

1000 nm exhibits hardly a half of this number of grains. This is also reflected in the AGS exceeding 500 nm. The trend of roughening of the μc–Si:H surface is saturated above 1000 nm – see the plateau of σ_{RMS} in Fig. 4.4).

Another important feature is the ambipolar diffusion length L_{diff} obtained from SSPG (Section 2.3.3). The typically amorphous value (L_{diff} ~100 nm) for the 200 nm sample increases almost up to L_{diff} ~250 nm typical for the best μc–Si:H thin films. The trend of L_{diff} reflects the general transport behaviour of the entire thin film:

- lower L_{diff} for the mixed phase, where some isolated microcrystalline grains are present, but where the transport is still dominated by the amorphous tissue (thickness up to 200 nm).
- increasing L_{diff} for the samples that may exhibit microcrystalline surface structure, but the transport properties are determined by the mixture of microcrystalline grains and remaining amorphous tissue (500–1000 nm thickness).
- saturated values of L_{diff} (close to the values of fully μc–Si:H) for the samples, where the transport is dominated by the microcrystalline structure (thickness above 1500 nm).

The saturated values of X_C and σ_d in Fig. 4.1 and surface images in Fig. 4.3 may arouse a false deduction that the structure and properties of the samples with thickness above 500 nm are almost the same.

However, the reality is different! The measurements of transport properties in the direction parallel to the substrate (L_{diff} in the Fig. 4.4) and the dark conductivity

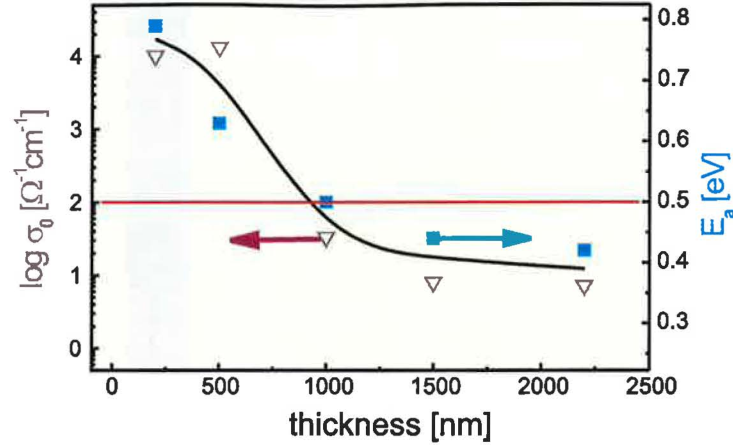

Figure 4.5: *Activation energy (E_a) together with conductivity prefactor (σ_0) of the samples of the 250°C thickness series at r_H=21.*

characteristics (E_a and σ_0 in Fig. 4.5) indicate the evolution of electrical properties of μc–Si:H structure up to the thickness of 1500 nm. The values of activation energy E_a further confirm that the 200 nm sample is amorphous (E_a=0.79 eV). In the case of the 500 nm sample (Stm 164) we measured surprisingly high E_a=0.63 eV meaning that the electronic transport is still influenced by the amorphous phase.

Our guiding rule (Section 3.3.5) is applicable just for the microcrystalline samples – with crystallinity $X_C \geq 70\%$ [110, 193]. The solid horizontal line graphically represents the conditions of the guiding rule and it is nicely visible that it is fulfilled by the 500 nm sample and almost fulfilled by the 1000 nm sample.

The correlation between the diffusion length L_{diff} and the AGS (Section 2.4.3) L_{diff}/AGS $\sim$ 0.3–0.5 (Eq. 3.1) is quite well fulfilled within the whole series (see the AGS column of Table 4.3) confirming the fact that the transport in mixed phase and microcrystalline silicon thin films is determined by the density and size of large grains and their boundaries.

Table 4.3: *Summary of the properties – thickness series at 250° C with r_H=21.*

Sample	X_C [%]	RMS [nm]	AGS [nm]	L_{diff} [nm]	σ_d [$\Omega^{-1}cm^{-1}$]	σ_0 [$\Omega^{-1}cm^{-1}$]	E_a [eV]
Stm 166 (200 nm)	71.0	16.7	182	98	4.0×10^{-10}	1.0×10^{4}	0.79
Stm 164 (500 nm)	84.0	7.9	167	173	3.0×10^{-7}	1.3×10^{4}	0.63
Stm 148 (1000 nm)	86.0	21.6	500	190	1.5×10^{-7}	3.3×10^{1}	0.50
Stm 146 (1500 nm)	88.0	18.2	555	247	3.0×10^{-7}	8.0×10^{0}	0.44
Stm 134 (2200 nm)	88.0	20.2	555	250	8.0×10^{-7}	7.2×10^{0}	0.42

4.4.2 Samples with r_H=32 (~3 % dilution)

Table 4.4: *Overview of the main deposition parameters of the samples of the thickness series at 250° C with r_H=32.*

Sample	d [nm]	dil. r_H	T_S [°C]	f_{exc} [MHz]	P_{eff} [W]	p_{tot} [Pa]	$[H_2]$ [sccm]	$[SiH_4]$ [sccm]
Stm 160	30							
Stm 155	70							
Stm 159	170							
Stm 156	320	32	250	13.56	9.0	70	50	1.6
Stm 157	700							
Stm 158	1000							
Stm 163	2000							

The crystallinity data in the Fig. 4.6 (X_C column in Table 4.5) show the same trend as in the case of the 4.5% dilution series (Fig. 4.1). The series with 3% dilution only includes more samples with lower film thickness, so there are more data points at the a–Si:H/μc–Si:H transition. The thinnest sample Stm 160 (30 nm) did not provide sufficient signal to perform electrical measurements, so the only available characteristics of this sample is surface roughness (Fig. 4.10). From the comparison with the thickness series with 4.5% dilution in previous section we can expect this very thin sample to be completely amorphous.

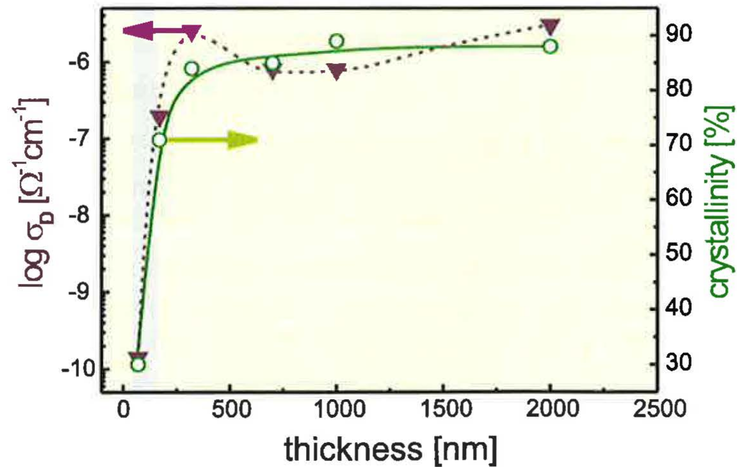

Figure 4.6: *Crystalline volume ratio (X_c) together with values of dark conductivity (σ_D) of the samples of the 250° C thickness series at r_H=32.*

The mixed–phase samples Stm 155 and Stm 159 (70 and 170 nm) with 30% and 71% crystallinity X_C exhibit also corresponding dark conductivities σ_d. For the

X_C=30%, σ_d is in the 10^{-10} $\Omega^{-1}cm^{-1}$ range, i.e., 'amorphous side' of the mixed–phase structure and for the X_C=71%, σ_d is in the 10^{-7} $\Omega^{-1}cm^{-1}$ range, which is quite close to the saturated values of μc–Si:H. The other samples Stm 156–Stm 163 (320–2000 nm) exhibit typical microcrystalline values, i.e., X_C ~90% and σ_d in the 10^{-7}–10^{-6} $\Omega^{-1}cm^{-1}$ range.

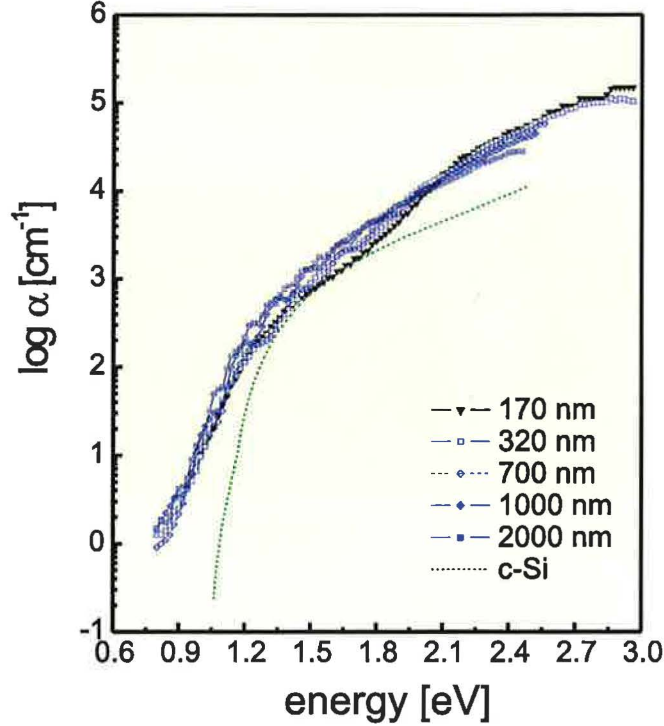

Figure 4.7: *CPM spectra of the samples of the 250°C thickness series at r_H=32.*

The CPM measurements (Fig. 4.7) of the absorption coefficient α again support the estimations of the sample structure based on X_C and σ_d. The samples with thickness above 320 nm are microcrystalline (according to the shape of their CPM spectra [122]). The CPM spectrum of Stm 159 (170 nm) is the only slightly different spectrum with a visible downshift of α in the 1.5–2.1 eV range. A similar shift was observed for the mixed–phase sample of the previous thickness series with 4.5% dilution (Fig. 4.2). The two thinnest samples Stm 160 and Stm 155 (30 and 70 nm) did not provide sufficient CPM signal.

The AFM surface pictures in Fig. 4.8 are entirely analogous to the pictures of the previous 4.5% dilution series (Fig. 4.3). Based on X_C and σ_d values (Fig. 4.6), the samples with 70 and 170 nm thickness are considered to have the mixed–phase structure. The AFM surface pictures (Fig. 4.8) confirm this finding, especially in the case of the 70 nm sample with combined structure of interconnected microcrystalline

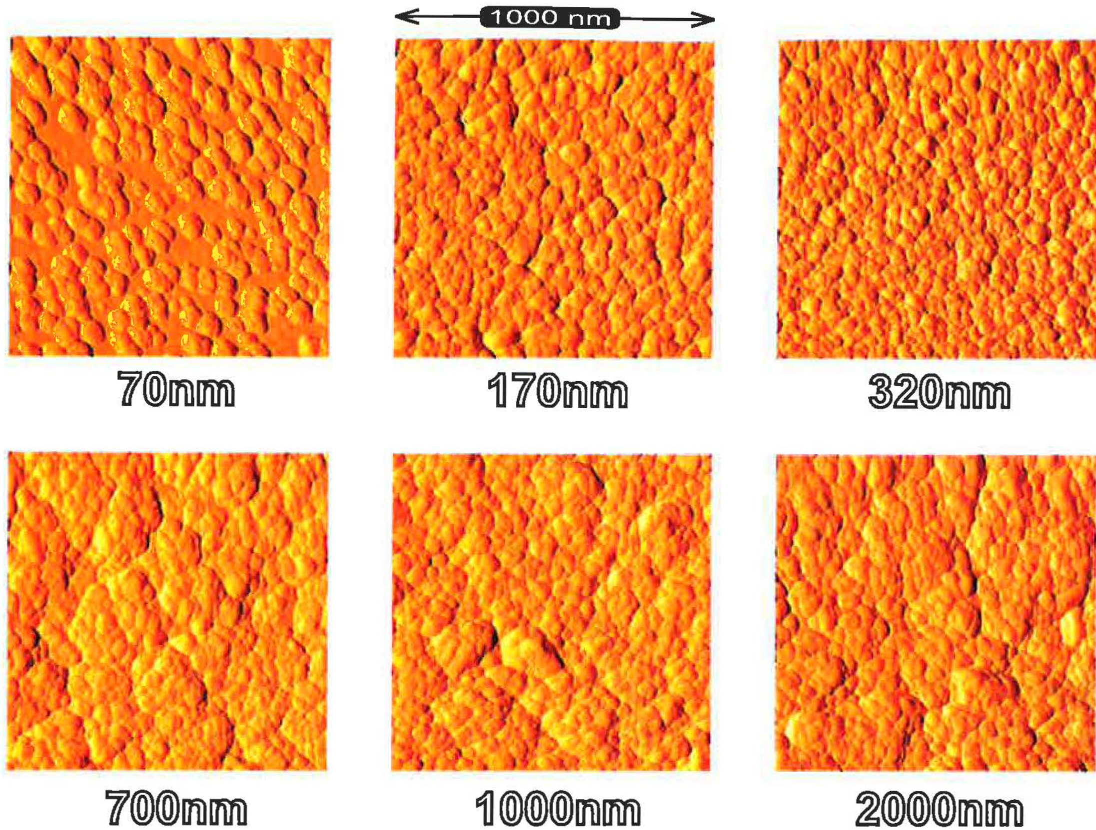

Figure 4.8: *AFM images of the samples of the 250°C thickness series at r_H=32. Numbers below the images indicate the thickness of each sample.*

grains and remaining amorphous tissue in between. The 170 nm sample is quite close to μc–Si:H structure, so the surface is already fully microcrystalline. Topography of the 320 n sample is very similar to the 170 nm sample. At higher thicknesses (above 700 nm) the topography shows the same type of structure, but more rough (see σ_{RMS} in Fig. 4.10) and with slightly larger grains. Supposing the constant nucleation density, these larger grains were probably created by the coalescence of growing grains.

Here, it is possible to make some comparison of the 4.5 % and 3 % dilution series. It seems that after reaching a certain thickness, samples in both series exhibit microcrystalline structure with the same X_C and σ_d values. For the series with **fixed 3.0% dilution (r_H=32) and variable film thickness, the transition from amorphous to microcrystalline structure occurs in the range of 50–170 nm.**

The topography pictures in Figs. 4.3 and 4.8 show the structure of thin Si films as they have grown directly on glass substrate.

However, for a successful measurement of the maps of local currents (Section 3.3.1), the presence of the bottom electrode is essential. This is clearly demonstrated in

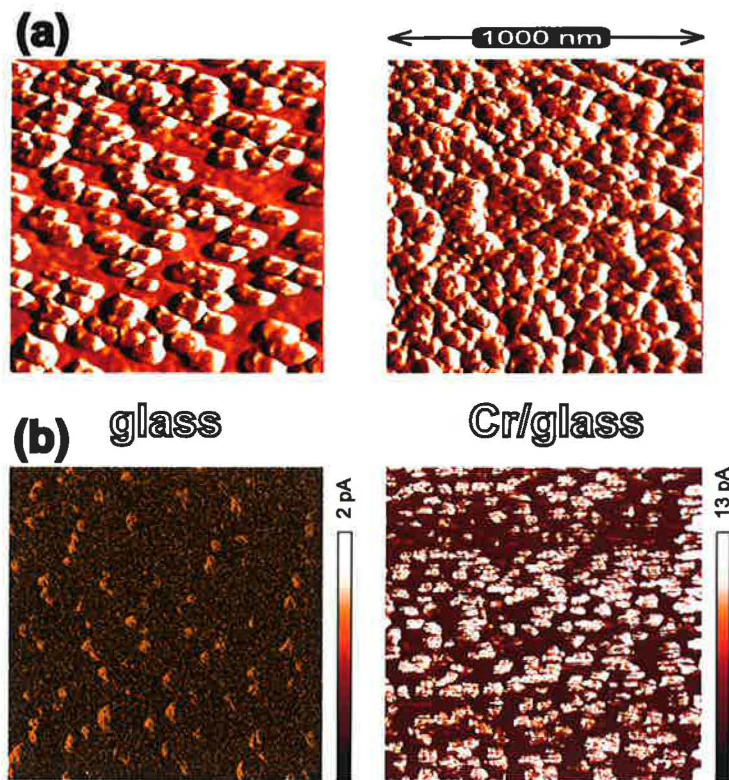

Figure 4.9: *Combined AFM images of (a) topography and (b) map of local currents (bias voltage +5 V) of the 70 nm sample (Stm 155) measured on glass substrate (left column) and on glass substrate covered with Cr electrode (right column).*

Fig. 4.9(b), where we attempted to measure maps of local currents of Si film deposited on glass and Cr coated glass. The left image (on glass) shows some slightly brighter spots in the places, where the microcrystalline grains appear in topography. Almost the whole scanned area provides current signal below the sensitivity of the detection system. The main reason for the weak signal is the serial resistance of the Si film – the local current must flow parallel to the substrate ~0.5 mm through the Si film to reach the bottom Cr electrode.

The measurement in the right image (on Cr coated glass) is quite different. The current is flowing from the coated cantilever through the Si film (70 nm thin) to the bottom electrode. As a result, the local current signal at the same bias voltage is almost one order higher and provides much better contrast. The usage of conductive PtIr coated cantilever is responsible for slightly lower resolution in Fig. 4.9 compared to uncoated Si cantilever used in Fig. 4.8.

The trend of the RMS roughness (Fig. 4.10) is again similar to the previous series with 4.5% dilution. The surface of the thinnest sample (30 nm) exhibited very small RMS roughness, virtually corresponding to a value typical for a glass substrate. The

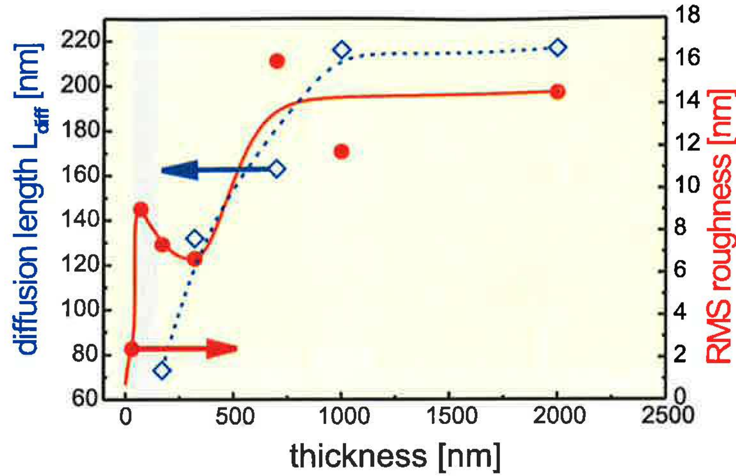

Figure 4.10: *Surface RMS roughness together with ambipolar diffusion length (L_{diff}) of the samples of the 250°C thickness series at r_H=32.*

plot of roughness firstly shows a maximum for the mixed–phase at 70 nm and then a decrease due to surface smoothing for the thicker samples (170 and 320 nm). Above 700 nm, there is surface roughening and saturation of RMS roughness (Fig. 4.4). The three thickest samples also show larger grain diameters ~220 nm instead of ~100 nm for the thinner samples (see AGS column in Table 4.5).

The plot of L_{diff} is quite similar to the plot of L_{diff} in Fig. 4.4, i.e., increasing L_{diff} with increasing film thickness, which is a natural consequence of the gradual interconnection of microcrystalline grains. In the case of the 3% thickness series (Fig. 4.10), all the L_{diff} values are a bit smaller than for the 4.5% thickness series (Fig. 4.4). The amorphous L_{diff} values are around ~70 nm at the thickness of 70 nm, then the L_{diff} increases up to ~220 nm for the thickest samples. Above the thickness of 1000 nm (Fig. 4.10) or above 1500 nm (Fig. 4.4) L_{diff} shows a plateau indicating the fact that the transport is fully dominated by the μc–Si:H.

The average grain size of this thickness series is not in such a good agreement with L_{diff} after the rule in Eq. 3.1: L_{diff}/AGS ~ 0.3–0.5. However, the values of AGS have the same increasing trend as L_{diff}. For the sample Stm 156 (320 nm) we even obtained L_{diff} >AGS. This indicates that the grain boundaries in this particular sample are not limiting the transport parallel to the substrate. This is in agreement with our guiding rule (Section 3.3.5) represented by the horizontal line in Fig. 4.11. All the μc–Si:H samples between 170 and 700 nm fulfill this rule.

Otherwise, the conductivity characteristics – E_a and σ_0 in Fig. 4.11 exhibit a monotonously decreasing trend, which does not correspond to the plateau of X_C, σ_d

and L_{diff} for the μc–Si:H samples. It means that the quality of grain boundaries is still changing with increasing film thickness and we expect the defective large grain boundaries to be formed above 700 nm.

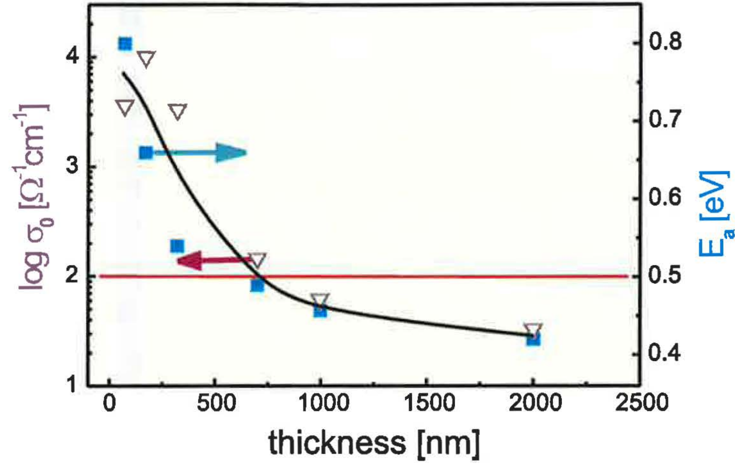

Figure 4.11: *Activation energy (E_a) together with conductivity prefactor (σ_0) of the samples of the 250°C thickness series at r_H=32.*

Table 4.5: *Summary of the properties – thickness series at 250° C with r_H=32.*

Sample	X_C [%]	RMS [nm]	AGS [nm]	L_{diff} [nm]	σ_d [$\Omega^{-1}cm^{-1}$]	σ_0 [$\Omega^{-1}cm^{-1}$]	E_a [eV]
Stm 160 (30 nm)	–	2.4	–	–	–	–	–
Stm 155 (70 nm)	30.0	9.0	83	–	1.4×10^{-10}	3.6×10^{3}	0.80
Stm 159 (170 nm)	71.0	7.3	100	73	2.0×10^{-7}	1.0×10^{4}	0.66
Stm 156 (320 nm)	84.0	6.7	87	132	2.5×10^{-6}	3.3×10^{3}	0.54
Stm 157 (700 nm)	85.0	16.0	222	163	8.0×10^{-7}	1.5×10^{2}	0.49
Stm 158 (1000 nm)	89.0	11.7	218	216	7.9×10^{-7}	5.1×10^{1}	0.46
Stm 163 (2000 nm)	88.0	14.5	246	217	3.0×10^{-6}	3.0×10^{1}	0.42

4.5 Structure evolution in the thickness series at 75°C

Table 4.6: *Overview of the main deposition parameters of the samples of the thickness series at 75° C.*

Sample	d [nm]	dil. r_H	T_S [°C]	f_{exc} [MHz]	P_{eff} [W]	p_{tot} [Pa]	$[H_2]$ [sccm]	$[SiH_4]$ [sccm]	r_d [nm/s]
Ge 01	40								
Ge 03	70								
Ge 06	100	29	75	54	45	38	50	1.7	~0.1
Ge 08	450								
Ge 10	1000								

The third thickness series was deposited at 75° C by Dr. Christian Koch from IPE, Stuttgart University, Germany. With the aim to study the growth of isolated microcrystalline grains the r_H was shifted close to the transition between a–Si:H and μc–Si:H growth. Based on the previous experiments in the same deposition chamber [47, 48], the value was r_H=29 (c_{SiH_4} ~3.3%). Due to other deposition conditions (Table 4.6) that were quite different from the previous thickness series (Table 4.2, mainly T_S and f_{exc}), the values of the dilution ratio r_H cannot be simply compared.

After the preparation and some basic measurements at IPE, we continued in the characterization of these samples using as many techniques as possible. However, the different design of the samples and some obstacles with low signals made some measurements impossible. Basically, the better the samples for the analysis of structure (Section 3.2.5 and Figs. 4.13–4.14), the worse samples for the measurements of electronic properties. This is then reflected in the summary Table 4.7. The name of the samples "Ge #" simply comes from "Growth evolution" and the # sign stands for the sequential number of the deposition. The results obtained in our laboratory on the samples of this thickness series from IPE Stuttgart were published in the joint papers [163, 164].

Within this thickness series the structure of the deposited films undergoes a transition from amorphous to microcrystalline structure too. The thinnest samples Ge 01, Ge 03 and Ge 06 (40, 70 and 100 nm) exhibit typical amorphous CPM spectra with lower values of α between 1.2 and 2.0 eV compared to single crystal Si (c-Si) in Fig. 4.12. The CPM spectrum of the sample Ge 08 (450 nm) shows signs of a mixed–phase,

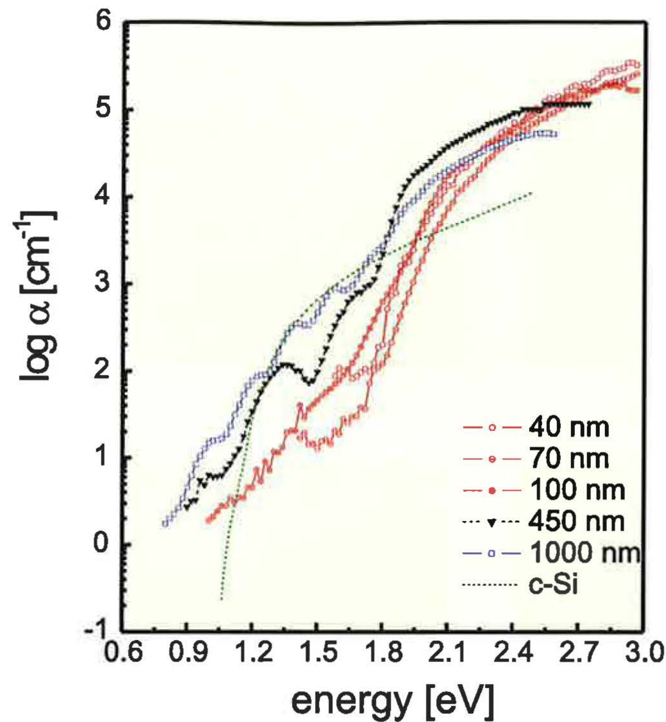

Figure 4.12: *CPM spectra of the samples of the 75°C thickness series.*

i.e., smaller values of α below 1.8 eV and higher α values above 1.8 eV compared to the thickest sample Ge 10 (1000 nm) with typical μc–Si:H CPM spectrum.

The transition is even more visible in the case of AFM surface images in Fig. 4.13. The topography undergoes a transition from a rather smooth amorphous surface with only a few small isolated microcrystalline grains (40 and 70 nm sample) to rough, fully microcrystalline surface composed of large grains with a typical cauliflower structure (450 and 1000 nm sample). After overcoming the incubation amorphous layer the circular grains protruding above the amorphous tissue start to develop (40 nm). At the thickness of 100 nm, grains start to collide with their neighbours, forming first grain boundaries. At this thickness a variation of the grain diameters (samples of 70 and 100 nm thickness) can be observed, indicating that the grain nucleation occurs not only at the film/substrate interface but also later during the growth of the film. We assume that that the smaller grains must have started to grow later (in upper layers), thus having not enough time to develop to the same size. At the thickness of 450 nm the grains already form an interconnected network and cross the percolation threshold. Further growth fully covers the surface with crystalline grains (1000 nm). Surface of grains indicates that they are actually aggregates of smaller grains (crystallites) – see Section 3.3.4. This is nicely visualized especially in the case of the 450 nm sample

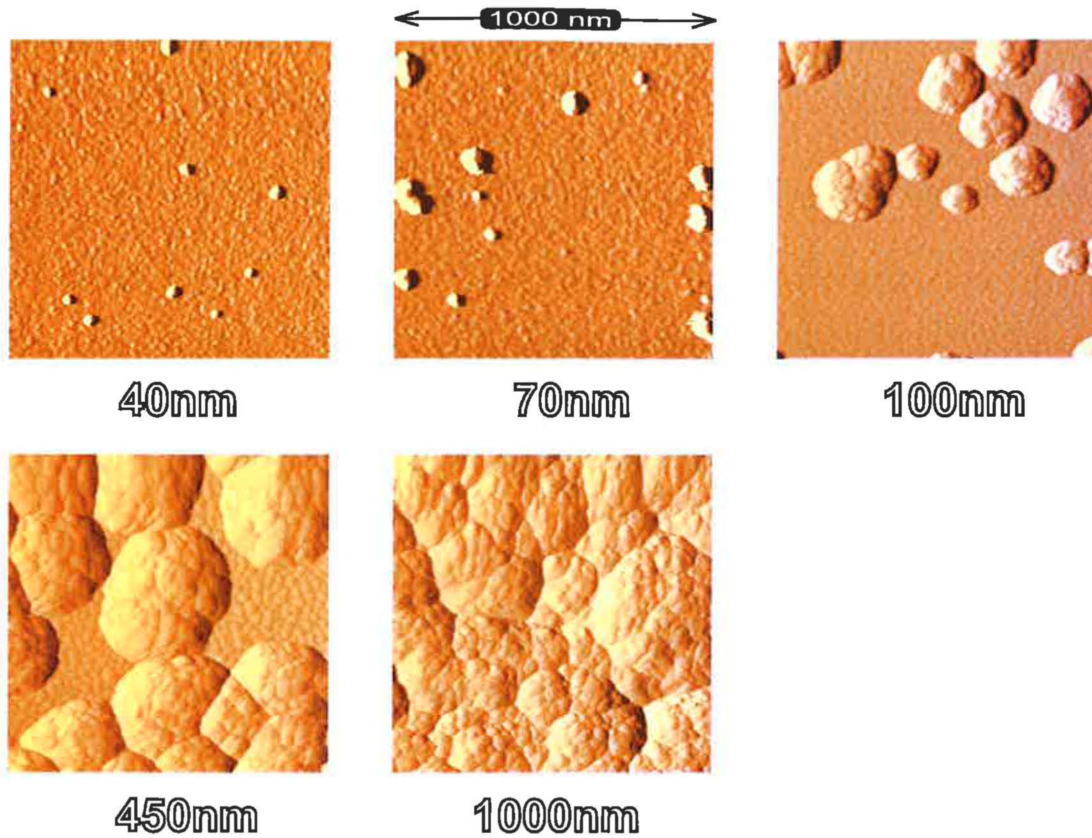

Figure 4.13: *AFM Surface topography of the samples of the thickness series at 75° C* ***on standard glass substrate****. Numbers indicate the thickness of each sample.*

in the map of local currents in Fig. 4.15, which provides higher resolution than the topography image.

A brief look at the pictures in Figs. 4.13 & 4.14 shows visible differences, for example in the case of 100 nm and 450 nm samples. These two images show just different spots of the same samples. In Fig. 4.13 the standard measurement of Si film grown directly on glass is presented, while Figs. 4.14 & 4.15 show how the same Si film has grown on NiCr coated glass. The typical grain diameter (see AGS in Table 4.7) is similar for each pair of pictures. The main difference is just in the number of grains, which reflects different nucleation density provided by each substrate material.

For μc–Si:H grown at standard conditions T_S=250° C the circular protrusions were identified as crystalline grains due to their higher conductivity [154]. The same is true for the thickness series prepared at very low temperatures T_S=75° C (Fig. 4.15) where the combined AFM measurements are presented. More conductive microcrystalline grains correspond to brighter ares in the maps of local currents (see Fig. 4.15(b)), while the darker areas represent the amorphous matrix with significantly lower conductivity.

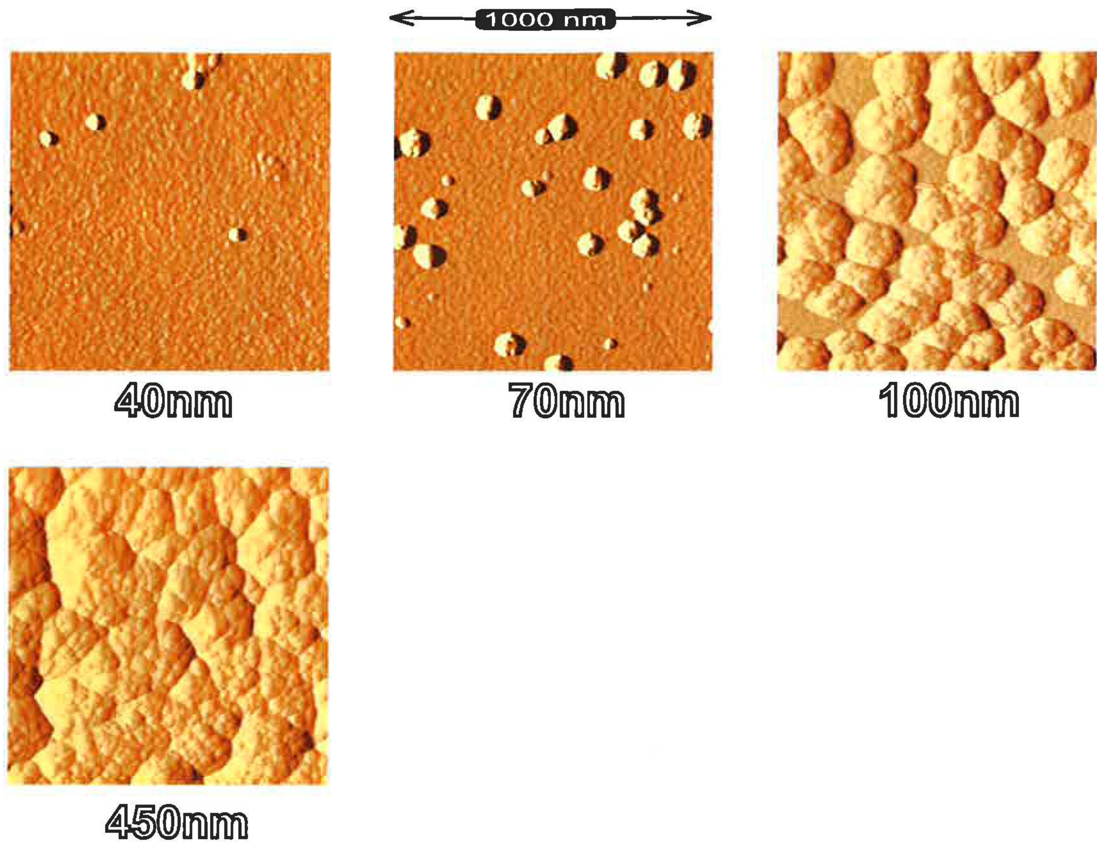

Figure 4.14: *AFM Surface topography of the samples of the thickness series at 75° C* ***on standard glass substrate covered with NiCr electrode****. Numbers indicate the thickness of each sample.*

The lower average conductivity in the case of 70 nm sample is caused by not yet completed interconnection of microcrystalline grains. The combined measurement performed by the UHV AFM microscope were carried out by the cantilever with PtIt conductive coating (Table 2.2). This cantilever is probably the reason of slightly larger grains observed by combined AFM (Fig. 4.15) compared to ambient AFM topography measurements (Fig. 4.13) performed by a sharper Si cantilever without the PtIr coating.

In Fig. 4.16 the values of surface RMS roughness together with the values of the diffusion length L_{diff} are plotted. Full circles represent the roughness of the microcrystalline samples grown directly on the glass substrate (Fig. 4.13), while open circles show the roughness of the samples grown on the NiCr electrode (Fig. 4.14).

The peak in the plot surface roughness values as a function of thickness is attributed to the transition between amorphous and microcrystalline structure (Section 3.2.6 and [49, 168]. Here, **for the series of samples with variable film**

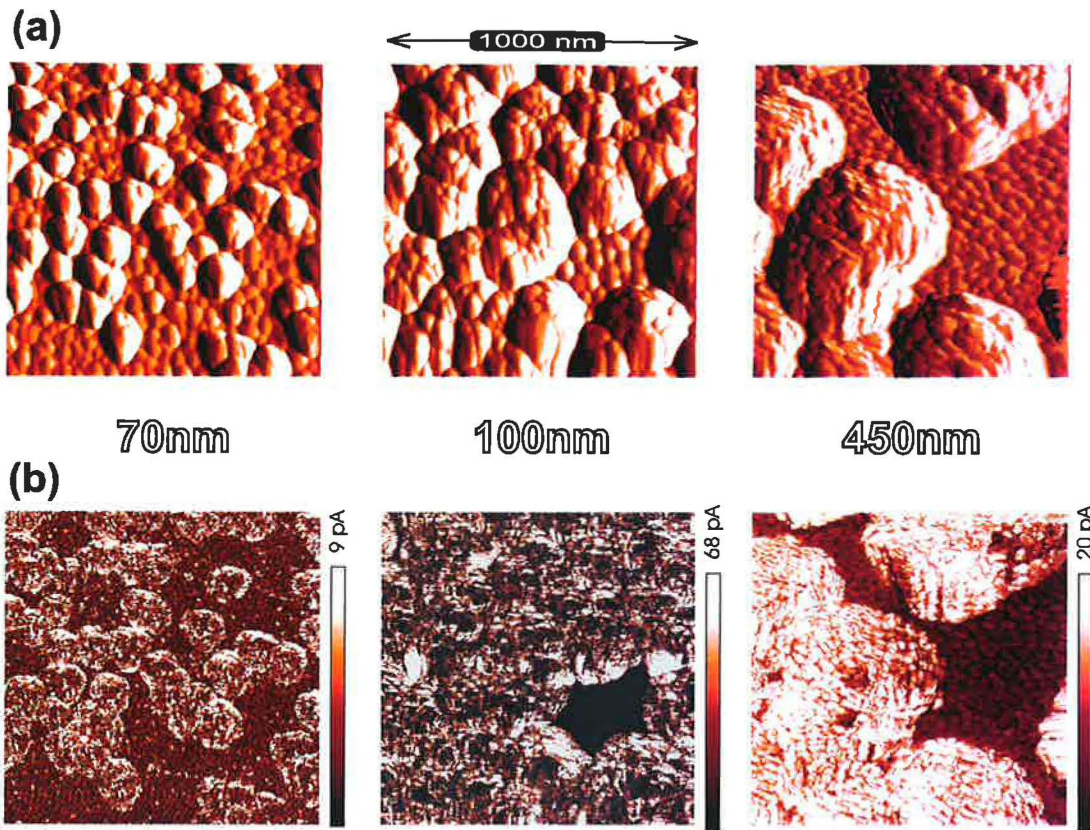

Figure 4.15: *Surface topography (a) and maps of local currents (b) of the samples of the thickness series at 75°C. The bias voltage (applied to the sample) was +5 V. Numbers below the images indicate the thickness of each sample.*

thickness, the transition from amorphous to microcrystalline structure occurs in the range of 250–600 nm. Fig. 4.16 also shows the shift of the roughness peak for the samples grown directly on glass to higher values of thickness. This can be generalized that the transition to fully μc–Si:H structure is obtained at a certain thickness if the nucleation density is fixed. Increase of the nucleation density can speed up the transition to μc–Si:H structure as seen in the AFM images of the sample Ge 08 (450 nm) in Figs. 4.13 & 4.14.

Note the striking similarity in the trend of the values of roughness and L_{diff} in Fig. 4.16. This behaviour can be explained as the competition of two contrary processes. The first process represents the growth of the microcrystalline grains. This brings the increase in the conductivity and thus higher values of the diffusion length. The combined structure of amorphous and microcrystalline silicon (as seen in the Fig.4.13 - 450 nm sample) is the case of the maximum roughness. When the grains "get in touch" and start to compete and coalesce, the roughness slightly decreases (1000 nm sample). The contact of microcrystalline grains may invoke the formation

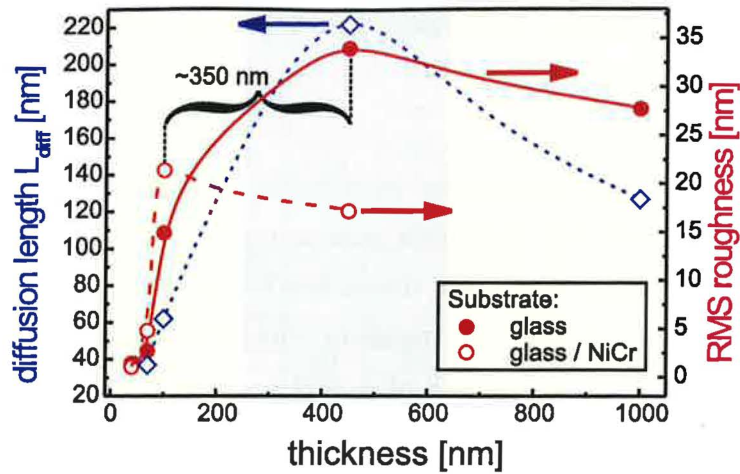

Figure 4.16: *Surface RMS roughness together with ambipolar diffusion length (L_{diff}) of microcrystalline samples of the thickness series at 75° C on standard glass substrate (full circles) compared with roughness of the same samples grown on metal NiCr electrode (open circles).*

of defective grain boundaries disturbing the transport (Section 3.3.5). Their presence may be responsible for the decrease of L_{diff} at 1000 nm in Fig. 4.16.

Finally, the values of L_{diff} and AGS give a perfect agreement with the rule in Eq. 3.1: L_{diff}/AGS $\sim$ 0.3–0.5 again reflecting the fact that the transport in mixed phase and μc–Si:H thin films is determined by grains and their boundaries.

Table 4.7: *Summarizing table of the properties of the thickness series prepared at 75° C (surface characteristics were evaluated for the films deposited directly on glass, as in all other series).*

Sample	X_C [%]	RMS [nm]	AGS [nm]	L_{diff} [nm]	σ_d $[\Omega^{-1}cm^{-1}]$	σ_0 $[\Omega^{-1}cm^{-1}]$	E_a [eV]
Ge 01 (40 nm)	–	1.38	46	–	–	–	–
Ge 03 (70 nm)	–	2.69	105	37	–	–	–
Ge 06 (100 nm)	–	14.90	180	62	–	–	–
Ge 08 (450 nm)	–	34.01	334	222	–	–	–
Ge 10 (1000 nm)	–	27.70	400	127	–	–	–

4.6 Controlled transport in the dilution series at 80° C

Composition of the working gas mixture, i.e., dilution of silane (SiH_4) in hydrogen (H_2) is one of the key deposition parameters for PECVD because it has a direct impact on the structure of the thin silicon film [54, 49, 178]. The exact values of silane concentration c_{SiH_4} or of another measure – hydrogen dilution ratio r_H (Definitions 2.2 and 2.3) leading to the growth of a-Si:H or μc–Si:H structure cannot be simply guaranteed for any deposition chamber. The deposition process is so complex that the transfer of exact r_H values to another chamber is not straightforward. This complicates the up–scaling process or repeated depositions in another laboratory. However, by depositing one or more series of samples with variable dilution in a sufficiently broad range of r_H, the particular value of r_H representing the transition between amorphous and microcrystalline structure should be obtained.

Thanks to the collaboration with other laboratories using different deposition systems, we faced all the troubles mentioned in the previous paragraph. This work should be thus understood as an investigation of general trends of the thin silicon films instead of an exact recipe for the deposition of a desired Si film.

The sample of the dilution series in this section were prepared in the Technical Research Institute of Toppan Printing Co. in Japan in the group of Dr. Manabu Ito. [1] The original sample names indicate the date of the deposition in the format YYMMDD-#i, where the # sign stands for the sequential number of the deposition in the particular day and "i" denotes the fact that an intrinsic layer was prepared. For a simpler handling of the samples in our laboratory, we added second, "more illustrative" names like MDS "r_H" based on the abbreviation of "Manabu – Dilution Series" and substituting "r_H" by the actual value of hydrogen dilution ratio for each sample as shown in the leftmost column of the Table 4.8.

This dilution series was prepared by changing the hydrogen dilution ratio r_H from 26 to 168 at a fixed substrate temperature of 80 °C. The excitation frequency was also f_{exc}=54 MHz (as in the case of the thickness series at 75° C in the previous section 4.5) and deposition duration was adjusted in order to achieve film thickness around 1 μm. This value was selected intentionally to provide structure with more pronounced typical features, sufficient signals for the electrical measurements and mainly a typical

[1] It is interesting to note that Manabu Ito obtained the experience of low T_S depositions during his stay at IPE, where the previous thickness series (Section 4.5) was prepared.

Table 4.8: *Overview of the main deposition parameters of the samples of the dilution series prepared at 80 °.*

Sample (abbrev.)	d [nm]	dil. r_H	T_S [°C]	f_{exc} [MHz]	P_{eff} [W]	p_{tot} [Pa]	$[H_2]$ [sccm]	$[SiH_4]$ [sccm]	r_d [nm/s]
010425-1i (MDS 34)	1340	34						1.5	0.25
010510-2i (MDS 43)	930	43						1.2	0.19
010511-4i (MDS 46)	1000	46						1.1	0.19
010509-4i (MDS 51)	880	51	80	54	10	20	50	1.0	0.18
010426-1i (MDS 64)	1530	64						0.8	0.17
010425-2i (MDS 101)	1010	101						0.5	0.09
010426-2i (MDS 168)	870	168						0.3	0.06

thickness of the i–layer in the solar cells. List of the deposition parameters is given in Table 4.8. The plasma power density for this series was 0.35 W/cm^2.

In contrast to the thickness series in Section 4.5 we succeeded in the measurements by most of available techniques. The results obtained in our laboratory for the samples of this dilution series were published in the joint papers [164, 194, 44, 110, 45].

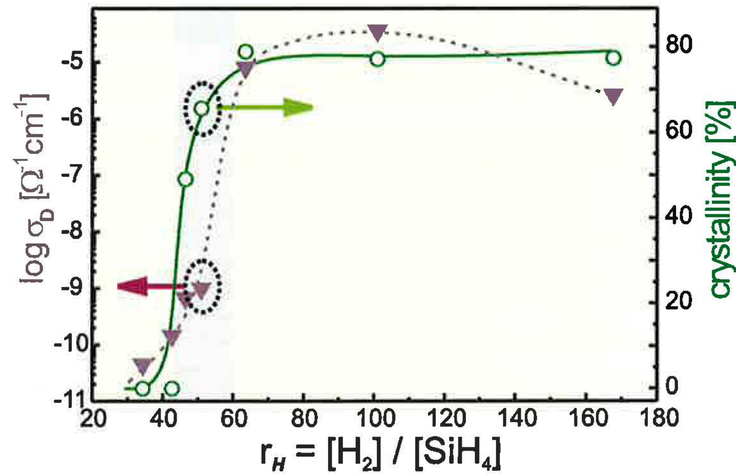

Figure 4.17: *Dark conductivity (σ_d) together with crystallinity (X_c) as a function of the silane dilution ratio r_H ranging from 34 to 168.*

The observations of the dilution series of samples deposited at T_S=225° C [52] indicate a clear transition to the crystalline structure for c_{SiH_4} above 5%, which is equal to $r_H \leq 19$. However, for the lower substrate temperatures T_S=75° C [48] and otherwise quite similar deposition conditions, the transition is shifted and occurs for $r_H \sim 50$ ($c_{SiH_4} \sim 2\%$). The same has happened for our dilution series (Fig. 4.17). Up to the value of r_H=43 the crystallinity (X_C) remains zero, indicating pure amorphous

structure. Between r_H=43 and 64, the crystallinity increases and above r_H=64, it is saturated (X_C ~80%) – a clear indication of fully μc structure. The same trend is shown in the plot of dark conductivity σ_d with just a small shift of the values to the right. The explanation is simple: while Raman measurement can detect isolated grains on the surface (X_C ≥0%), the overall conductivity might be still dominated by the amorphous phase. This exactly is the case of the mixed phase samples with r_H=46 and 51.

Estimations of the crystalline structure from Raman measurements is further confirmed by the results of X-ray diffraction (Section 2.3.6). All the samples up to r_H=51 exhibit fully amorphous response (Fig. 4.18). This means, there are no microcrystalline grains or too few grains to gain some XRD signal. As reported in [195], XRD method seems to be less sensitive to small amounts of crystalline phase in the thin film compared to Raman spectroscopy. Samples with r_H ≥64 indicate some degree of crystallinity with slightly preferential peak of the (111) crystallographic plane and much weaker response for (220) and (311) planes. Regrettably, this is not the ideal structure for high efficiency solar cells. It was reported that (220) preferential orientation provides better electronic properties [139]. The XRD patterns of the samples with r_H=101 and 168 show less noisy plots as a consequence of prolonged accumulation time. However, positions of peaks and their ratios are fully comparable.

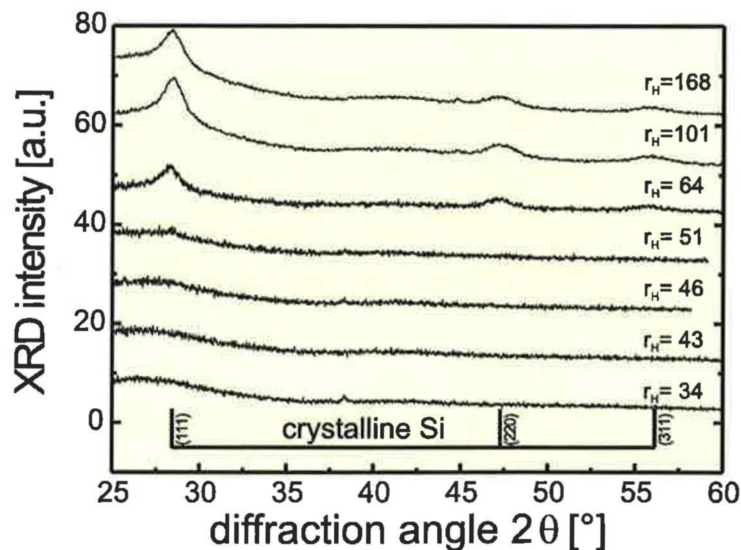

Figure 4.18: *Overview of the XRD patterns of all the samples of the dilution series.*

Plots of the absorption coefficient α measured by CPM are shown in Fig. 4.19. Taking into account the knowledge of typical shape of CPM spectrum [122], we can say that the spectra in this figure represent three distinct structures of thin Si films:

- amorphous – samples with r_H=34 and 43
- mixed phase – samples with r_H=46 and 51
- microcrystalline – samples with $r_H \geq$64

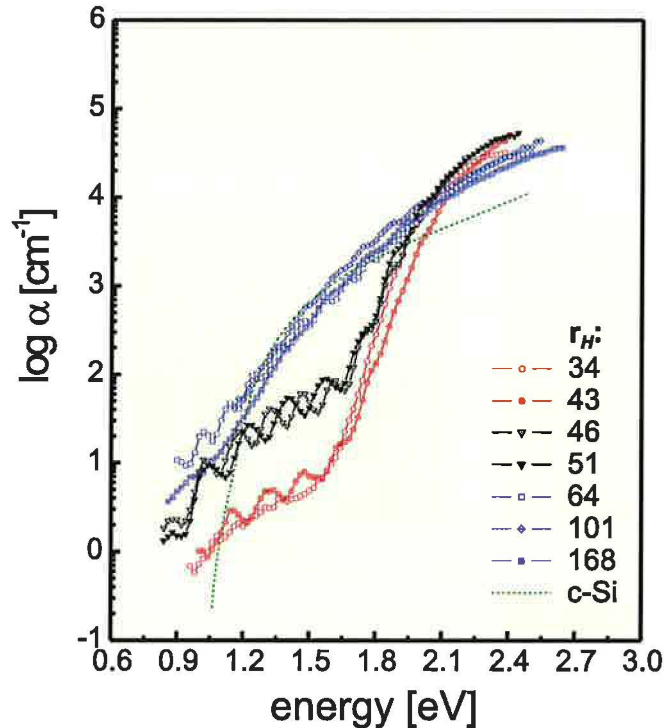

Figure 4.19: *CPM spectra of the samples of the dilution series.*

It is interesting to note that the highest values of α outside of the gap (above 2.0 eV) belong to the mixed phase samples. Based on data from Figs. 4.17 – 4.19 it is obvious that **for the series of samples with variable r_H, the transition from a–Si:H to μc–Si:H structure occurs for r_H between 45–60.**

Final information about the structure of samples comes from the topography measurements by AFM shown in Fig. 4.20. The structure undergoes a transition from rather smooth amorphous surface (r_H=34), through amorphous structure with only a few isolated grains (r_H=43–51) to rough μc–Si:H surface composed of grains (aggregates) with a typical cauliflower structure (r_H=64).

At higher values of r_H, the nucleation density increases and much smaller grains are formed (r_H=101 and 168). Note the striking similarity of the surface structure at low and high r_H (34 and 168 in Fig. 4.20.) although the first sample is completely amorphous and the last one is fully microcrystalline. This demonstrates that judging the sample structure only on the basis of AFM topography could be very misleading.

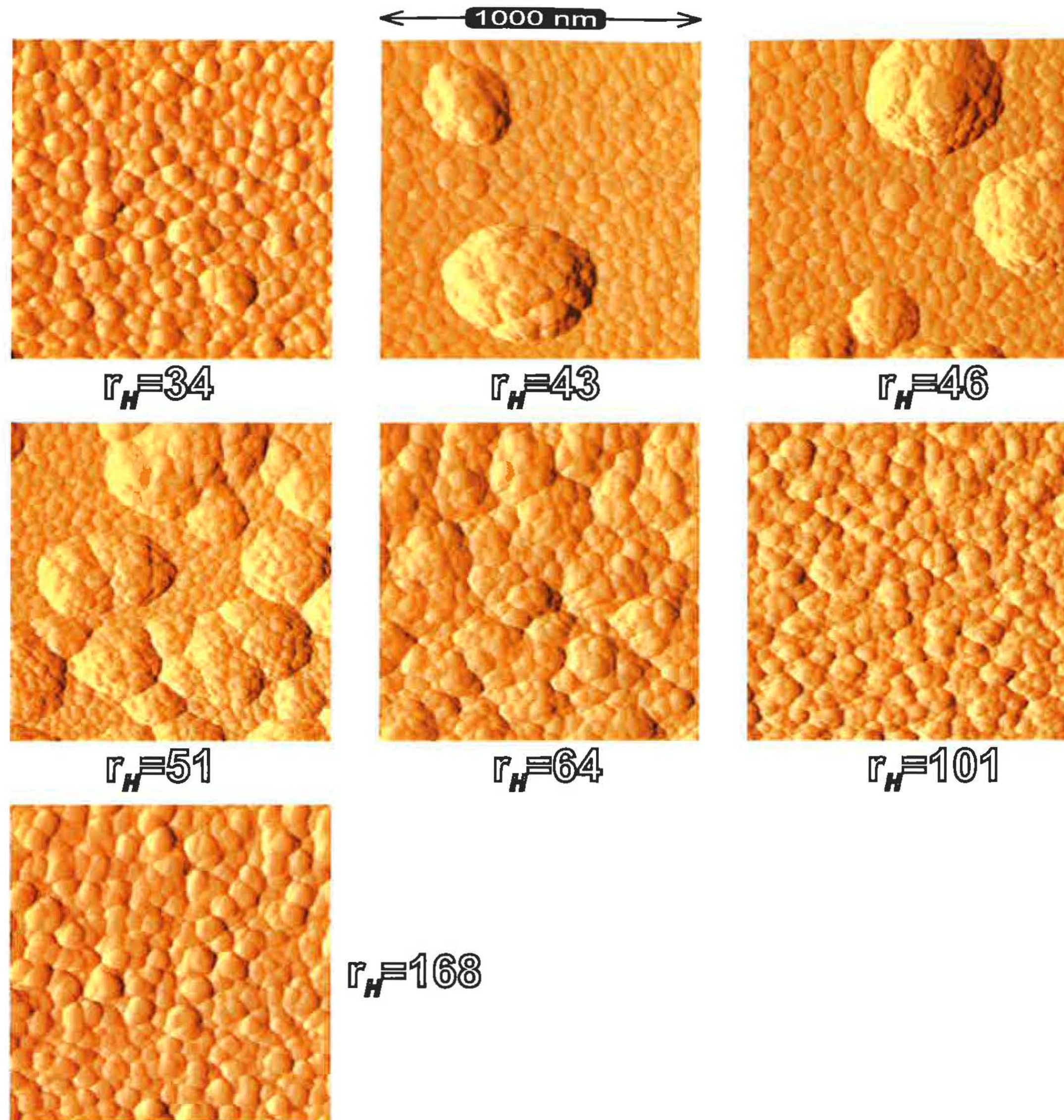

Figure 4.20: *AFM topography images of the samples of the dilution series.*

The results comparing structure (surface RMS roughness) and transport properties (L_{diff}) of the samples of this series are shown in Fig. 4.21, [164]. A sharp peak in the values of L_{diff} and of RMS roughness can be found at r_H=51. This coincidence of maxima in both plots is worth further attention. It seems to be a general behaviour of the a–Si:H /μc–Si:H transition and was observed by other laboratories, too.

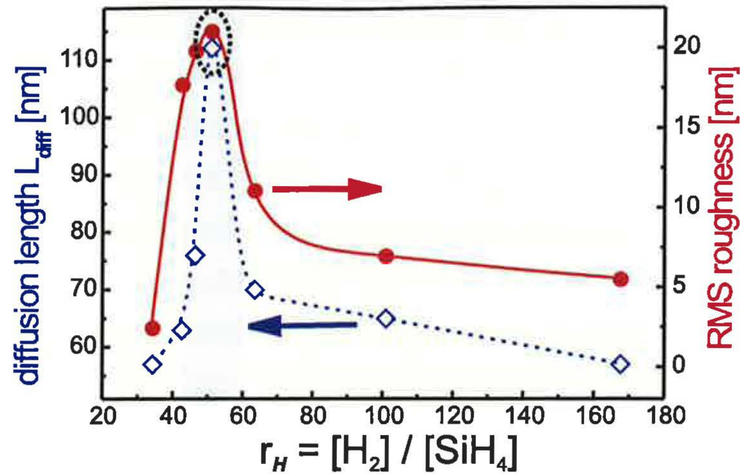

Figure 4.21: *Surface RMS roughness together with ambipolar diffusion length L_{diff} of the samples of the dilution series.*

Less pronounced peak in SSPG L_{diff} values was observed, for example, by the Neuchâtel group [67]. Another PECVD series presented in [67] exhibits the peak in RMS roughness as well as the results from Collins et al. [168]. Clear illustration of a–Si:H/μc–Si:H transition provides a special series of samples by Li et al. [195] exploiting the inhomogeneous deposition conditions within one deposition chamber.

Similar peak in L_{diff} values has been observed also for the dilution series of samples prepared by HWCVD (Section 2.2) in different laboratories: Ecole Polytechnique group [90, 92] and Utrecht University group [196]. The maxima of RMS roughness and L_{diff} coincide again.

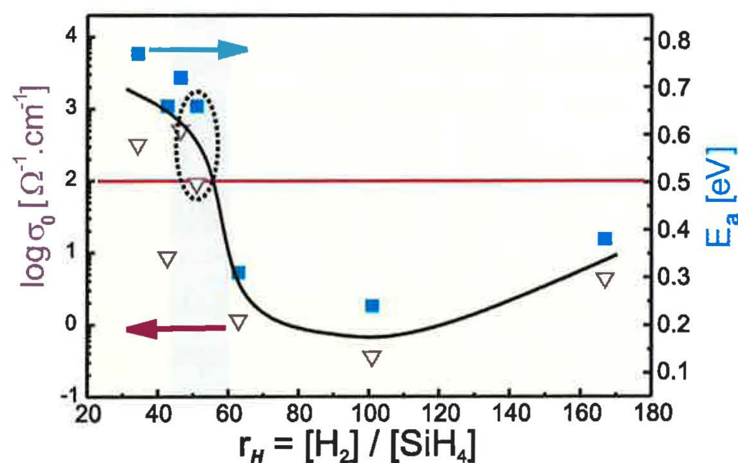

Figure 4.22: *Activation energy (E_a) together with conductivity prefactor (σ_0) as a function of the silane dilution ratio r_H ranging from 34 to 168.*

Taking into account all the presented data for the samples of the dilution series, illustrated by the AFM topography in Fig. 4.20, it is obvious that at r_H=51 the percolation threshold is crossed. Both the diffusion length in Fig. 4.21 and the activation energy E_a and conductivity prefactor σ_0 in Fig. 4.22, [45] exhibit a drop of their values, when $r_H \geq 51$. This clearly indicates the formation of large grains and their boundaries, which disturb the transport in the film.

As explained in Section 2.3.3, L_{diff} is a better measure of expected solar cell performance than the conductivity values (σ_d or σ_{ph}). Taking into account also the values of E_a and σ_0 and our guiding rule, it seems that **the sample prepared at r_H=51 would be the best μc–Si:H material** for the intrinsic layer of a solar cell prepared at T_S=80° C.

Table 4.9: *Summarizing table of the properties measured on the samples of the dilution series prepared at 80 °C.*

Sample	X_C [%]	RMS [nm]	AGS [nm]	XRD [nm]	L_{diff} [nm]	σ_d [$\Omega^{-1}cm^{-1}$]	σ_0 [$\Omega^{-1}cm^{-1}$]	E_a [eV]
MDS 34	0	2.4	71	–	57	4.5×10^{-11}	3.2×10^{2}	0.77
MDS 43	0	17.7	439	–	63	1.4×10^{-10}	8.7×10^{0}	0.66
MDS 46	49.1	19.8	419	–	76	6.8×10^{-10}	5.1×10^{2}	0.72
MDS 51	65.6	21.0	271	–	**112**	1.0×10^{-9}	9.2×10^{1}	0.66
MDS 64	78.9	11.1	244	14.2±1.6	70	8.0×10^{-6}	1.2×10^{0}	0.31
MDS 101	77.1	6.9	111	13.5±1.5	65	3.6×10^{-5}	3.6×10^{-1}	0.24
MDS 168	77.4	5.5	125	15±12	57	2.7×10^{-6}	4.4×10^{0}	0.38

We evaluated the size of grains both from AFM topographies (Fig. 4.20) and from XRD patterns (Fig. 4.18), see Table 4.9. The procedures are described in Sections 2.4.3 and 2.3.6 for average grain size (AGS) and grains from XRD, respectively. AGS's are in the range of 100–450 nm, while the XRD grains are ~15 nm, i.e., in good agreement with [52]. These values correspond to our previous observation of small and large grains by combined AFM (Fig. 3.24). We thus conclude that AGS refers to the size of large grains (aggregates), while XRD provides the information about small grains (crystallites), which form these aggregates. Large grains are then easily visible by AFM and their size is inversely dependent on the nucleation density. Taking into account the error bars for XRD grain size evaluation (Table 4.9), it seems that the size of crystallites remains almost constant, independent of the dilution r_H.

4.7 Exploring the properties of the VHF temperature series

The motivation for the study of the material properties of thin silicon films prepared at rather low deposition temperatures has been mentioned already in the Chapter 1. If the deposition temperature is below 100° C, much wider range of substrates materials can be used, i.e., glass can be replaced by cheap plastic substrates bringing also new mechanical properties (flexibility) to the solar cell modules.

Table 4.10: *Overview of the main deposition parameters of the samples of the VHF temperature series*

Sample	d [nm]	dil. r_H	T_S [°C]	f_{exc} [MHz]	P_{eff} [W]	p_{tot} [Pa]	$[H_2]$ [sccm]	$[SiH_4]$ [sccm]
011130-1i (MTS 35)	520		35					
011130-2i (MTS 50)	300		50					
011221-1i (MTS 60)	450		60					
011221-2i (MTS 65)	380		65					
011221-3i (MTS 70)	380		70					
011225-1i (MTS 75)	360		75					
020109-1i (MTS 80)	340	133	80	54	20	50	80	0.6
011220-4i (MTS 85)	290		85					
011220-3i (MTS 90)	290		90					
011219-1i (MTS 100)	260		100					
011219-2i (MTS 110)	300		110					
011126-4i (MTS 120)	350		120					
011126-1i (MTS 200)	400		200					

Table 4.11: *Additional deposition parameters of the samples of the VHF temperature series*

Average deposition rate r_d	~0.06 nm/s
Plasma power density	~0.71 W/cm^2

As in the case of the dilution series (Section 4.6), the samples were also prepared in the Technical Research Institute of Toppan Printing Co. in Japan in the group of Dr. Manabu Ito. The measurements of structural, optical and electronic properties were performed in our group. This series with variable substrate temperature T_S was prepared to test the lowest T_S for sufficient crystallinity X_C and observe the

change of structural and optoelectronic properties, when T_S decreases. Since it was expected that the lower temperatures will favour the growth of amorphous structure, we intentionally shifted the dilution r_H=133 to the fully microcrystalline regime. The substrate temperature T_S ranged from 35 °C to 200 °C, the excitation frequency was again 54 MHz (as in the case of previous series – Sections 4.5 and 4.6). By adjusting the deposition time, the thickness of layers was maintained around 0.35 μm. Main deposition parameters of the samples are summarized in the Table 4.10.

Samples are denoted by the abbreviation MTS standing for: Manabu – Temperature Series and the value of the key variable parameter (substrate temperature). For example, MTS 120 denotes the sample of the temperature series prepared at T_S=120°C. Since this work is dealing with two different temperature series, we denominated this one VHF temperature series due to f_{exc}=54MHz. The results obtained in our laboratory on the VHF temperature series from Toppan Printing Co. were published in the joint papers [194, 44, 197, 109, 110, 45, 193].

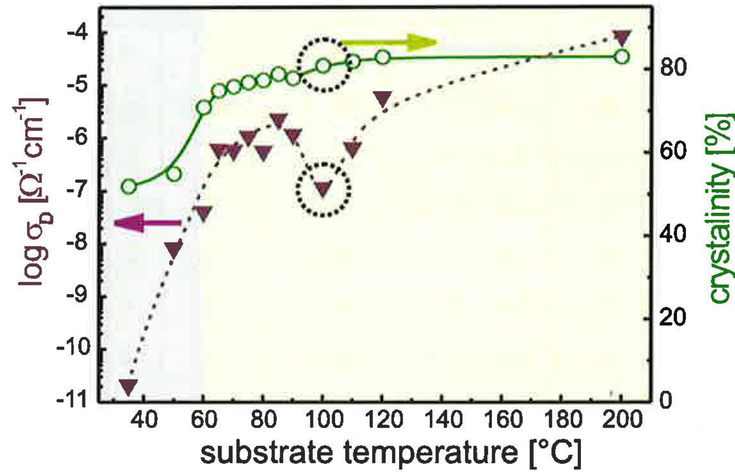

Figure 4.23: *Crystalline volume ratio (X_c) together with values of dark conductivity (σ_D) of the samples of the VHF temperature series.*

Starting with the crystallinity (X_C) and dark conductivity (σ_D) in Fig. 4.23, it is not surprising to see the sample with the highest T_S=200° C having X_C=83% and σ_D in the $10^{-5}\Omega^{-1}cm^{-1}$ range, which is typical for fully microcrystalline films. With decreasing temperature the X_C slowly decreases to 71% for T_S=60° C and then slightly drops to 55% and 52% for T_S=50° C and 35° C, respectively. The values of σ_D follow the same trend with two exceptions. Firstly, there is a local minimum of σ_D for T_S=100° C and secondly, for T_S ≤60° C, the dark conductivity drops in the 10^{-9}–$10^{-11}\Omega^{-1}cm^{-1}$ range, which is typical for fully a–Si:H films. This indicates that

the percolation threshold has been crossed at $X_C \approx 60\%$, confirming the universality of our model of the amorphous tissue coating the crystalline grains (Section 3.3.3, [169, 180]).

Another important fact is that for the samples prepared at T_S=60 – 90 ° C dark conductivity σ_D recovers to values between 10^{-6} and 10^{-7} $\Omega^{-1}cm^{-1}$ and crystallinity X_C remains around 70–80%. These findings show that a technological window for the preparation of μc–Si:H exists in this temperature range if sufficiently high dilution (r_H > 100) is used.

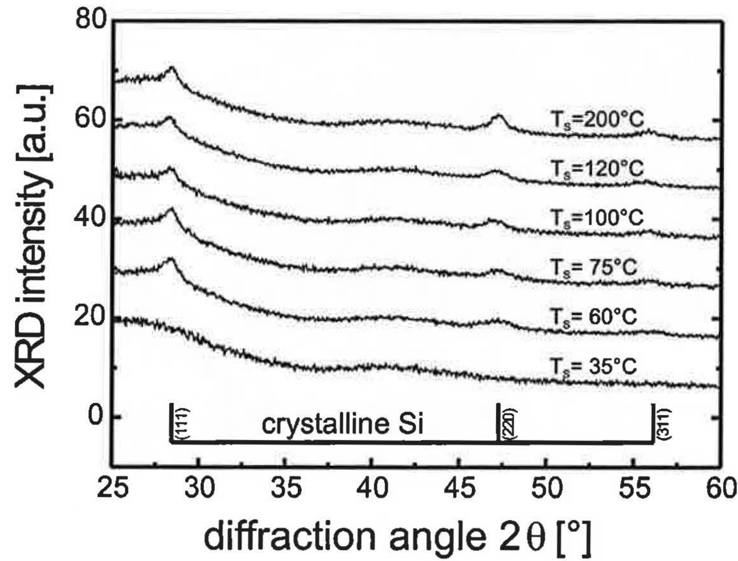

Figure 4.24: *Overview of the XRD patterns of selected samples from the VHF temperature series.*

The XRD measurements of the VHF temperature series (Fig. 4.24) are consistent with the Raman data (Fig. 4.23) and with the observations made on previous series. Samples with $T_S \geq$60°C, which have X_C >70%, exhibit some peaks in XRD patterns. **Two last samples with T_S=50°C and 35°C are really surprising! They also exhibit some crystallinity in their Raman spectra.** The values are a bit lower – $X_C \approx$ 55%, which is probably below the sensitivity threshold of the XRD measurement (as in the case of mixed–phase samples with r_H=46 and 51 in the dilution series in Figs. 4.17 and 4.18). These two samples have peculiar features. On one hand, there are data identifying them as a–Si:H samples:

- low dark conductivity σ_d
- no XRD response

However, there are also indications of the microcrystalline structure:

- Raman crystallinity X_C around 55%
- CPM spectrum of the absorption coefficient α

The plots of the α measured by CPM are shown in Fig. 4.25. Most of the samples of the VHF temperature series (T_S=60–120°C) have very similar values of α corresponding to typical μc–Si:H structure. The sample with T_S=200° C slightly sticks out in the range of 1.1 – 1.9 eV. The only different trends of α occur for the two samples with the lowest T_S, which are discussed in the previous paragraph. The comparison of CPM data in Fig. 4.25 with the previous dilution series (Fig. 4.19) gives the evidence of mixed–phase structure of these two samples.

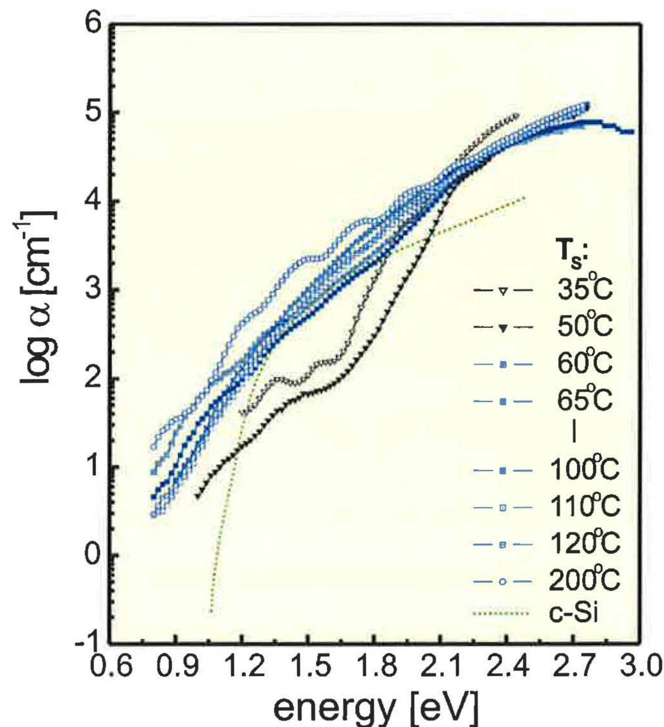

Figure 4.25: *CPM spectra of the samples of the VHF temperature series.*

Taking into account the data from Figs. 4.23 – 4.25 it seems that **for the series of samples with variable T_S, the transition from amorphous to microcrystalline structure occurs for $T_S \leq 60°$ C.** The fact that this series does not contain any sample with fully a–Si:H structure is caused by too high r_H value, which was selected to promote the μc–Si:H growth regime.

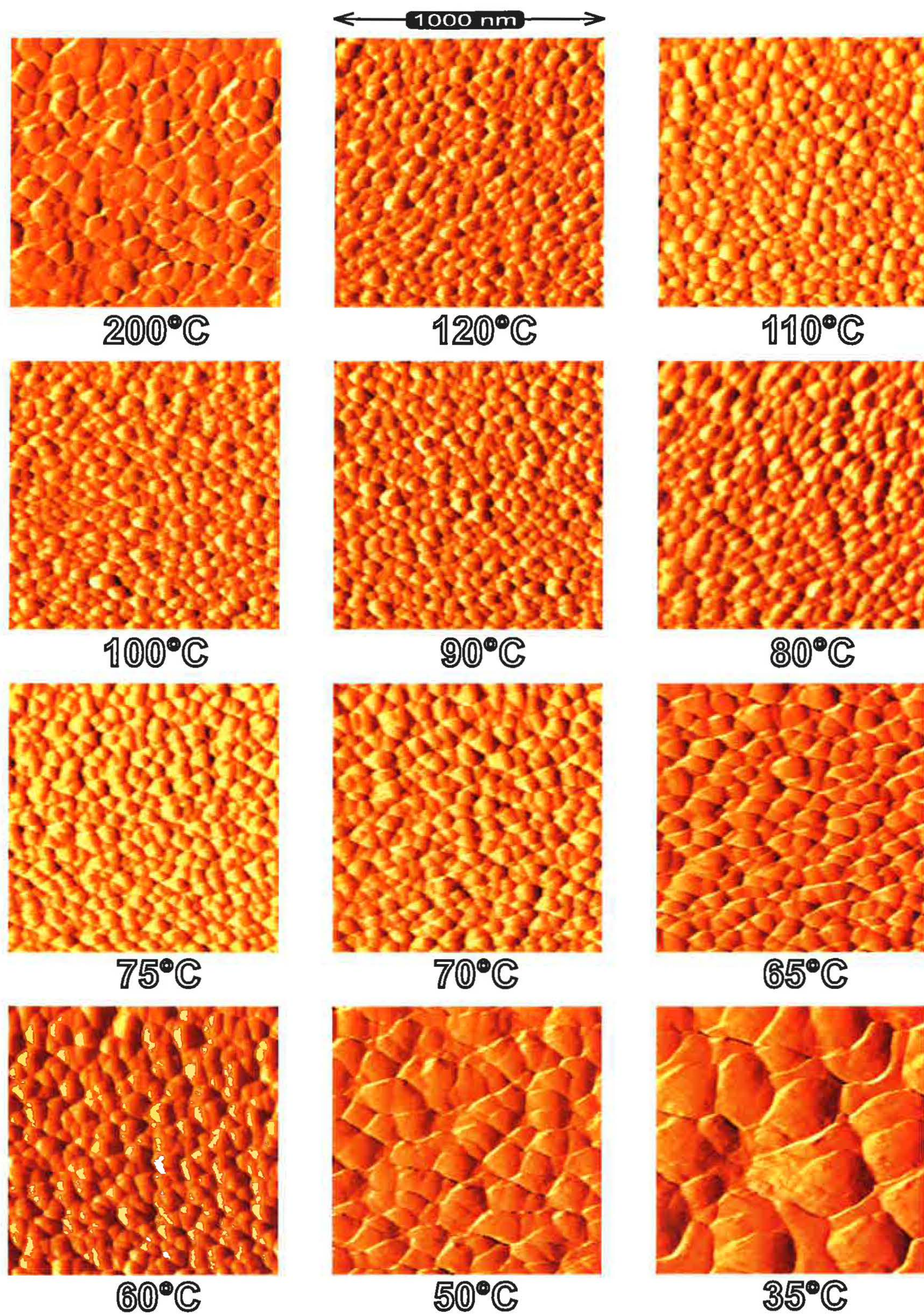

Figure 4.26: *Surface topography of the samples of the VHF temperature series by the ambient AFM microscope. Numbers below the images indicate the substrate temperature of each sample.*

Surface topography of the samples of VHF temperature series was measured both by standard ambient AFM (layer on glass – Fig. 4.26) and also by combined AFM (layer on Cr coated glass – Figs. 4.27 and 4.28). The ambient AFM topography (Fig. 4.26) does not show any dramatic change within the whole series, since all samples above 60° C are μc–Si:H and only a small fluctuation of grain size can be observed. This is also mirrored in the flat curve of surface RMS roughness (Fig. 4.29). For the temperature below 60° C, the apparent grain size on the surface is increasing (see values of AGS in Table 4.12) as well as the RMS roughness. The reason for the formation of large grains is the transition to the mixed–phase structure with decreasing T_S. As demonstrated in the case of the dilution series (Fig. 4.20), the nucleation density decreases when the conditions are shifted to the a–Si:H growth. The reason why no isolated μc–Si:H grains are observed on the surface of the samples of the VHF temperature series, is probably higher thickness of the deposited films. Supposing a similar growth mechanism as observed in the thickness series in Fig. 4.13, a similar surface structure might have been observed also for the samples with T_S=35° C if lower thickness, i.e., $\sim$200 nm, was used. Yet the increased value of RMS roughness in Fig. 4.29 for this sample is another proof of its mixed–phase structure.

In Fig. 4.27 results of simultaneous measurement of surface topography and maps of local currents (combined AFM) are displayed for the samples of the VHF temperature series. The maps of local currents indicate pronounced inhomogeneity when the T_S goes down to 35° C. This can be seen for $T_S \leq$ 100° C in the presence of less conductive grains or grains isolated by a surrounding amorphous tissue, which are visualized as darker areas. Further temperature decrease introduces more of these isolated grains and finally leads to the deterioration of the transport path, which is mirrored in significantly lower values of the macroscopic sample conductivity (Fig. 4.23) for $T_S \leq$60° C.

Topography images shown in Fig. 4.26 and 4.27 indicate grainy structure for all the samples of VHF temperature series. Comparison of values of AGS (average grain size evaluated from AFM) with the grain sizes obtained by XRD for selected samples in Table 4.12 indicates that AGS data represent the large grains (aggregates) and XRD data the small grains (crystallites) as in the case of dilution series in the previous section (Table 4.9).

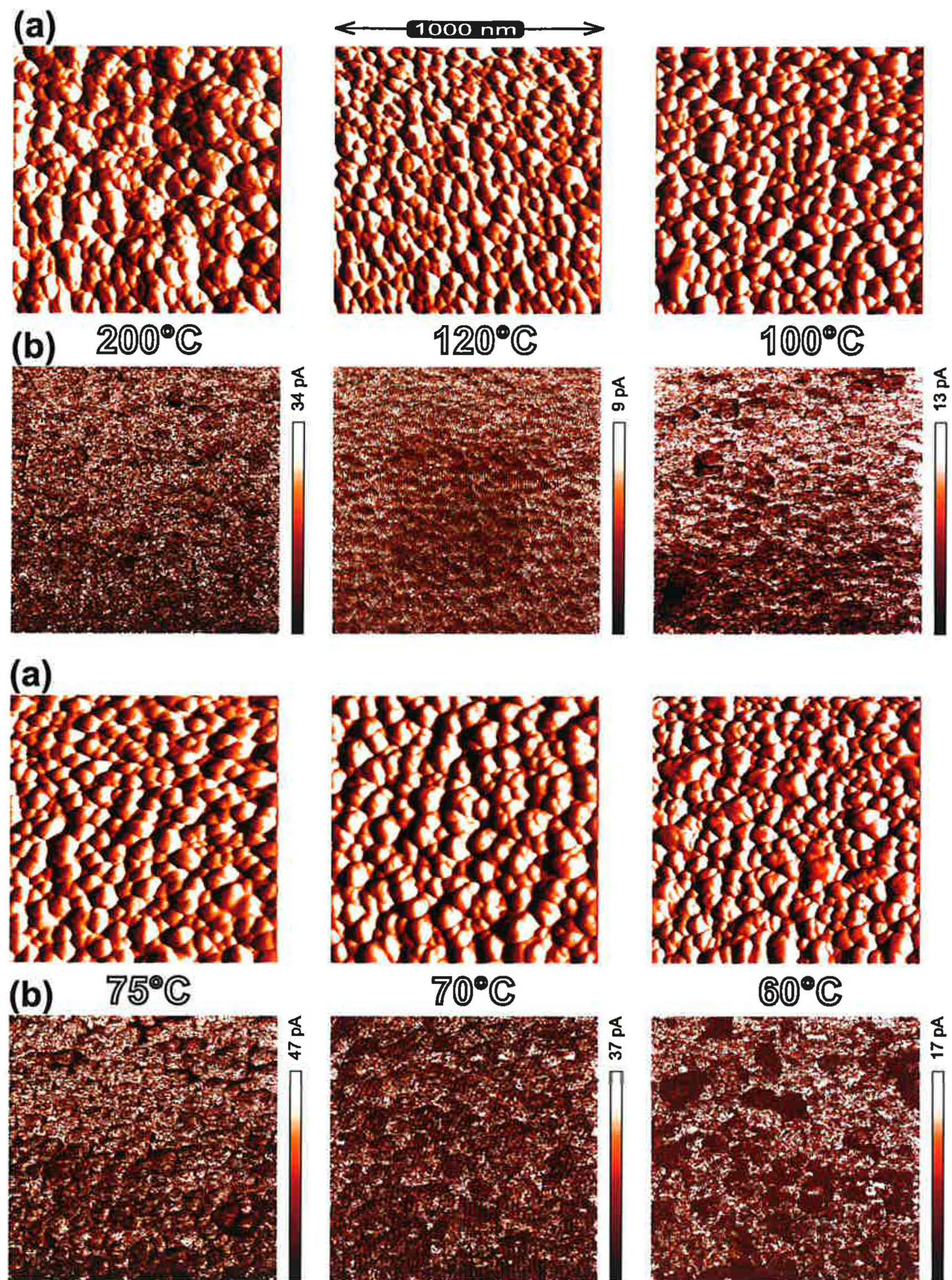

Figure 4.27: *Surface topography (a) and maps of local currents (b) of the selected samples of the VHF temperature series. The bias voltage (applied to the sample) was +7 V. Numbers below the images indicate the substrate temperature of each sample.*

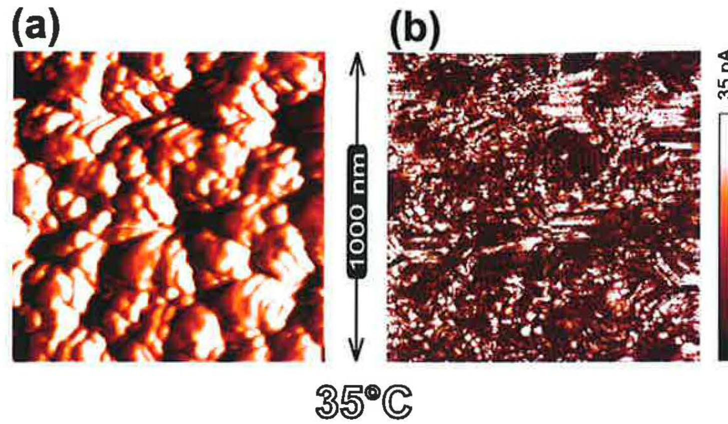

Figure 4.28: *Surface topography (a) and map of local currents (b) of the 35 ° sample of the VHF temperature series. The bias voltage (applied to the sample) was +7 V.*

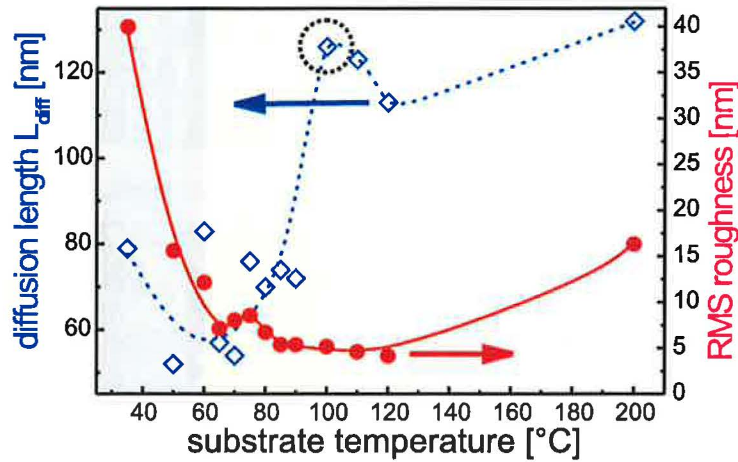

Figure 4.29: *Surface RMS roughness together with ambipolar diffusion length (L_{diff}) of the samples of the VHF temperature series.*

The evolution of diffusion length L_{diff} as a function of T_S is shown in Fig. 4.29. The typical coinciding peak of L_{diff} and RMS roughness for the mixed–phase samples is only partially indicated by the increase at 35° C. However, the other half is missing, i.e., decreasing tail for fully a–Si:H samples, which are not present in this series. Besides the a–Si:H/μc–Si:H transition effects, there are also dramatic changes of transport properties within the μc–Si:H samples ($T_S \geq$60° C). Fig. 4.29 shows similar values of L_{diff} for T_S=100–200° C, which then drop to half values for lower T_S. This change of transport properties is not accompanied by the change of structure (flat plot of RMS roughness for the given range of T_S). We attributed this behaviour to the change of nature of grain boundaries induced by the increased amount of hydrogen in

the deposited films (Fig. 4.30). Hydrogen is expected to be concentrated to the grain boundaries [198] and the change of grain/grain boundary ratio is probably the reason of the fluctuations of the H content. However, the averaged plot in Fig. 4.30 gives a clearly increasing trend for decreasing T_S.

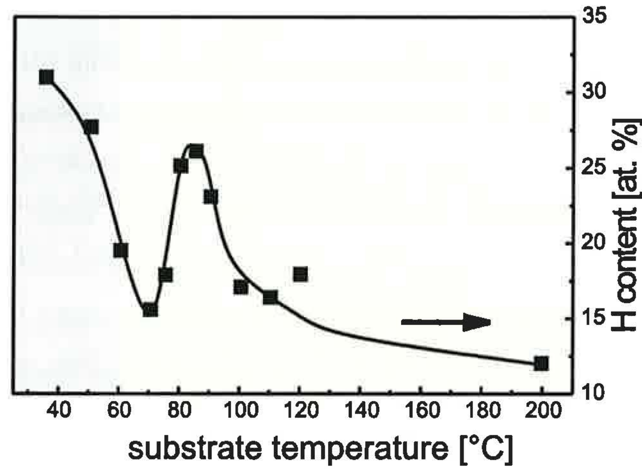

Figure 4.30: *Hydrogen content by ERDA within the VHF temperature series.*

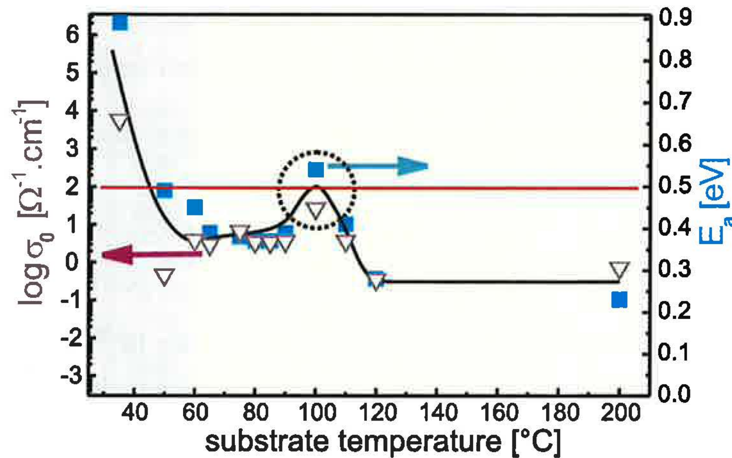

Figure 4.31: *Activation energy (E_a) together with conductivity prefactor (σ_0) of the samples of the VHF temperature series.*

The quality of grain boundaries in μc–Si:H films can be monitored by measuring the values of activation energy E_a and conductivity prefactor σ_0 (Fig. 4.31) as we proposed in the guiding rule (see Definition 3.2 on page 68) represented graphically by the horizontal line in Fig. 4.31. The formation of large grain boundaries, which deteriorate the transport in μc–Si:H films, is indicated by the drop of values of prefactor σ_0 below 100 Ω^{-1}.cm^{-1} and activation energy E_a below 0.5 eV. This is valid

for all the μc–Si:H samples of VHF temperature series with one exception – sample deposited at T_S=100°C, which is the only sample without the large grain boundaries.

Comparing the data in Figs. 4.29, 4.30 and 4.31, the behaviour of samples of this series becomes more understandable. The sharp drop of L_{diff} exactly matches the onset of the peak in hydrogen content. The local maximum of L_{diff} at T_S=100° C also corresponds to the local maximum of E_a and σ_0 for the only sample fulfilling the guiding rule. There are plateaus on both sides of this local maximum (Fig. 4.31) indicating two different transport mechanisms for T_S=60–90° C and 110–200° C. This is also reflected in quite distinct values of L_{diff} for these two groups of samples. Another comparison of L_{diff}, σ_d (Fig. 4.23) and photoconductivity σ_{ph} (with the same trend as σ_d [110]) in the range of 90–110° C shows opposite behaviour of L_{diff} and conductivities. This is probably caused by the fact that these quantities are controlled by different charge carriers: majority carriers determine σ_{ph}, σ_d, while minority carriers determine L_{diff}. These quantities are thus strongly and inversely dependent on the position of the Fermi level in the material.

Since L_{diff} is a better measure of expected solar cell performance than the σ_d or σ_{ph} values and taking account also the values of E_a and σ_0 in the context of our guiding rule, it seems that **the sample prepared at T_S=100° C would be the μc–Si:H material** for the intrinsic layer of a solar cell prepared at r_H=133.

Table 4.12: *Summary of the properties of the samples of the VHF temperature series.*

Sample	X_C [%]	RMS [nm]	AGS [nm]	XRD [nm]	L_{diff} [nm]	σ_d [$\Omega^{-1}cm^{-1}$]	σ_0 [$\Omega^{-1}cm^{-1}$]	E_a [eV]	H_{ERDA} [%]
MTS 35	52.0	40.0	287	–	79	2.1×10^{-11}	5.7×10^{3}	0.89	31.1
MTS 50	55.0	15.6	153	–	52	8.2×10^{-9}	4.7×10^{-1}	0.49	27.8
MTS 60	71.0	12.2	97	7.4±5.0	83	4.1×10^{-8}	3.9×10^{0}	0.45	19.5
MTS 65	75.0	7.2	100	–	57	6.1×10^{-7}	3.0×10^{0}	0.39	-
MTS 70	76.0	8.1	71	–	54	5.9×10^{-7}	–	–	15.6
MTS 75	77.0	8.6	77	10.1±6.3	76	1.1×10^{-6}	6.7×10^{0}	0.38	17.9
MTS 80	77.5	6.7	105	–	70	5.7×10^{-7}	3.5×10^{0}	0.37	25.2
MTS 85	79.0	5.4	83	–	74	2.3×10^{-6}	3.4×10^{0}	0.37	26.2
MTS 90	78.0	5.4	80	–	72	1.2×10^{-6}	3.7×10^{0}	0.39	23.2
MTS 100	81.0	5.2	84	8.7±2.7	**126**	1.2×10^{-7}	2.7×10^{1}	0.54	17.1
MTS 110	82.0	4.6	83	–	123	6.5×10^{-7}	3.8×10^{0}	0.41	16.4
MTS 120	83.0	4.2	77	5.3±1.3	113	6.0×10^{-6}	3.6×10^{-1}	0.28	18.0
MTS 200	83.0	16.3	105	21±10	132	8.3×10^{-5}	7.4×10^{-1}	0.23	12.0

4.8 Exploring the properties of the RF temperature series

The RF temperature series of thin Si films was prepared with the same motivation as in the case of VHF temperature series (Section 4.7). The aim was also to clarify some questions, which arose from the interpretation of results of the VHF temperature series. The questions were as follows:

- Can we prepare the whole range of structures (a–Si:H, mixed–phase, μc–Si:H) by changing the T_S?
- Are the indications of the mixed–phase structure as clear as in the case of variable thickness and dilution?
- What is the role of H at low T_S?
- What is the structure of samples prepared close to RT?

Table 4.13: *Overview of the main deposition parameters of the samples of the RF temperature series*

Sample (T_S)	d [nm]	dil. r_H	T_S [°C]	f_{exc} [MHz]	P_{eff} [W]	p_{tot} [Pa]	$[H_2]$ [sccm]	$[SiH_4]$ [sccm]
Stm 232 (250°)	900		250		8.5			
Stm 233 (220°)	900		220		8.5			
Stm 235 (190°)	850		190		8.5			
Stm 236 (160°)	900		160		8.5			
Stm 237 (130°)	900	32	130	13.56	8.2	70	50	1.6
Stm 238 (100°)	850		100		8.0			
Stm 246 (80°)	900		80		8.0			
Stm 241 (60°)	850		60		8.0			
Stm 242 (40°)	850		40		8.0			

To ensure the fact that both the a–Si:H and μc–Si:H structures would be obtained we shifted the value of dilution closer to the transition, i.e., r_H=32. The same value of r_H was used in the thickness series (Section 4.4.2), which was prepared in the same deposition chamber. Due to the transfer of results, we were sure that the samples at the highest T_S will have μc–Si:H structure if their thickness is more than 300 nm. The other deposition conditions were also adopted from the thickness series, i.e.,

Table 4.14: *Additional deposition parameters of the samples of the RF temperature series*

Average deposition rate r_d	~0.08 nm/s
Plasma power density	~0.21 W/cm^2
Substrate potential	U_{fl}
Cathode peak to peak voltage	~500 V
Cathode bias voltage	~-120 V

we took the values optimized for our PECVD chamber at the Department of Thin Films, Institute of Physics in Prague. Details of this chamber are indicated in the Fig. 2.1. The full list of the deposition parameters used for the RF temperature series of samples is given in the Table 4.13. The main differences – compared to the previous VHF temperature series – is the discharge frequency f_{exc}=13.56 MHz and higher thickness of samples 0.9 μm.

The samples of this series are denoted as "Stm #", where the # sign stands for the sequential number of the deposition. The results obtained in our laboratory on this RF temperature series of samples were published in the papers [199, 193].

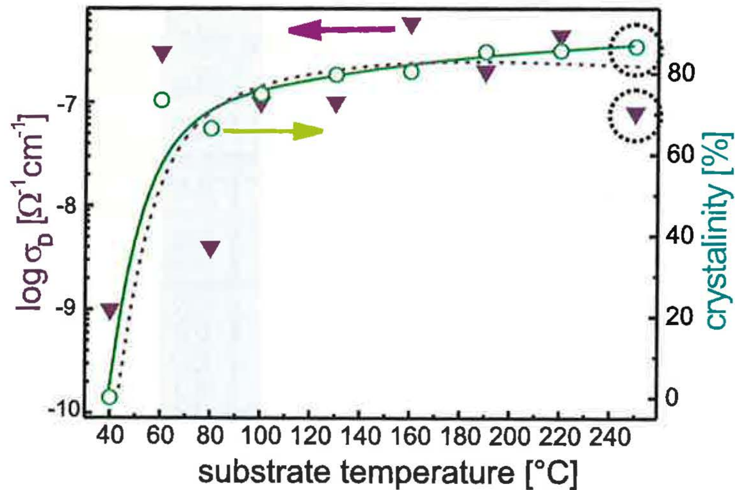

Figure 4.32: *Crystalline volume ratio (X_c) together with values of dark conductivity (σ_D) of the samples of the RF temperature series.*

By decreasing the T_S we crossed the whole range of structures: from fully μc–Si:H ($T_S \geq 100°$ C), through mixed–phase (T_S=80°C) and for the lowest T_S=40° C we obtained fully a–Si:H sample. This is seen in the values of crystallinity X_C and dark conductivity σ_d having "true amorphous" values for T_S=40° C (Fig. 4.32). For T_S above 100° C a slow increase of X_C and σ_d is observed. All the values are well above the percolation threshold, i.e., corresponding to fully μc–Si:H material. The fluctuations

of values for T_S=60 and 80° C probably resulted from slight variations of deposition conditions, to which the samples in the transition zone are very sensitive.

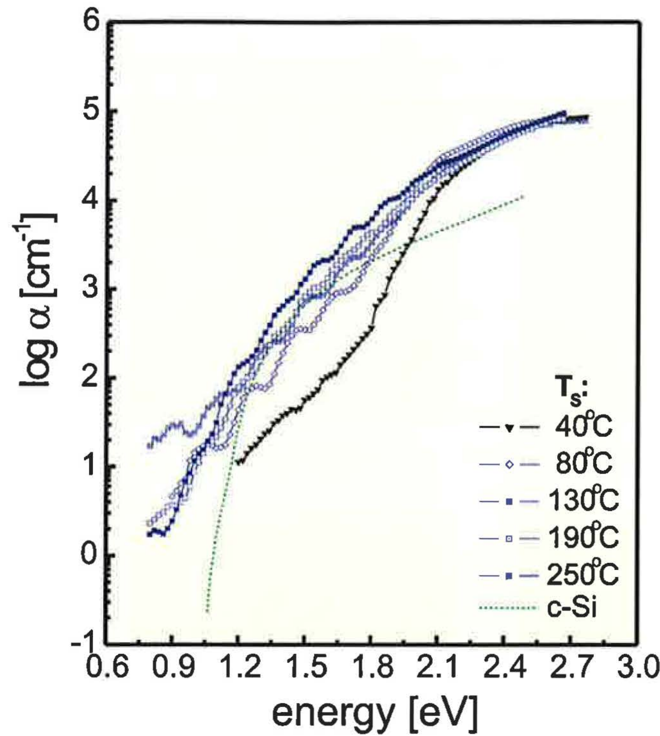

Figure 4.33: *CPM spectra of the samples of the RF temperature series.*

The plots of the α measured by CPM are shown in Fig. 4.33. All the samples with $T_S \geq 80°$ C exhibit plots of α corresponding to typical μc–Si:H structure, which is in good agreement with the X_C crystallinity data in Fig. 4.32. The only different trend of α occurs for the sample with T_S=40° C. The comparison with previous CPM plots indicates a mixed–phase structure, however, by taking into account the other data available for this sample, i.e., X_C=0% and AFM topography (Fig. 4.34) it is more likely that this sample is amorphous with a high level of defects shifting–up the values of α below 1.9 eV. This is in consistence with the poor transport characteristics (L_{diff} and σ_0) presented in Figs. 4.36 and 4.38, respectively.

The surface topography of the films measured by ambient AFM is shown in the Fig. 4.34. From the sample prepared at 250 °C down to the sample at 130 °C the surface structure shows no major change, remaining almost at the same value of the surface roughness (Fig. 4.36). These samples are dominantly microcrystalline as confirmed by crystallinity X_C plotted in Fig. 4.32.

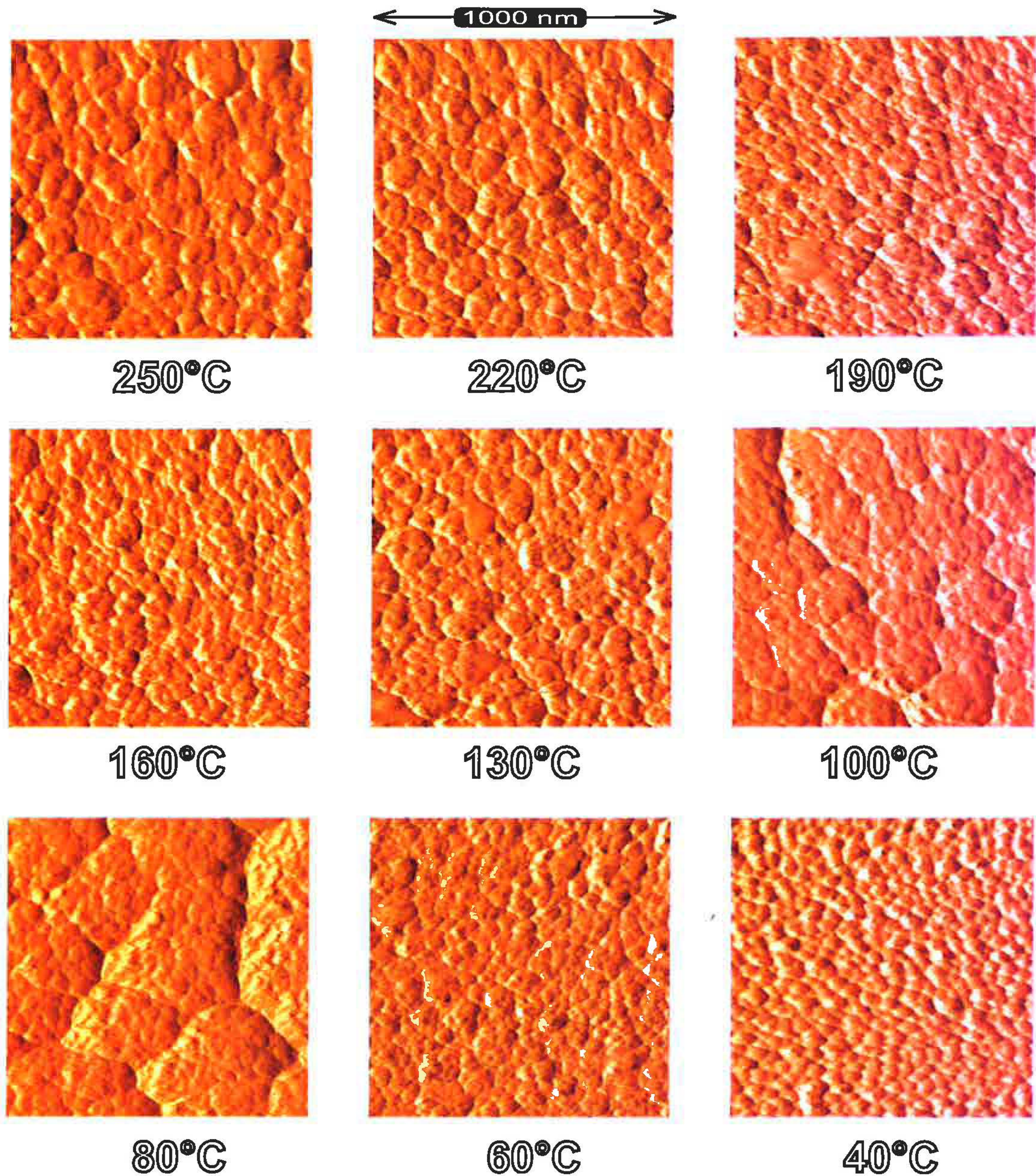

Figure 4.34: *Surface topography of the samples of the RF temperature series taken by the ambient AFM microscope. Numbers below the images indicate the substrate temperature of each sample.*

The samples at 100 °C and 80 °C represent the surface of mixed–phase structure typically pronounced by the peak in surface roughness (Fig. 4.36). Lower nucleation density lead to the increase of grain size, which brings corrugations seen in the AFM images (Fig. 4.34). The fact that these mixed–phase samples do not exhibit isolated μc–Si:H grains (nor did the samples of the VHF temperature series in Fig. 4.26) is probably due to higher thickness of the deposited films. However, the lower nucleation density for the mixed–phase samples is still pronounced by much higher surface roughness even at the thickness of ~900nm.

Contrary to the previous VHF temperature series we did not find the surprisingly large grains near the room temperature. This was due to the fact that further lowering of the deposition temperature T_S at the conditions selected for this RF temperatures series caused the formation of amorphous films as confirmed by the values of sample crystallinity X_C (Fig. 4.32).

Taking into account the data from Figs. 4.32 – 4.34 it seems that **for the RF temperature series the transition from amorphous to microcrystalline structure occurs for 60° C < T_S ≤100° C.**

For this RF temperature series we could exploit the fact that the samples were prepared in our deposition chamber directly connected to the same vacuum system as the UHV AFM/STM microscope. This made it feasible to use the combined AFM measurements of in–situ films, which are presented in Fig. 4.35.

Comparison of Figs. 4.34 and 4.35 reveals a clear difference in topography for the samples with $T_S \leq 100°$ C. This is the same case as we observed in the low temperature thickness series in Figs. 4.13 and 4.13 – the influence of the substrate material. It was mentioned in Section 4.2 that the combined AFM is measured above the bottom Cr electrode, while the air–AFM is measured on Si deposited directly on glass. The presence of metal electrode shifted the growth regime more to the μc–Si:H phase and this was the reason for the μc–Si:H structure at 100° C and mixed–phase structure at 80 and 40° C. This means that the samples at 60 and 40° C are not homogeneous all over the substrate – they have a–Si:H structure on glass and mixed–phase structure when the film is grown on Cr coated glass.

The maps of local currents indicate quite homogeneous distribution for the scanned areas for samples with $T_S \geq 100°$ C, which is typical for fully μc–Si:H films. For the last two samples with T_S=80 and 40° C the local current exhibits increased values at the grain boundaries, which we attribute to the measurement artefact caused by variable contact area on very rough surfaces (Section 2.4.5).

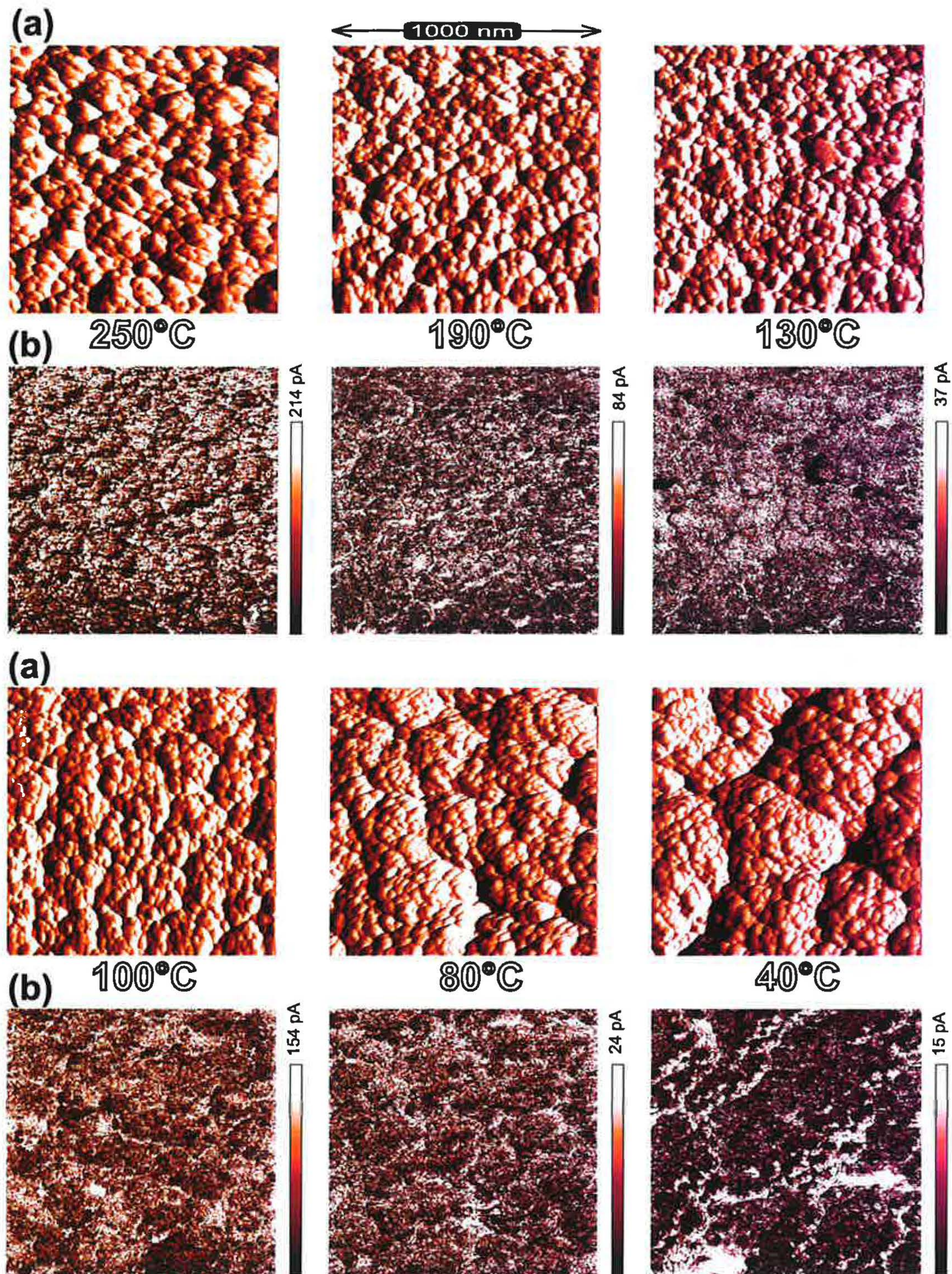

Figure 4.35: *Surface topography (a) and maps of local currents (b) of the selected samples of the RF temperature series. The bias voltage (applied to the sample) was +7 V. Numbers below the images indicate the substrate temperature of each sample.*

Due to the well defined surface conditions (UHV), we can also extract some quantitative information from the absolute values of local currents. Providing the same bias voltage of +7V, the sample at 250° C exhibits highest current values around 200 pA and sample at 100° C values around 150 pA. The other samples at 190 and 130° C would probably provide their highest local current values between these two values, however, due to the wear off of the metal coating, the actual values are a bit lower than expected. The last two samples at 80 and 40° C provide much lower values of local current – in the order of tens of pA. Taking into account their mixed–phase structure, there must be a significant a–Si:H incubation layer below the fully μc–Si:H surface preventing it from the direct electrical contact to the bottom electrode. Using this interpretation we come to a very good agreement with the macroscopic dark conductivities σ_d of the whole films shown in Fig. 4.32.

The RMS surface roughness (evaluated from images in Fig. 4.34) exhibits a peak for the mixed–phase sample at T_S=80° C. The transport properties represented by the diffusion length L_{diff} in Fig. 4.36 follow this trend with the coinciding peak as in the case of the dilution series in Fig. 4.21.

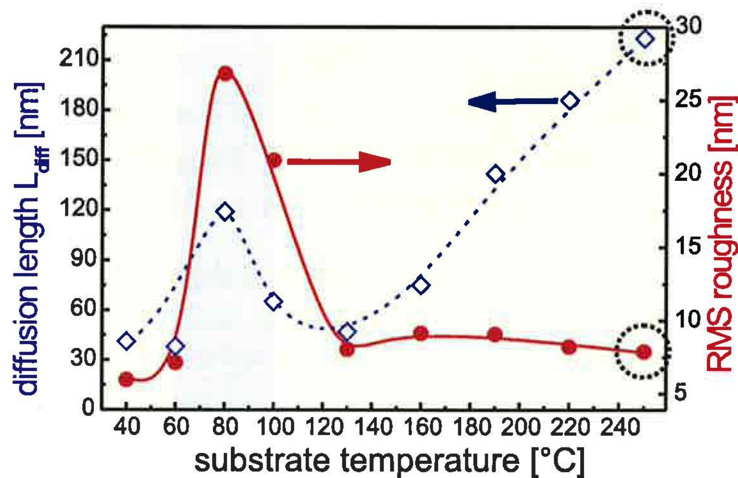

Figure 4.36: *Surface RMS roughness together with ambipolar diffusion length (L_{diff}) of the samples of the RF temperature series.*

However, these typical features of a–Si:H to μc–Si:H transition are combined with the effect of variable substrate temperature T_S, which is responsible for the trend of L_{diff} for $T_S \geq 130$° C. The L_{diff} values show a substantial increase (tripling the value in the given range), which does not correlate with the change of structure – see the flat plot of RMS roughness in Fig. 4.36 and values of average grain size (AGS) $\sim$ 100 nm in the Table 4.15 for $T_S \geq 130$° C. If the structure remains almost the same, but the

transport properties undergo a dramatic change, then something else in the film must be changing. It is the content of hydrogen in the film shown in Fig. 4.37. This figure shows the amounts of hydrogen in the film measured by two different techniques, which provide complementary information both about the amount and location of hydrogen in the studied material (Section 2.3.7). While the H–content by FT–IR remains almost constant within the whole range of substrate temperatures, results from ERDA indicate increasing total amount of hydrogen for lower T_S. This means that the amount of molecular (non–bound) hydrogen is increasing for decreasing T_S. Taking into account the X_C data showing a small, but systematical decrease for T_S=250 °C downto 100° C, means that the increase of H–content is closely related to the presence of amorphous structure.

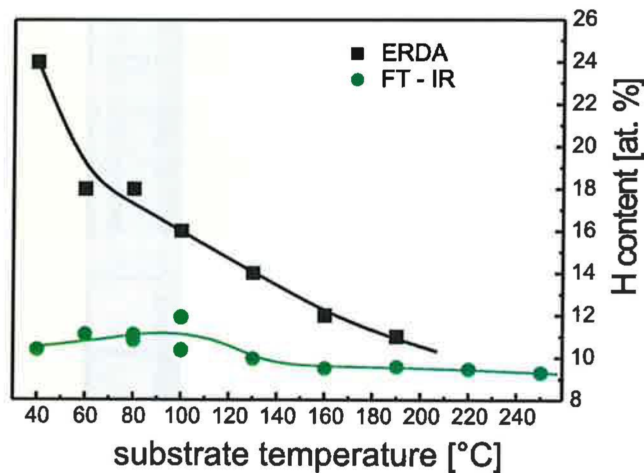

Figure 4.37: *Hydrogen content in the samples of the RF temperature series measured by ERDA and FTIR.*

In films with $X_C \geq 70\%$ (above the percolation threshold) the a–Si:H structure is expected to be at the grain boundaries. This is then the explanation for the decrease of L_{diff} for T_S=250° C downto 100° C: the increasing amount of hydrogen is incorporated in the disordered a–Si:H structure of the grain boundaries acting as potential barriers and disturbing the electronic transport.

The peak in total amount of hydrogen typically observed for the mixed–phase samples in [53, 90] is in this series probably superimposed by another effect, i.e., steadily increase of H–content caused by the decreasing substrate temperature T_S.

Fig. 4.38 shows the dependency of the activation energy E_a together with conductivity prefactor σ_0 as a function of the deposition temperature. Using our guiding rule for the μc–Si:H films (see Definition 3.2 on page 68) one can easily determine the

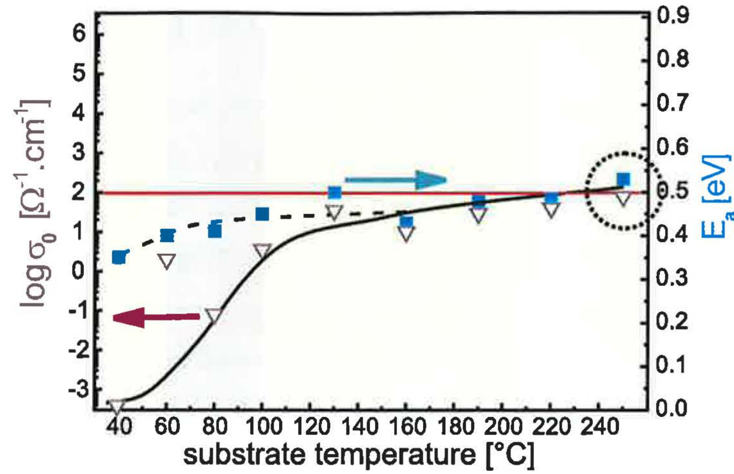

Figure 4.38: *Activation energy (E_a) together with conductivity prefactor (σ_0) of the samples of the RF temperature series.*

high–quality μc–Si:H samples. All the fully μc–Si:H samples of the RF temperature series ($T_S \geq 130°$ C) almost fulfill our guiding rule, which is graphically indicated by the horizontal line in the Fig. 4.38. This is in agreement with the CPM measurements (Fig. 4.33), where most of the μc–Si:H samples also exhibit rather low defect density. However, the transport properties and the expected behaviour of a real solar cell are better represented by L_{diff} (Fig. 4.36), which means that **the best sample of the RF temperature series is the sample at 250° C**. This is no surprise because all the deposition conditions used for this series were long–term optimized just for this temperature.

Table 4.15: *Summarizing table of the properties measured on the samples of the RF temperature series. For the full original name of the samples see Table 4.13.*

Sample T_S	X_C [%]	RMS [nm]	AGS [nm]	L_{diff} [nm]	σ_d [$\Omega^{-1}cm^{-1}$]	σ_0 [$\Omega^{-1}cm^{-1}$]	E_a [eV]	H_{ERDA} [%]	H_{FTIR} [%]
250°C	86.7	7.8	109	**223**	8.0×10^{-8}	7.8×10^{1}	0.53	–	9.3
220°C	85.6	8.2	100	186	4.4×10^{-7}	5.0×10^{1}	0.48	–	9.4
190°C	85.4	9.1	87	142	2.0×10^{-7}	2.9×10^{1}	0.48	11	9.6
160°C	80.5	9.1	83	75	5.8×10^{-7}	1.0×10^{1}	0.43	12	9.5
130°C	79.7	8.0	131	47	1.0×10^{-7}	3.5×10^{1}	0.50	14	9.9
100°C	74.8	21.0	199	65	1.0×10^{-7}	3.5×10^{0}	0.45	16	10.4
80°C	66.4	26.8	376	119	4.0×10^{-9}	3.3×10^{-2}	0.41	18	10.8
60°C	73.4	7.1	100	38	3.0×10^{-7}	2.0×10^{0}	0.40	18	11.1
40°C	0	5.9	71	41	1.0×10^{-9}	4.0×10^{-4}	0.35	24	10.4

4.9 RF temperature series on plastic substrates

With the motivation to test the behaviour of films deposited on real plastic substrates and test the applicability of our methods for the diagnostics of films prepared on flexible substrates, we introduced 0.2 mm thick PET (polyethylene terephtalate) foil of the same dimensions as the glass substrate (Fig. 2.3) into the deposition chamber. The PET was placed just next to the glass substrate in a region with identical deposition conditions. Due to the maximum allowed temperature for the PET foil, we prepared thin Si films on both glass and PET substrates for temperatures not greater than 100° C as summarized in Table 4.16.

Table 4.16: *Overview of substrate materials used for the samples of the RF temperature series. Legend: "√" = was used, "–" = was not used.*

Sample (T_S)	d [nm]	Glass	PET
Stm 232 (250°)	900	√	–
Stm 233 (220°)	900	√	–
Stm 235 (190°)	850	√	–
Stm 236 (160°)	900	√	–
Stm 237 (130°)	900	√	–
Stm 238 (100°)	850	√	√
Stm 246 (80°)	900	√	√
Stm 247 (80°)	900	√	√
Stm 241 (60°)	850	√	√
Stm 248 (50°)	700	√	√
Stm 242 (40°)	850	√	√

In Fig. 4.40 we added one more sample (compared to Fig. 4.36) prepared at T_S=50° C with slightly different position in the deposition chamber. However, the comparison of the properties of thin Si films on glass and PET substrates is not disturbed by this small deviation.

Samples on the PET substrates do not exhibit any pronounced differences neither in topography (Figs. 4.34 and Fig. 4.39) and roughness nor in the values of the diffusion length (Fig. 4.40). The only exception is the surface of sample at T_S=40° C, which grew more rough on PET substrate then on glass. This was probably caused by higher initial roughness introduced by the PET substrate. Further roughening occurred probably due to decreased surface diffusion of precursors at 40° C.

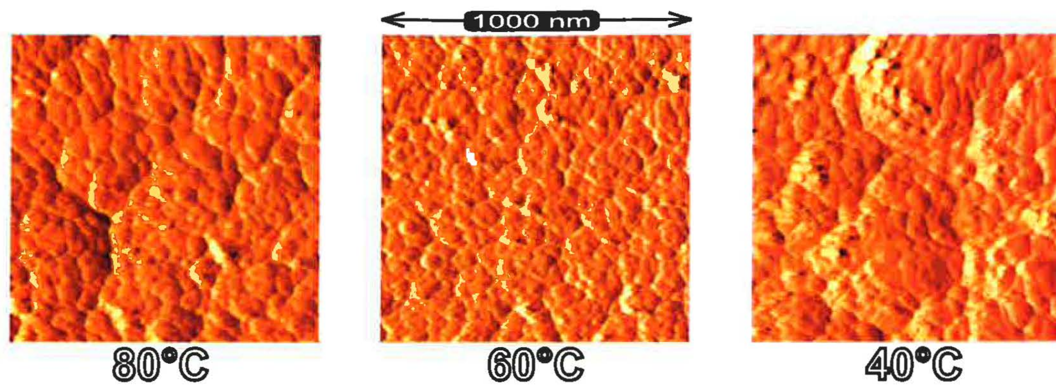

Figure 4.39: *AFM surface topography of the selected samples of the RF temperature series prepared on PET substrates.*

In spite of slight changes in topography (see values of RMS roughness in Fig. 4.40), the transport properties (see values of L_{diff}) of thin Si films of RF temperature series deposited simultaneously on glass and PET substrate give a very good agreement. This is a good promise for the applicability of plastic substrates (e.g. PET) in the deposition of thin Si films and solar cells without a major risk of the deprivation of electrical and transport properties.

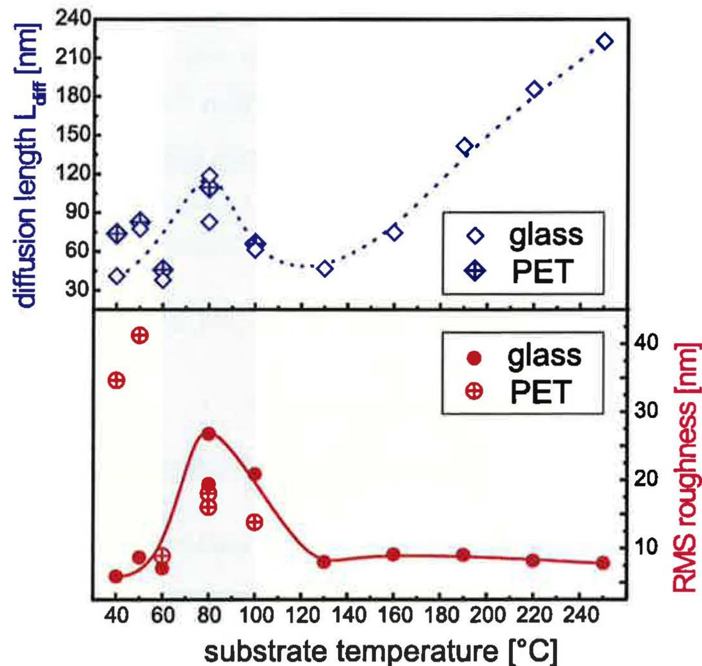

Figure 4.40: *Ambipolar diffusion length (L_{diff}) and RMS roughness of the RF temperature series on glass and PET substrates.*

4.10 Test of increased deposition rate

Due to the recent works presenting faster deposition of the microcrystalline silicon [37, 69] we also attempted to prepare samples with high r_d and study their properties. The samples prepared at higher pressure of 200 Pa and higher plasma power of 100 W (high p&P) turned out to be more amorphous showing rather low SSPG diffusion length and crystallinity below the percolation threshold. The deposition conditions were selected to correspond to the best sample of the dilution series (Table 4.8), which was the sample at r_H=51 with crystallinity exactly at the percolation threshold.

Table 4.17: *Overview of the main deposition parameters of the high p&P sample.*

Sample	thick. [nm]	dil. r_H	T_S [°C]	freq. [MHz]	P_{eff} [W]	p_{tot} [Pa]	$[H_2]$ [sccm]	$[SiH_4]$ [sccm]
030527-2i (high p&P)	1100	50	80	54.24	**100**	**200**	100	2.0

Table 4.18: *Additional deposition parameters of the high p&P sample.*

Average deposition rate r_d	~0.61 nm/s
Plasma power density	~2.60 W/cm^2

In this section we present the data for the high p&P sample together with the data for the samples of the dilution series (Section 4.6) to demonstrate the change of properties caused by the increase of pressure and applied plasma power.

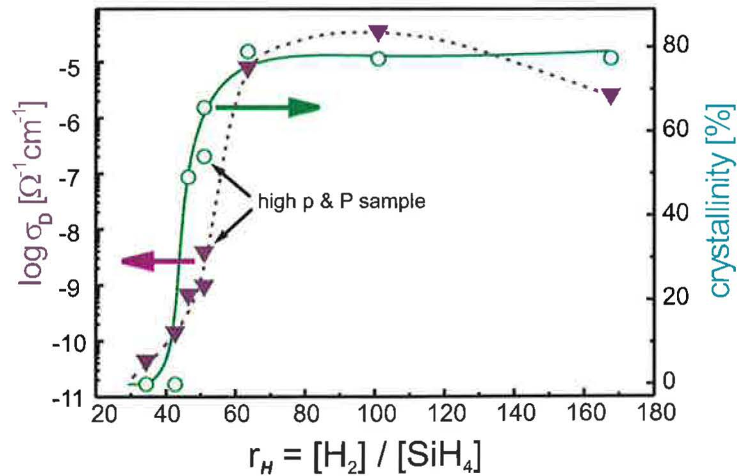

Figure 4.41: *Crystalline volume ratio (X_c) together with values of dark conductivity (σ_D) of the high p&P sample together with the samples of dilution series (Section 4.6).*

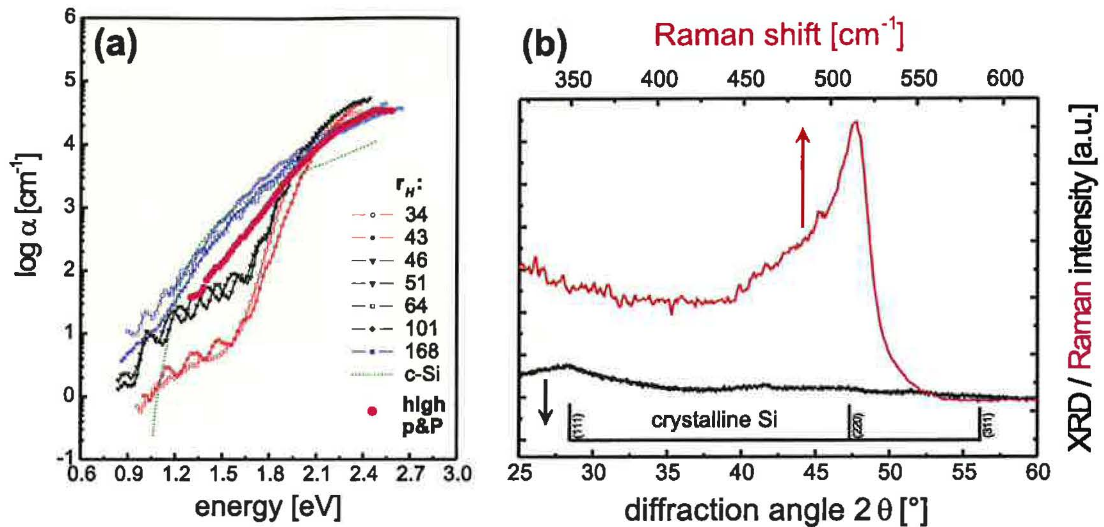

Figure 4.42: *(a) CPM spectra and (b) XRD & Raman spectra the high p&P sample. The CPM spectra provide a comparison of the high p&P sample with the samples of dilution series (Section 4.6).*

Summary of the data obtained from the measurements of the high p&P sample shows its "dual" behaviour. The results can be divided into two groups indicating either amorphous or microcrystalline structure:
Amorphous data:

- XRD pattern with no crystalline peaks (Fig. 4.42)
- dark conductivity in the amorphous range (Fig. 4.41)
- activation energy and dark conductivity typical for amorphous silicon (Fig. 4.44)
- low roughness and very low SSPG diffusion length (Fig. 4.43)

Microcrystalline data:

- crystalline peak in Raman signal corresponding to 54% crystallinity (Fig. 4.42)
- shape of the CPM spectrum is more microcrystalline–like (Fig. 4.42)

These data partially resemble the properties of mixed–phase sample with r_H=51 of the dilution series (Section 4.6) and partially the sample at T_S=50° C of the VHF temperature series (Section 4.7). Is seems that the high p&P sample is close to the mixed–phase structure, but probably at the amorphous side. The shape of its CPM spectrum (Fig. 4.42(a)) and very low L_{diff} (Fig. 4.43) and also very high E_a (Fig. 4.44) suggest amorphous structure with a lot of defects. The AFM topography

pictures (Fig. 4.45) resemble the structure of the sample at T_S=60° C of the VHF temperature series (Section 4.7) with some type of a grainy structure. Especially, the local current map is quite similar, exhibiting also some darker spots corresponding to less conductive areas, which we attributed to the microcrystalline grains isolated by the amorphous tissue.

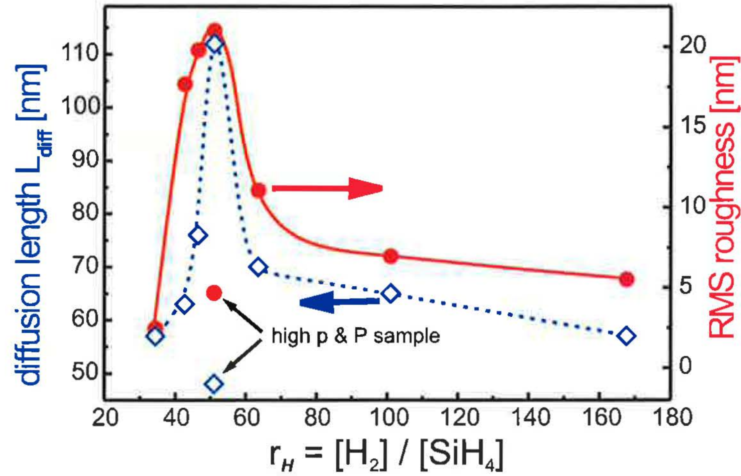

Figure 4.43: *Surface RMS roughness together with the values of the ambipolar diffusion lengths L_{diff} of the high p&P sample together with the samples of dilution series (Section 4.6).*

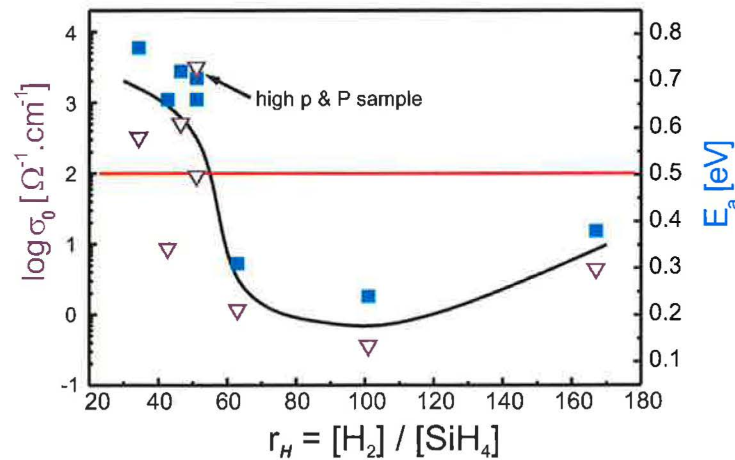

Figure 4.44: *Activation energy (E_a) together with conductivity prefactor (σ_0) of the high p&P sample together with the samples of dilution series (Section 4.6).*

The properties of this sample clearly demonstrate the difficulty of optimization, which should follow every single change of any deposition parameter. In fact, a new series of samples with variable dilution r_H should be prepared in order to find the

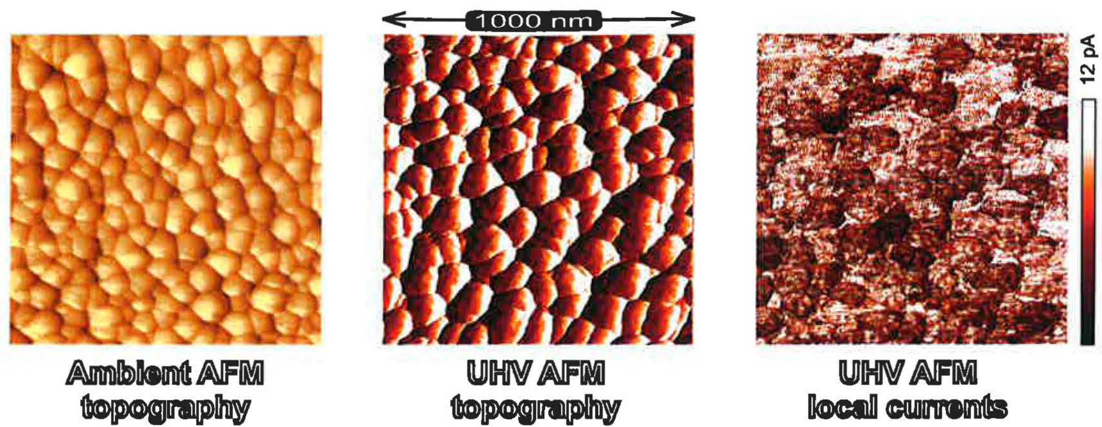

Figure 4.45: *AFM images of the high p&P sample showing (a) topography measured in air, (b) topography and (c) map of local currents measured in UHV. The bias voltage (applied to the sample) was +10 V.*

Table 4.19: *Summarizing table of the properties measured on the high p&P sample.*

Sample	X_C [%]	RMS [nm]	AGS [nm]	L_{diff} [nm]	σ_d [$\Omega^{-1}cm^{-1}$]	σ_0 [$\Omega^{-1}cm^{-1}$]	E_a [eV]
high p&P	54.0	4.7	–	48	4.0×10^{-9}	1.6×10^{3}	0.69

a–Si:H/μc–Si:H transition and understand the growth at the new conditions (with higher pressure and higher power).

This is exactly how we continued in the research: four series with variable dilution were deposited with a new cathode design [69] to achieve both very high deposition rate and good quality of the deposited films. The deposition conditions of these new high rate dilution series follow the conditions of the best sample of this work (Section 5.3), i.e., T_S=250° C. The transition from a–Si:H to μc–Si:H with all the typical features (summarized in Section 5.2) appeared also in these high rate dilution series with r_d ~3nm/s [200, 201]. The work on further increase of r_d and optimization of properties of these films is now in progress [202].

Chapter 5

DISCUSSION

5.1 General properties

Contrary to amorphous silicon which is rather homogeneous both in structure and electrical properties, the microcrystalline counterpart is much more complicated material. Since the properties of the whole thin film are markedly determined by its structure, it is logical to start the study on μc–Si:H just by the exploration of its structure as we attempted in Chapter 3. This chapter dealt with selected samples and showed some typical or interesting properties of thin Si films.

Electrical properties are significantly determined by the structure of the deposited films and especially in the case of microcrystalline silicon with complicated microstructure the relation between structure and properties is not simple. It is thus logical to start the study of properties of thin μc–Si:H films by their structure as presented in Section 3.2.

Firstly, we did a simple test of thickness inhomogeneity that was previously indicated [115] by different values of diffusion lengths obtained in parallel (SSPG) or perpendicular direction (SPV). The "thickness profile" was obtained by simple mechanical abrasion of one sample and subsequent Raman measurements with high lateral resolution (spot of 2 μm moving with precision of few micrometers) [161]. We obtained increasing trend of crystallinity with increasing thickness of film, which is consistent with all published works describing the structure of μc–Si:H shown in Fig. 3.3.

After this simple measurement, we employed AFM to probe the surface and by using the surface topography images of samples with different thickness (details in Section 3.2.5) we reconstructed the cross–sectional structure of microcrystalline grain as shown in Fig. 3.14, [17].

After comparing our AFM and Raman results with cross–sectional TEM pictures (see Fig. 3.2) we came with the simple model of growth of the microcrystalline grains [163]. We described these grains by cones capped by parts of spheres of a certain radii. Even such a substantial simplification produced results in good agreement with the experimental data as shown in the case of surface roughness (Fig. 3.12, [164]), dark conductivity and crystallinity of the growing film [163].

5.2 Typical features of a–Si:H/μc–Si:H transition

It is interesting to observe how the optimization of amorphous and microcrystalline silicon leads to one common conclusion, which would be the mixed phase (a–Si:H + μc–Si:H). The improved electrical properties of amorphous silicon could be ascribed to some amount of very small crystallites in the material, possibly improving the light induced degradation of a–Si:H based solar cells. The best μc–Si:H based solar cells are deposited at the dilution close to the mixed phase material both for low temperatures $T_S \sim 225°C$ [26, 195] and for very low temperatures $T_S \sim 75°C$ [48]. This beneficial symbiosis of amorphous and microcrystalline silicon in the thin film has been reported in many works, recently by our group in [203], where the promising transport properties of the multi layer structure (with alternating amorphous and microcrystalline layers) are demonstrated.

During the study of series of samples we noticed the fact that there is always a peak in roughness [164], which can be more or less pronounced. After the comparison with the crystallinity and conductivity data we concluded that this is the *typical feature of the transition* between amorphous and microcrystalline silicon (also called *mixed–phase*) as reported by other laboratories, e.g. [178, 67, 49, 168]. We also found a clear coincidence of the peak in RMS roughness and ambipolar diffusion length L_{diff} [164, 199, 193] confirmed by results in other laboratories both for PECVD [67] and even for HWCVD samples [196, 90, 92]. This transition from a–Si:H to μc–Si:H growth can be caused by the change of various deposition parameters like thickness, dilution, temperature always exhibiting the same typical features.

Transition can be delayed by the a–Si:H sublayer decreasing the nucleation density. The resulting film has than larger grains (AGS 374 nm) compared to AGS 182 nm with no a–Si:H sublayer. These larger grains also bring higher surface roughness (see the absolute value of RMS roughness for the mixed–phase peaks in Fig. 5.1). Higher nucleation density of the thickness series with 3% dilution lead to even smaller AGS

of a mixed–phase sample (AGS=83nm). The corresponding RMS roughens is also smaller.

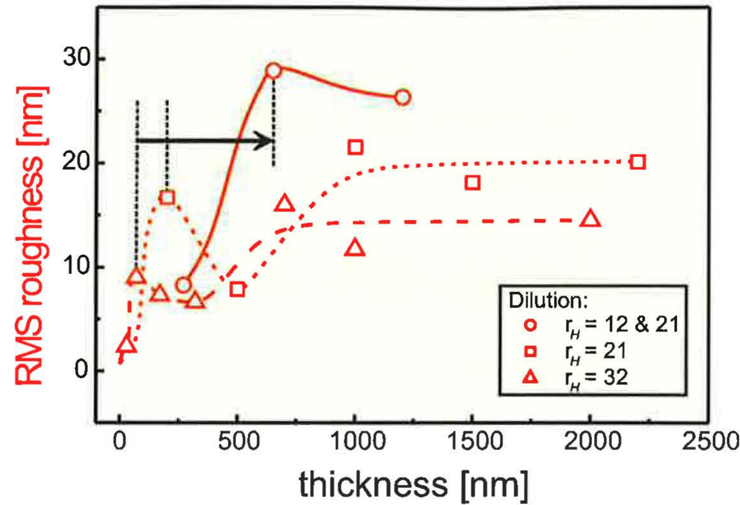

Figure 5.1: *Surface RMS roughness summarized for all three thickness series at 250°C with different dilution ratios r_H. The position of the peak is shifting with increasing value of r_H. However, the values of roughness follow the same trend. The solid line shows the values of roughness for the series with delayed nucleation.*

In the Section 3.2.6 the importance of the peak in roughness as a sensitive tool for the detection of the a–Si:H/μc–Si:H transition was explained. In the Fig. 5.1 we compare the values of the RMS surface roughness for three thickness series prepared at 250°C with dilution ratios r_H=21, 32 (Table 4.2 & Fig. 4.3 and Table 4.4 & Fig. 4.8, respectively) and r_H=21 & 12 (Table 3.5 and Fig. 3.19). It is a comparison of the small thickness series with a–Si:H sublayer with two other thickness series without this sublayer. All the series show a peak in roughness which corresponds to the mixed–phase. This peak is shifting with the dilution, which means that at higher values of r_H (lower c_{SiH_4}) the formation of μc–Si:H structure is faster (roughness peak at smaller thicknesses) and thinner a–Si:H incubation layers are obtained or even omitted. The presence of the a–Si:H sublayer brought a significant shift of the roughness peak meaning that the μc–Si:H started to grow at much higher thicknesses (~500 nm), where the other series exhibit a fully μc–Si:H surface. The absolute value of roughness indicates another important fact. In the case of samples with amorphous sublayer the nucleation of microcrystalline grains was not only shifted to higher thicknesses, but also the nucleation density has decreased. This lead to the formation of much larger microcrystalline grains thus producing more rough surfaces. This is also seen in the case of saturated roughness values at thicknesses above 1000 nm, where smoother

surfaces of samples with r_H=32 are a natural consequence of a fast onset of μc–Si:H structure typical for higher number of smaller microcrystalline grains.

Although the thickest samples (1500 & 2200 nm) exhibit higher values of L_{diff} (Fig. 4.4), the fact that they do not fulfill our guiding rule (Fig. 4.5) means that the grain boundaries disturb the macroscopic transport. We expect that i–layers made of such films would result in smaller conversion efficiencies of solar cells. This is supported by our measurements [180] of record efficiency samples [12], where we obtained similar L_{diff} values and the guiding rule was fulfilled.

Different substrate materials may provide quite different conditions for the growth of the deposited films [78, 107]. Besides the different nucleation density, which is of chemical character, the substrate materials (glass and NiCr) also differ in the conductivities. This may influence the plasma confinement just above the substrate, even if the substrate has a floating potential. Virtually, non–conductive substrates develop more negative surface potential in plasma discharge [78]. This causes higher bombardment of the positive ions disturbing the growing crystalline structure [58], as discussed in the Section 2.1.4. This theoretical expectation is in agreement with the AFM observation of surfaces of real samples in Figs. 4.9 and 4.13 & 4.14. The Si films on glass substrates have always smaller density of μc–Si:H grains than the metal coated glass used in the same deposition.

This finding of the different nucleation density for different substrates, has, in fact, positive impact on solar cell applications. The utilization of p–i–n or n–i–p structures means that the i–layer is never grown directly on glass. The amorphous incubation layer is thus overcome by μc–Si:H p or n layer and a faster onset of crystalline growth can be easily obtained.

Within all the series of samples, we have observed another effect of the bottom NiCr electrode, i.e., better adhesion of deposited thin Si films on NiCr compared to the adhesion on bare glass substrate. The adhesion can be also improved by the introduction of rough substrate. The results in Section 3.3.6 indicate that the films with higher residual compressive stress ($\sigma_r \sim$ -1 GPa) are more likely to peel–off.

Continuing in the research of thin Si films prepared under a wide range of different deposition conditions (Chapter 4) we found similar behaviour of properties of samples when the structure is changed from amorphous to microcrystalline independent of the reason of this change (thickness, gas dilution, temperature...). Based on these results (Chapter 4 and references within) we attempted to summarize [110, 193] the typical features of the a–Si:H/μc–Si:H transition:

- a clear peak in ambipolar diffusion length (L_{diff}) and surface RMS roughness
- drop of dark DC conductivity to $\sigma_d < 10^{-7}\Omega^{-1}cm^{-1}$ and crystallinity to $X_C < 70\%$
- percolation threshold (just interconnected network of microcrystalline grains) accompanied by large grain boundaries (LGBs) formation

For the explanation of dramatic changes of transport properties in fully microcrystalline films we formulated a simple rule [180] for monitoring the occurrence of LGBs. This rule was applied to all samples presented in this work. It is based on the values of conductivity prefactor σ_0 and activation energy E_a, which must fulfill the following conditions:

- $\sigma_0 \geq 100\ \Omega^{-1}cm^{-1}$, $\quad E_a \geq 0.5\ eV$

and then μc–Si:H film is free from large grain boundaries acting as potential barriers and the transport properties are very good. This typically favours the samples with low nucleation density having larger grains and smaller portion of grain boundaries, see samples of dilution series in Section 4.6.

However, not all the changes of electrical properties are simply derived from the structure. This was the case of samples of both temperature series (Sections 4.7 and 4.8), where very similar topographies were observed for samples with dramatically different transport properties. We employed the guiding rule, which gave consistent results, i.e., samples with poor transport properties did not fulfill this rule. However, for the explanation of this behaviour, we had to find some additional information since the structure did not provide any reasonable answer. By taking into account the fact that the samples were prepared at rather low temperatures, we measured the hydrogen content c_H and these measurements gave us a clear answer, i.e., change of nature of grain boundaries containing more hydrogen as the temperature was decreased.

The observation of samples of the VHF temperature series however shows another effect, i.e., hydrogen compensates the decreasing mobility of Si growth precursors leading to surprisingly high crystallinities for samples close to RT (X_C=50% at 35° C).

Peak in hydrogen content attributed to the transition zone structure [53] was in the case of both temperature series combined with an additional effect – i.e., the increase of c_H due to lower substrate temperature. So, the changes of properties of samples with variable T_S are more complicated to explain than in the case of dilution series.

From the role of hydrogen in the series of our samples we have learned that there must be some optimal amount of hydrogen, which is:

- necessary amount (more than 1%) to passivate the defects (as known from the behaviour of poly–Si films [204])
- and below the upper limit of H-content (~15%) limiting the transport properties (as seen in the temperature series [193])

5.3 Empirical estimate of the best sample

Firstly, we studied three thickness series prepared at different dilutions r_H and temperatures T_S. The samples were analysed in order to understand the growth of the μc–Si:H structure. Another result is the estimation of optimal thickness with regard to best optoelectronic properties. Based on the results of our thickness series (Sections 4.4 & 4.5), the film thickness should be 500–1000 nm. Such a range is given by two contrary trends. On one hand, the L_{diff} increases with increasing thickness (Figs. 4.4 & 4.10), but on the other hand at higher thickness the large grain boundaries may start to disturb the transport by decreasing the values of E_a and σ_0 (Figs. 4.5 & 4.11). For the evaluation of the sample with best optoelectronic properties we took into account X_C, σ_d, surface roughness and put an emphasis on the values of L_{diff}. The E_a and σ_0 had to exhibit good values, i.e., fulfilling our guiding rule (Section 3.3.5) as well. The overview of the best samples of the next three series is as follows:

- Dilution series - best sample - r_H=51 (at 80° C)
- VHF temperature series - best sample - T_S=100° C
- RF temperature series - best sample - T_S=250° C

We selected **Stm 232 (900 nm)** from RF temperature series at T_S=250° C with L_{diff}=223 nm as the **best sample** of the whole work. Selection of this sample was based on the results of precise measurements, but the series themselves are quite difficult to compare. The series were prepared in different deposition systems in three laboratories. Each series served another purpose, which was successfully completed. Fortunatelly all the series exhibited the same trends in properties at the a–Si:H/μc–Si:H transition and so these trends could have been generalized.

Coming back to the benchmark of the best sample for the i–layer of the solar cell: Thin Si films prepared at low temperatures we will probably hardly achieve record efficiencies, but comparable properties at lower production costs may be the strong arguments for the production of solar cells made of thin Si films at T_S=80–100°C.

Chapter 6

FINAL CONCLUSIONS

The research performed within this thesis contributes to the knowledge of the structure and properties of thin Si films, which are used in many applications. Besides electronic devices (e.g. TFT's) the most important application are the thin film solar cells, which can play a major role in renewable energetics. The solar cells must exhibit rather high efficiency values at an affordable price to be successful on the market. To achieve these goals, the understanding of the properties of thin Si films is essential.

The state-of-the-art knowledge of thin Si films when the author entered this field (~1999) was the rediscovery of μc–Si:H and fabrication of first μc–Si:H based solar cells in 1994 [33]. It was reported that the structure of μc–Si:H reflects the deposition parameters, especially silane concentration c_{SiH_4} [52]. The measurements of μc–Si:H by combined AFM revealed different conductivity of a–Si:H and μc–Si:H structures with high lateral resolution [154]. There had been also the first depositions of solar cells at low temperatures (T_S=100° C) [47]. The existence of transition between a–Si:H and μc–Si:H and the hydrogen content in the thin Si films was reported [53].

An overview of techniques used for the preparation and characterization of the thin Si films is presented in the theoretical part of this work. Special attention was given to the techniques developed and actively used in the group of Dr. Jan Kočka at the Institute of Physics, AS CR in Prague. In the experimental part we present a complex study of several series of intrinsic a–Si:H and μc–Si:H films. We used several characterization techniques and showed the influence of key deposition parameters on the structure and properties of the films. The research of properties of thin Si films is still far from being complete. It will continue with the emphasis on reducing the production costs of these films by using cheap substrates and fast depositions. In the last decade it underwent a dramatic development, to which we contributed the following results:

Structure of μc–Si:H films:

- demonstration of structure evolution with increasing thickness by the measurement of crystallinity in the thickness profile created by the Calotest
- construction of the grain cross–sectional scheme based on the AFM images of the thickness series; two different stages of growth (expansion and elongation) were detected
- understanding of the growth of the microcrystalline grains and introduction of a simple geometrical model of growth (based on the results of three thickness series)
- first empirical estimation of the diffusion length of precursors L_{prec} on the growing surface (from the AFM images of a mixed–phase sample with smooth a–Si:H)
- visualization of small grains (crystallites) and large grains (aggregates) in μc–Si:H by combined AFM
- introduction of simple guiding rule (based on E_a and σ_0) for monitoring the quality of grain boundaries in μc–Si:H
- exploration of properties of thin Si films prepared at lower temperatures
- confirmation of important role of hydrogen content, which influences the quality of grain boundaries

Discovery of typical features at the a–Si:H/μc–Si:H transition:

- sharp increase of σ_d and X_C when the percolation threshold is crossed
- coincidence of peak in RMS roughness and L_{diff} by SSPG for the mixed–phase samples

The author participated in the preparation of thin films by PECVD and performed all the AFM measurements and image processing presented in the thesis (Section 2.4 and Chapters 3 and 4). The author also gathered the data from other techniques and significantly contributed to the interpretation of the observed trends of thin Si films (Chapters 4). Furthermore, the author suggested and performed the evaluation of average μc–Si:H grain size by means of PSDF (Section 2.4.3). The comparison of internal stress in thin Si films evaluated from Raman and XRD measurements (Section 3.3.6) is another important author's contribution.

Bibliography

[1] International Energy Agency. *Energy 2050, Scenarios for a Sustainable Future.* IEA, OECD (2003). http://www.iea.org/Textbase/publications/free_all.asp.

[2] K. Kurokawa. *PV Industries: Future Visions.* In *Proceedings of the 4th IEA-PVPS international conference*, Osaka, Japan (2003). IEA-PVPS.

[3] R.J. Hassett. *Future visions of U.S. photovoltaics industry.* In *Proceedings of the 4th IEA-PVPS international conference*, Osaka, Japan (2003). IEA-PVPS.

[4] R. Sellers. *PV: Progress and Promise.* In *Proceedings of the 4th IEA-PVPS international conference*, Osaka, Japan (2003). IEA-PVPS.

[5] International Energy Agency - Photovoltaics Power Systems Programme. *IEA PVPS.* http://www.oja-services.nl/iea-pvps (2005). International statistics – Glossary.

[6] U.S. Department of Energy - National Centre for Photovoltaics. *NREL - NCPV.* http://www.nrel.gov/ncpv/energy_payback.html (2005). Information Resources – FAQ.

[7] A.V. Shah, R. Platz and H. Keppner. *Thin-film silicon solar cells: A review and selected trends.* Sol. Energy Mater. Sol. Cells, **38**, 501 (1995).

[8] M.A. Green, K. Emery, D. King, S. Igari and W. Warta. *Solar cell efficiency tables (ver. 17).* Progress in Photovoltaics: Res. and Appl., **9**, 49–56 (2001).

[9] J. Meier, J. Spitznagel, U. Kroll, C. Bucher, S. Faÿ and A. Shah. *High efficiency micromorph tandem solar cells.* In *Proceedings of the 3rd World Conference on Photovoltaic Energy Conversion*, Osaka, Japan (2003). WCPEC.

[10] J. Yang, A. Banerjee and S. Guha. *Triple-junction amorphous silicon alloy solar cell with 14.6% initial and 13.0% stable conversion efficiencies.* Appl. Phys. Lett., **70**, 2975–2977 (1997).

[11] K. Yamamoto, M. Yoshimi, Y. Tawada, Y. Okamoto and A. Nakajima. *Thin film Si solar cell fabricated at low temperature.* J. Non-Crystal. Solids, **266–269**, 1082–1087 (2000).

[12] Y. Nasuno, M. Kondo and A. Matsuda. *Effects of substrate surface morphology on microcrystalline silicon solar cells.* Jpn. J. Appl. Phys., **40**, L303–L305 (2001).

[13] Y. Tawada, H. Yamagishi and K Yamamoto. *Mass productions of thin film silicon PV modules.* Sol. Energy Mater. Sol. Cells, **78**, 647–662 (2003).

[14] T. J. Rinke, R. B. Bergmann and J. H. Werner. *Quasi–monocrystalline silicon for thin-film devices.* Appl. Phys. A, **68**, 705–707 (1999).

[15] J. Meier, S. Dubail, R. Flückinger, D. Fischer, H. Keppner and A. Shah. In *Proceedings of the 1st World Conference on Photovoltaic Energy Conversion*, Hawaii, USA (1994). WCPEC.

[16] J. Yang, A. Banerjee and S. Guha. *Amorphous silicon based photovoltaics – from Earth to the 'final frontier'.* Sol. Energy Mater. Sol. Cells, **78**, 597–612 (2003).

[17] A. Fejfar, T. Mates, O. Čertík, B. Rezek, J. Stuchlík, I. Pelant and J. Kočka. *Model of electronic transport in microcrystalline silicon and its use for prediction of device performance.* J. Non-Crystal. Solids, **338–340**, 303–309 (2004).

[18] M.A. Green. *Green energy visions: personal views of the future of photovoltaics.* In *Proceedings of the 3rd World Conference on Photovoltaic Energy Conversion*, Osaka, Japan (2003). WCPEC.

[19] Nicolas Wyrsch. *La technique de temps–de–vol et la détermination des propriétés électroniques du silicium amorphe hydrogéné.* PhD thesis, Institut de Microtechnique, Université de Neuchâtel, Switzerland (1992).

[20] L. Ley. *The Physics of Hydrogenated Amorphous Silicon II.* In J.D. Joanopoulos and G. Lucovsky, editors, *Topics in Applied Physics*, page 61, Berlin, Germany (1984). Springer Verlag.

[21] Y. Saito, M. Aomori and H. Kuwano. *Effects of hydrogen passivation on the electrical conduction in undoped polycrystalline silicon films.* J. Appl. Phys., **81**(2), 754–757 (1997).

[22] N.H. Nickel, N.M. Johnson and W.B. Jackson. *Hydrogen passivation of grain boundary defects in polycrystalline silicon thin films.* Appl. Phys. Lett., **62**(25), 3285–3287 (1993).

[23] Y. Ishikawa, Y. Yamamoto, T. Hatayama, Y. Uraoka and T.Fuyuki. *Crystallographic analysis of high quality poly–Si thin films deposited by atmospheric pressure chemical vapor deposition.* Sol. Energy Mater. Sol. Cells, **74**, 255–260 (2002).

[24] D.L. Staebler and C.R. Wronski. *Reversible condictivity changes in discharge produced amorphous Si.* Appl. Phys. Lett., **31**, 292–294 (1977).

[25] H. Tsubomura and H. Kobayashi. *Solar cells.* Critical Rev. in Sol. State and Mat. Sci., **18**(3), 261–326 (1993).

[26] A.V. Shah, J. Meier, E. Vallat-Sauvain, N. Wyrsch, U. Kroll, C. Droz and U. Graf. *Material and solar cell research in microcrystalline silicon.* Sol. Energy Mater. Sol. Cells, **78**, 469 (2003).

[27] H.F. Sterling and R.C.G. Swann. *Chemical vapour deposition promoted by r.f. discharge.* Solid State Electron., **8**, 653–654 (1965).

[28] S. Vepřek and V. Mareček. *The preparation of thin layers of Ge and Si by chemical hydrogen plasma transport.* Solid State Electron., **11**, 683 (1968).

[29] S. Usui and M. Kikuchi. *Properties of heavily doped GD–Si with low resistivity.* J. Non-Crystal. Solids, **34**, 1 (1979).

[30] W.E. Spear, G. Willeke, P.G. LeComber and A.G. Fitzgerald. *Electronic properties of microcrystalline silicon films prepared in a glow discharge plasma.* Journal de Physique, **42**(NC4), 257 (1981).

[31] G. Lucovsky, C. Wang, R.J. Nemanich and M.J. Williams. *Deposition of μc–Si and μc–Si–C thin films by remote plasma enhanced chemical vapor deposition.* Sol. Cells, **30**, 419 (1991).

[32] M. Faraji, S. Gokhale, S.M. Choudhari, M.G. Takwle and S.V. Ghaisas. *High mobility hydrogenated and oxygenated microcrystalline silicon as a photosensitive material in photovoltaic applications.* Appl. Phys. Lett., **60**, 3289–3291 (1992).

[33] J. Meier, R. Flückinger, H. Keppner and A. Shah. *Complete microcrystalline p–i–n solar cell - crystalline or amorphous behavior.* Appl. Phys. Lett., **65**, 860–862 (1994).

[34] B. Rech, T. Roschek, T. Repman, J. Müller, R. Schmitz and W. Appenzeller. *Microcrystalline silicon for large area thin film solar cells.* Thin Sol. Films, **427**, 157–165 (2003).

[35] L. Feitknecht, O. Kluth, Y. Ziegler, X. Niquille, P. Torres, J. Meier, N. Wyrsch and A. Shah. *Microcrystalline n–i–p solar cells deposited at 10 Å/s by VHF-GD.* Sol. Energy Mater. Sol. Cells, **66**, 397 (2001).

[36] J.K. Rath. *Low temperature polycrystalline silicon: a review on deposition, physical properties and solar cell applications.* Sol. Energy Mater. Sol. Cells, **76**, 431–487 (2003).

[37] T. Matsui, M. Kondo and A. Matsuda. *Origin of the omproved performance of high–deposition–rate microcrystalline silicon solar cells by high–pressure glow discharge.* Jpn. J. Appl. Phys., **42**, L901–L903 (2003).

[38] M. Matsumoto, M. Shima, S. Okamoto, K. Murata, M. Tanaka, S. Kiyama, H. Kakiuchi, K. Yasutake, K. Yoshii, K. Endo and Y. Mori. *Extremely high-rate deposition of silicon thin films prepared by atmospheric plasma CVD method with rotary electrode.* In *Proceedings of the 3rd World Conference on Photovoltaic Energy Conversion*, Osaka, Japan (2003). WCPEC.

[39] G. Ganguly and A. Matsuda. *Defect formation during growth of hydrogenated amorphous silicon.* Phys. Rev. B, **47**, 3661 (1993).

[40] Y. Nasuno, M. Kondo and A. Matsuda. *Passivation of oxygen–related donors in microcrystalline silicon by low temperature deposition.* Appl. Phys. Lett., **78**(16), 2330–2332 (2001).

[41] K. Zellama, H. Labidi, P. Germain, H.J. von Bardeleben, L. Chahed, M.L. Theye, P. Roca i Cabarrocas, C. Godet and J.P Stoquert. *Systematic study of light-induced effects in hydrogenated amorphous silicon.* Phys. Rev. B, **45**(23), 13314–13322 (1992).

[42] J.N. Lee, B.J. Lee, D.G. Moon and B.T. Ahn. *Effect of deposition temperature on the crystallization mechamism of amorphous silicon films on glass.* Jpn. J. Appl. Phys., **36**, 6862–6866 (1997).

[43] M.K. van Veen and R.E.I. Schropp. *Beneficial effect of a low deposition temperature of hot-wire deposited intrinsic amorphous silicon for solar cells.* J. Appl. Phys., **93**(1), 121–125 (2003).

[44] T. Mates, A. Fejfar, M. Ledinský, K. Luterová, P. Fojtík, H. Stuchlíková, I. Pelant, J. Kočka, A. Macková, M. Ito, K. Ro and H. Uyama. *Effect of substrate temperature and hydrogen dilution on thin silicon films deposited at low substrate temperatures.* In *Proceedings of the 3rd World Conference on Photovoltaic Energy Conversion*, Osaka, Japan (2003). WCPEC.

[45] J. Kočka, T. Mates, P. Fojtík, M. Ledinský, K. Luterová, H. Stuchlíková, J. Stuchlík, I. Pelant, A. Fejfar, M. Ito, K. Ro and H. Uyama. *Formation of microcrystalline silicon at low temperatures and role of hydrogen.* J. Non-Crystal. Solids, **338–340**, 287–290 (2004).

[46] Y. Nasuno, M. Kondo and A. Matsuda. *Microcrystalline silicon thin-film solar cells prepared at low temperature*, page A15.5. MRS Symp. Proc. **664**, San Francisco, USA (2001).

[47] M. B. Schubert. *Low temperature silicon deposition for large area sensors and solar cells.* Thin Sol. Films, **337**, 240–247 (1999).

[48] M. Ito, C. Koch, V. Švrček, M. B. Schubert and J. H. Werner. *Silicon thin film solar cells deposited under 80° C.* Thin Sol. Films, **383**, 129–131 (2001).

[49] A.S. Ferlauto, R.J. Koval, C.R. Wronski and R.W. Collins. *Extended phase diagrams for guiding plasma-enhanced chemical vapor deposition of silicon thin films for photovoltaics applications.* Appl. Phys. Lett., **80**(15), 2666–2668 (2002).

[50] X. Xu, J. Jang and S. Guha. *On the lack of correlation between film properties and solar cell performance of amorphous silicon-germanium alloys.* Appl. Phys. Lett., **62**, 1399–1401 (1993).

[51] S. Okamoto, Y. Hishikawa and S. Tsuda. *New interpretation of the effect of hydrogen dilution of silane on glow-discharged hydrogenated amorphous silicon for stable solar cells.* Jpn. J. Appl. Phys., **35**, 26–33 (1996).

[52] E. Vallat-Sauvain, U. Kroll, J. Meier, A. Shah and J. Pohl. *Evolution of the microstructure in microcrystalline silicon prepared by very high frequency glow-discharge using hydrogen dilution.* J. Appl. Phys., **87**(6), 3137 (2000).

[53] U. Kroll, J. Meier, A. Shah, S. Mikhailov and J. Weber. *Hydrogen in amorphous and microcrystalline silicon films prepared by hydrogen dilution.* J. Appl. Phys., **80**, 469 (1996).

[54] J. Koh, A.S. Ferlauto, P.I. Rovira, C.R. Wronski and R.W. Collins. *Evolutionary phase diagrams for plasma-enhanced chemical vapor deposition of silicon thin films from hydrogen-diluted silane.* Appl. Phys. Lett., **75**(15), 2286–2288 (1999).

[55] Y. Ziegler, V. Daudrix, C. Droz, R. Platz, N. Wyrsch and A. Shah. *More stable low gap a-Si:H layers deposited by PE-CVD at moderately high temperature with hydrogen dilution.* Sol. Energy Mater. Sol. Cells, **66**, 413–419 (2001).

[56] R. E. I. Schropp and M. Zeman, editors. *Amorphous and microcrystalline silicon solar cells: Modeling materials and device technology.* Kluwer Academic Publishers, Dordrecht, The Netherlands (1998).

[57] J. Perrin. *Plasma deposition of amorphous-based materials, edited by G. Bruno and P. Capezzuto and A. Madan*, page 216. Academic Press Inc., San Diego, CA, USA (1995).

[58] M. Kondo, M. Fukawa, L. Guo and A. Matsuda. *High rate growth of microcrystalline silicon at low-temperatures.* J. Non-Crystal. Solids, **266–269**, 84–89 (2000).

[59] H. Fujiwara, M. Kondo and A. Matsuda. *Plasma diagnostics and low-temperature deposition of microcrystalline silicon films in ultrahigh-frequency silane plasma.* J. Appl. Phys., **88**, 576–581 (2000).

[60] J. Daey Ouwens, R.E.I. Schropp, C.H.M. van der Werf, M.B. von der Linden, C.H.M. Marée, W.F. van der Weg, P. Rava, F. Demichelis, C.F. Pirri and E. Tresso. *Effect of electrode spacing and hydrogen dilution on a-SiC:H and a-Si:H layers.* In E.A. Schiff, M.J. Thompson, A. Madan, K. Tanaka and P.G. LeComber, editors, *Amorphous Silicon Technology*, volume 297, pages 61–66. Materials Research Society Symp. Proc. (1993).

[61] T. Matsui, M. Kondo and A. Matsuda. *Microcrystalline silicon solar cells grown at 20–30 Å/s by high-pressure silane-depletion plasma.* In *Proceedings of the 3rd World Conference on Photovoltaic Energy Conversion*, Osaka, Japan (2003). WCPEC.

[62] C. Niikura, M. Kondo and A. Matsuda. *High rate growth of microcrystalline silicon films assisted by high density plasma.* In *Proceedings of the 3rd World Conference on Photovoltaic Energy Conversion*, Osaka, Japan (2003). WCPEC.

[63] M. Kondo, S. Suzuki, Y. Nasuno, M. Tanda and A. Matsuda. *Recent developments in the high growth rate technique of device-grade microcrystalline silicon thin film.* Plasma Sources Sci. Technol., **12**(4), S111–S116 (2003).

[64] U. Graf, J. Meier, U. Kroll, J. Bailat, C. Droz, E. Vallat-Sauvain and A. Shah. *High rate growth of microcrystalline silicon by VHF–GD and high pressures.* Thin Sol. Films, **427**, 37–40 (2003).

[65] M. Kondo, S. Suzuki, Y. Nasuno and A. Matsuda. *High rate growth of device grade silicon thin films for solar cells*, page A4.3. MRS Symp. Proc. **664**, San Francisco, USA (2001).

[66] Pedro Torres. *Hydrogenated microcrystalline silicon deposited by VHF–GD for thin-film solar cells.* PhD thesis, Institut de Microtechnique, Université de Neuchâtel, Switzerland (1998).

[67] N. Wyrsch, L. Feitknecht, C. Droz, P. Torres, A. Shah, A. Poruba and M. Vaněček. *Hydrogenated microcrystalline silicon: how to correlate layer properties and solar cell performance.* J. Non-Crystal. Solids, **266–269**, 1099–1103 (2000).

[68] A. Matsuda. *Formation kinetics and control of microcrystallite in μc–Si:H from glow discharge plasma.* J. Non-Crystal. Solids, **59–60**, 767–774 (1983).

[69] C. Niikura, M. Kondo and A. Matsuda. *Preparation of microcrystalline silicon films at ultra high rate of 10 nm/s using high-density plasma.* J. Non-Crystal. Solids, **338–340**, 42 (2004).

[70] H. Curtins, N. Wyrsch, M. Favre and A.V. Shah. *Influence of plasma excitation frequency for a–Si:H thin film deposition.* Plasma Chem. and Plasma Processing, **7**, 267–273 (1987).

[71] U. Kroll, A. Shah, H. Keppner, J. Meier, P. Torres and D. Fischer. *Potential of VHF–plasmas for low–cost production of a–Si:H solar cells.* Sol. Energy Mater. Sol. Cells, **48**, 343 (1997).

[72] A.A. Howling, J.L Dorier, C. Hollenstein, U. Kroll and F. Finger. *Frequency effects in silane plasmas for plasma enhanced chemical vapor deposition.* J. Vac. Sci. Technol. A, **10**, 1080 (1992).

[73] M. Heintze. *Diagnostics of high–rate a–Si:H deposition in a variable frequency plasma.* Solid State Phenomena, **44–46**, 181 (1995).

[74] J. Dutta, U. Kroll, P. Chabloz, A. Shah, A.A. Howling, J.L. Dorier and Ch. Hollestein. *Dependence of intrinsic stress in hydrogenated amorphous silicon on excitation frequency in a plasma–enhanced chemical vapor deposition process.* J. Appl. Phys., **72**, 3220–3222 (1992).

[75] Takuya Matsui. *Material and device desing for high efficiency polycrystalline silicon thin film solar cells.* PhD thesis, Graduate School of Engineering Science, Osaka University, Japan (2002).

[76] S. Bae and S.J. Fonash. *Assessment of as-deposited microcrystalline silicon films on polymer substrates using electron cyclotron resonance-plasma enhanced chemical vapor deposition.* J. Vac. Sci. Technol. A, **17**, 1987–1990 (1999).

[77] E.A.G. Hamers, A. Fontcuberta i Morral, C. Niikura, R. Brenot and P. Roca i Cabarrocas. *Contribution of ions to the growth of amorphous, polymorphous, and microcrystalline silicon thin films.* J. Appl. Phys., **88**, 3674–3688 (2000).

KNIHOVNA MAT.-FYZ. FAKULTY
Knihovna Fr Záviský (fyz. odd.)
Ke Karlovu 3
121 16 Praha 2

[78] M. Kondo, Y. Toyoshima, A. Matsuda and K. Ikuta. *Substrate dependence of initial growth of microcrystalline silicon in plasma-enhanced chemical vapor deposition.* J. Appl. Phys., **80**, 6061 (1996).

[79] B. Kalache, A.I. Kosarev, R. Vanderhaghen and P. Roca i Cabarrocas. *Ion bombardment effects on the microcrystalline silicon growth mechanisms and structure.* J. Non-Crystal. Solids, **299–302**, 63–67 (2002).

[80] A. C. W. Biebericher, W. F. van der Weg, J. K. Rath, M. R. Akdim and W. J. Goedheer. *Gas-efficient deposition of device-quality hydrogenated amorphous silicon using low gas flows and power modulated radio-frequency discharges.* J. Vac. Sci. Technol. A, **21**, 156–166 (2003).

[81] U. Das, S. Morrison, E. Centurioni and A. Madan. *Thin film silicon materials and solar cells grown by pulsed PECVD technique.* In *Proceedings of the IEE - Circuit devices and systems*, volume 150, page 282, Hertford, United Kingdom (2003). Inst. of Elec. Eng.

[82] S. Koynov, S. Gebner, P. Rajdokovic, E. Hartmann, R. Schwarz, L Vasilev, R. Krankenhagen, I. Sieber, W. Henrion and M. Schmidt. *Initial stages of microcrystalline silicon film growth.* J. Non-Crystal. Solids, **198–200**, 1012–1016 (1996).

[83] J. R. Heath, S. M. Gates and C. A. Chess. *Nanocrystal seeding: A low temperature route to polycrystalline Si films.* Appl. Phys. Lett., **64**, 3569–3571 (1994).

[84] J.H. Zhou, K. Ikuta, T. Yasuda, T. Umeda, S. Yamasaki and K. Tanaka. *Control of crystallinity of microcrystalline silicon film grown on insulating glass substrates.* J. Non-Crystal. Solids, **230**, 857–860 (1998).

[85] P. Fojtík, K. Dohnalová, T. Mates, J. Stuchlík, I. Gregora, J. Chval, A. Fejfar, J. Kočka and I. Pelant. *Rapid crystallization of amorphous silicon at room temperature.* Phil. Mag. B, **82**(17), 1785–1793 (2002).

[86] Petr Fojtík. *New photoelectric and structural properties of non-crystalline forms of silicon.* PhD thesis, Faculty of Mathematics and Physics, Charles University, Prague, Czech Republic (2003).

[87] H. Wiesmann, A.K. Ghosh, T. McMahon and M. Strongin. *Method of producing hydrogenated amorphous silicon film.* J. Appl. Phys., **50**, 3752 (1979).

[88] H. Matsumura. *Catalytic chmical vapor deposition (CTL-CVD) method producing high quality hydrogenated amorphous silicon.* Jpn. J. Appl. Phys., **25**, L949 (1986).

[89] A.H. Mahan, E. Iwaniczko, B.P. Nelson, R.C. Reedy Jr., R.S. Crandall, S. Guha and J. Yang. *Proc.* 25th *IEEE Photovoltaic Specialists Conf., Washington*, page 1065. IEEE, New York (1996).

[90] Chisato Niikura. *Microcrystalline silicon films prepared by hot-wire assisted catalytic chemical vapor deposition: from analysis of film properties to realization of solar cells.* PhD thesis, Ecole Polytechnique, Palaiseau Cedex, France (2002).

[91] C. Niikura, J. Guillet, R. Brenot, B. Equer, J.E. Bourée, C. Voz, D. Peiro, J.M. Asensi, J. Bertomeu and J. Andreu. *Comparative study of microcrystalline silicon films prepared in low or high pressure regime by hot-wire chemical vapor deposition.* J. Non-Crystal. Solids, **266**, 385–390 (2000).

[92] C. Niikura, Y. Poissant, M. E. Gueunier, J. P. Kleider and J. E. Bourée. *Transport properties of hot-wire CVD μc-Si:H layers for solar cells.* J. Non-Crystal. Solids, **299–302**, 1179–1183 (2002).

[93] J.K. Rath, F.D. Tichelaar and R.E.I. Schropp. *Profiled poly-silicon films by hot-wire chemical vapour deposition for solar cells on cheap metal substrate.* Solid State Phenomena, **67–8**, 465 (1999).

[94] C. Niikura, S.Y. Kim, B. Drevillon, Y. Poissant, P. Roca i Cabarrocas and J.E. Bourée. *Growth mechanisms and structural properties of microcrystalline silicon films deposited by catalytic CVD.* Thin Sol. Films, **395**, 178–183 (2001).

[95] M. Ichikawa, J. Takeshita, A. Yamada and M. Konagai. *High deposition rate of polycrystalline silicon thin films prepared by hot wire cell method.* Jpn. J. Appl. Phys., **38**, L24–L26 (1999).

[96] Y. H. Yang and J. R. Abelson. *Growth of polycrystalline silicon at 470° C by magnetron sputtering onto a sputtered μc-hydrogenated silicon seed layer.* Appl. Phys. Lett., **67**, 3623–3625 (1995).

[97] S. Logothetidis and G. Kiriakidis. *Optical properties and structure of microcrystalline hydrogenated silicon prepared by radio-frequency magnetron sputtering.* J. Appl. Phys., **64**, 2389–2398 (1988).

[98] M.F. Cerqueira, M. Andritschky, L. Rebouta, J.A. Ferreira and M.F. da Silva. *Microcrystalline silicon thin films prepared by RF reactive magnetron sputter deposition.* Vacuum, **46**, 1385 (1995).

[99] S.N. Sharma, D. Das and R. Banerjee. *A simple modification fo the magnetron sputtering method for the deposition of boron–doped hydrogenated microcrystalline silicon films with enhanced doping efficiency.* Thin Sol. Films, **298**, 200–210 (1997).

[100] Y. Leconte, C. Dufour, B. Garrido and R. Rizk. *Evolution of the surface roughness with the hydrogen partial pressure for thigh deposition rate on nanocrystalline silicon films.* J. Non-Crystal. Solids, **299–302**, 87–92 (2002).

[101] Y. Mishima, M. Takei, T. Uematsu, N. Matsumoto, T. Kakehi, U. Wakino and M. Okabe. *Polycrystalline silicon formed by ultrahigh-vacuum sputtering system.* J. Appl. Phys., **78**, 217–223 (1995).

[102] M. Takeya, W.S. Park, G.S. Jong and T. Ohmi. *Plasma conditions for as–grown low temperature poly–Si formation on SiO_2 substrate by sputtering and plasma enhanced chemical vapor deposition.* J. Vac. Sci. Tech. A, **16**, 1917 (1998).

[103] P. Muller, W.M. Holber, W. Henrion, E. Nebauer, V. Schlosser, B. Selle, I. Sieber and W. Fuhs. *Low-temperature deposition of microcrystalline silicon by microwave plasma–enhanced sputtering.* Solid State Phenomena, **67–68**, 119–124 (1999).

[104] Tomáš Mates. *Deposition of microcrystalline thin silicon films by DC magnetron sputtering.* Master's thesis, Faculty of Applied Sciences, University of West Bohemia, Pilsen, Czech Republic (1999).

[105] P. Reinig, F. Fenske, W. Fuhs and B. Selle. *Crystalline silicon films grown by pulsed dc magnetron sputtering.* J. Non-Crystal. Solids, **299–302**, 128–132 (2002).

[106] P.Reinig, V.Alex, F.Fenske, W.Fuhs and B.Selle. *Pulsed dc magnetron-sputtering of microcrystalline silicon.* Thin Sol. Films, **403–404**, 86–90 (2002).

[107] J. Kočka, A. Fejfar, P. Fojtík, K. Luterová, I. Pelant, B. Rezek, H. Stuchlíková, J. Stuchlík and V. Švrček. *Charge transport in microcrystalline Si – the specific features.* Sol. Energy Mater. Sol. Cells, **66**, 61–71 (2001).

[108] J. Kočka, A. Fejfar, H. Stuchlíková, J. Stuchlík, P. Fojtík, T. Mates, B. Rezek, K. Luterová, V. Švrček and I. Pelant. *Basic features of transport in microcrystalline silicon.* Sol. Energy Mater. Sol. Cells, **78**, 493 (2003).

[109] M. Ito, K. Ro, S. Yoneyama, Y. Ito, H. Uyama, T. Mates, M. Ledinský, K. Luterová, P. Fojtík, H. Stuchlíková, A. Fejfar and J. Kočka. *Silicon thin films deposited at very low substrate temperatures.* Thin Sol. Films, **442**, 163–166 (2003).

[110] J. Kočka, A. Fejfar, T. Mates, P. Fojtík, K. Dohnalová, K. Luterová, J. Stuchlík, H. Stuchlíková, I. Pelant, B. Rezek, A. Stemmer and M. Ito. *The physics and technological aspects of the transition from amorphous to microcrystalline and polycrystalline silicon.* phys. stat. sol. (c), **1**, 1097–1114 (2004).

[111] D. Ritter, E. Zeldov and K. Weiser. *Steady-state photocarrier grating technique for diffusion length measurement in photoconductive insulators.* Appl. Phys. Lett., **49**, 791 (1986).

[112] S. M. Sze. *Physics of semiconductor devices.* John Wiley & Sons, New York, USA, 2 edition (1981).

[113] M. Hack, J. McGill, W. Czubatyj, R. Singh, M. Shur and A. Madan. *Minoriry carrier diffusion lengths in amorphous silicon-based allyos.* J. Appl. Phys., **53**, 6270 (1982).

[114] A.M. Goodman. *A method for the measurement of short minority carrier diffusion lengths in semiconductors.* J. Appl. Phys., **32**, 2550 (1961).

[115] V. Švrček, I. Pelant, J. Kočka, P. Fojtík, B. Rezek, H. Stuchlíková, A. Fejfar, J. Stuchlík, A. Poruba and J. Toušek. *Transport anisotropy in microcrystalline silicon studied by measurement of ambipolar diffusion length.* J. Appl. Phys., **89**, 1800–1805 (2001).

[116] V. Švrček, A. Fejfar, P. Fojtík, T. Mates, A. Poruba, H. Stuchlíková, I. Pelant, J. Kočka, Y. Nasuno, M. Kondo and A. Matsuda. *Importance of the transport isotropy in μc-Si:H thin films for solar cells deposited at low substrate temperatures.* J. Non-Crystal. Solids, **299–302**, 395–399 (2002).

[117] Y. Nasuno, M. Kondo and A. Matsuda. *Key issue for the fabrication of high-efficiency microcrystalline silicon thin-film solar cells at low temperatures.* Jpn. J. Appl. Phys., **41**(10), 5912–5918 (2002).

[118] M. Vaněček, J. Kočka, J. Stuchlík and A. Tříska. *Direct measurement of the gap states and band tail absorption by constant photocurrent method in amorphous silicon.* Solid State Comm., **39**, 1199–1202 (1981).

[119] M. Vaněček, J. Kočka, A. Poruba and A. Fejfar. *Direct measurement of the deep defect density in thin amorphous silicon films with the absolute constant photocurrent method.* J. Appl. Phys., **78**, 6203 (1995).

[120] A. Fejfar, A. Poruba, M. Vaněček and J. Kočka. *Precise measurement of the deep defects and surface states in a-Si:H films by absolute CPM.* J. Non–Crystal. Solids, **200**, 304–308 (1996).

[121] D. Ritter and K. Weiser. *Suppression of interference fringes in absorption measurements on thin films.* Optics Communications, **57**, 336 (1986).

[122] M. Vaněček, A. Poruba, Z. Remeš, N. Beck and M. Nesládek. *Optical properties of microcrystalline materials.* J. Non–Crystal. Solids, **227–230**, 967–972 (1998).

[123] Martin Ledinský. *Strukturní a optoelektronické vlastnosti moderních materiálů pro tenkovrstvé sluneční články.* Master's thesis, Fyzikální ústav Univerzity Karlovy, Praha (2003).

[124] J. Gonzalez-Hernandez, G. H. Azarbayejani, R. Tsu and F. H. Pollak. *Raman, transmission electron microscopy, and conductivity measurements in molecular beam deposited microcrystalline Si and Ge - A comparative study.* Appl. Phys. Lett., **47**, 1350–1352 (1985).

[125] E. Bustarret, M. A. Hachicha and M. Brunel. *Experimental determination of the nanocrystalline volume fraction in silicon thin films from Raman spectroscopy.* Appl. Phys. Lett., **52**, 1675–1677 (1988).

[126] A. T. Voutsas, M. K. Hatalis, J. Boyce and A. Chiang. *Raman spectroscopy of amorphous and microcrystalline silicon films deposited by low-pressure chemical vapor deposition.* Journal of Applied Physics, **78**, 6999–7006 (1995).

[127] I. Gregora and V. Vorlíček. *Private communication.* Evaluation of Raman spectra of a–Si:H and μc–Si:H thin films. (1997).

[128] Ladislav Fekete. *Material for solar cells based on thin silicon films.* Master's thesis, Institute of Physics of Charles University, Prague (2004).

[129] M. Ledinský, J. Stuchlík, T. Mates, A. Fejfar and J. Kočka. *Characterization of mixed phase silicon by Raman spectroscopy.* J. Non-Crystal. Solids, **in press** (2006).

[130] V. Paillard, P. Puech, M.A. Laguna, P. Temple–Boyer, B. Caussat, J.P. Couderc and B. de Mauduit. *Resonant Raman scattering in polycrystalline silicon thin films.* Appl. Phys. Lett., **73**, 1718–1720 (1998).

[131] P. Lengsfeld, N.H. Nickel, Ch. Genzel and W. Fuhs. *Stress in undoped and doped laser crystallized poly-Si.* J. Appl. Phys., **91**(11), 9128–9135 (2002).

[132] Z. Iqbal, S. Vepřek, A.P. Webb and P. Capezzuto. *Raman scattering from small particle size polycrystalline silicon.* Solid State Comm., **37**, 993–996 (1981).

[133] Yoshihiko Kanemitsu. *Light emission from porous silicon and related materials.* Phys. Reports, **263**, 1–91 (1995).

[134] V. Paillard, P. Puech, M.A. Laguna, R. Carles, B. Kohn and F. Huisken. *Improved one-phonon confinement model for an accurate size determination of silicon nanocrystals.* J. Appl. Phys., **86**, 1921–1924 (1999).

[135] C. Droz, E. Vallat–Sauvain, J. Bailat, L. Feitknecht, J. Meier, X. Niquilleand and A. Shah. *Electrical and microstructural characterisation of microcrystalline silicon layers and solar cells.* In *Proceedings of the 3rd World Conference on Photovoltaic Energy Conversion*, Osaka, Japan (2003). WCPEC.

[136] V. Paillard, P. Puech, R. Sirvin, S. Hamma and P. Roca i Cabarrocas. *Measurement of the in-depth stress profile in hydrogenated microcrystalline silicon thin films using Raman spectrometry.* J. Appl. Phys., **90**, 3276–3279 (2001).

[137] S. Vepřek, Z. Iqbal and F.A. Sarott. *Rapid crystallization of amorphous silicon at room temperature.* Phil. Mag. B, **45**, 137 (1982).

[138] V. Valvoda, M. Polcarová and P. Lukáč. *Základy strukturní analýzy.* Univerzita Karlova, Praha, Czech Republic (1992).

[139] J. Matsui, M. Tsukiji, H. Saika, T. Toyama and H. Okamoto. *Infuence of substrate texture on the microstructure and photovoltaic performance of thin film polycrystalline silicon solar cells.* J. Non-Crystal. Solids, **299–302**, 1152–1156 (2002).

[140] H. P. Klug and L. E. Alexander. *X–ray diffraction procedure.* John Wiley & Sons, New York, USA (1974).

[141] S.P. Sen Gupta. *Evaluations of particle size and strain values from X–ray line breadths and line shapes in α-AgCd alloys.* Acta Cryst., **21**, 820–821 (1966).

[142] K. Knížek. *Kalvados - software for crystal structure and powder diffraction.* http://www.fzu.cz/~knizek/kalvados (2003).

[143] W.C. O'Mara, R.B. Herring and L.P. Hunt. *Handbook of semiconductor silicon technology.* Noyes, Park Ridge, New Jersey, USA (1990).

[144] Aleš Poruba. *Constant photocurrent method – study of optical properties of amorphous hydrogenated silicon prepared by microwave plasmas.* PhD thesis, Brno University of Technology, Czech Republic (1998).

[145] Micro Photonics Inc. *Supplier of advanced instrumentation for research.* http://www.microphotonics.com/Calotest.html (2004). CaloTest – product presentation.

[146] G. Binnig, C.F. Quate and Ch. Gerber. *Atomic force microscope.* Phys. Rev. Lett., **56**(9), 930–934 (1986).

[147] G. Binning, H. Rohrer, Ch. Gerber and E. Weibel. *Surface studies by scanning tunneling microscopy.* Phys. Rev. Lett., **49**(1), 57–61 (1982).

[148] G.H. Buh and J.J. Kopanski. *Atomic force microscope laser illumination effects on a sample and its application for transient spectroscopy.* Appl. Phys. Lett., **83**(12), 22 (2003).

[149] K.R. Bray and G.N. Parsons. *Surface transport kinetics in low-temperature silicon deposition determined from topography evolution.* Phys. Rev. B, **65**, 035311 (2001).

[150] S. J. Fang, S. Haplepete, W. Chen, C. R. Helms and Hal Edwards. *Analyzing atomic force microscopy images using spectral methods.* J. Appl. Phys., **82**, 5891–5898 (1997).

[151] P. Klapetek and I. Ohlídal. *Theoretical analysis of the atomic force microscopy characterization of columnar thin films.* Ultramicroscopy, **94**, 19–29 (2003).

[152] D. Nečas and P. Klapetek. *Gwyddion - a software framework for SPM data analysis.* http://gwyddion.net (2004).

[153] Kazuya Goto. *Studies on combined scanning capacitance/force microscopy.* PhD thesis, Department of Mechatronics and Presicion Engineering, Tohoku University, Japan (1998).

[154] B. Rezek, J. Stuchlík, A. Fejfar and J. Kočka. *Local characterization of electronic transport in microcrystalline silicon thin films with submicron resolution.* Appl. Phys. Lett., **74**(10), 1475–1477 (1999).

[155] Bohuslav Rezek. *Study of charge transport in amorphous and microcrystalline silicon with high lateral resolution.* PhD thesis, Faculty of Mathematics and Physics, Charles University, Prague, Czech Republic (2000).

[156] B. Rezek, J. Stuchlík, A. Fejfar and J. Kočka. *Microcrystalline silicon thin films studied by atomic force microscopy with electrical current detection.* J. Appl. Phys., **92**(1), 587 (2000).

[157] W.A. Hofer, A.S. Foster and A.L. Shugler. *Theories of scanning probe microscopes at the atomic scale.* Rev. Modern Phys., **75**, 1285 (2003).

[158] H. Fujiwara, M. Kondo and A. Matsuda. *Real-time spectroscopic ellipsometry studies of the nucleation and grain growth processes in microcrystalline silicon thin films.* Phys. Rev. B, **63**, 115306 (2001).

[159] J. Bailat, E. Vallat-Sauvain, L. Feitknecht, C. Droz and A. Shah. *Infuence of substrate on the microstructure of microcrystalline silicon layers and cells.* J. Non-Crystal. Solids, **299–302**, 1219–1223 (2002).

[160] J. Kočka, A. Fejfar, V. Vorlíček, H. Stuchlíková and J. Stuchlík. *Amorphous and Heterogeneous Silicon Thin Films: Fundamentals to Devices*, page 483. MRS Symp. Proc. **557**, San Francisco, USA (1999).

[161] A. Fejfar, T. Mates, B. Rezek, J. Stuchlík, V. Švrček, V. Vorlíček, K. Drbohlav, I. Pelant and J. Kočka. *Influence of crystallinity and grains on the transport properties of microcrystalline silicon.* In H. Scheer, B. McNelis, W. Palz, H.A. Ossenbrink and P. Helm, editors, *Proceedings of the 16th European photovoltaic Solar Energy Conference and Exhibition*, London, United Kingdom (2000). James & James.

[162] A. Fejfar, T. Mates, S. Honda, B. Rezek, J. Stuchlík, J. Kočka, J. Matějková, P. Hrnčiřík and J. Valenta. *Growth of microcrystalline grains in mixed phase silicon thin films for solar cells.* In *Proceedings of the 19th European Photovoltaic Solar Energy Conference and Exhibition*, volume II, page 1564, Paris, France (2004). WIP–Münich and ETA–Florence.

[163] A. Fejfar, T. Mates, C. Koch, B. Rezek, V. Švrček, P. Fojtík, H. Stuchlíková, J. Stuchlík and J. Kočka. *Amorphous and heterogeneous silicon-based films: microscopic aspects of charge transport in hydrogenated microcrystalline silicon*, page A16.1.1. MRS Symp. Proc. **664**, San Francisco, USA (2001).

[164] T. Mates, A. Fejfar, I. Drbohlav, B. Rezek, P. Fojtík, K. Luterová, J. Kočka, C. Koch, M.B. Schubert, M. Ito, K. Ro and H. Uyama. *Role of grains in protocrystalline silicon layers grown at very low substrate temperatures and studied by atomic force microscopy.* J. Non-Crystal. Solids, **299–302**, 767–771 (2002).

[165] R. Messier. *Toward qualification of thin film morphology.* J. Vac. Sci. Tech. A, **4**, 490–495 (1986).

[166] Ch. Ross, J. Herion, R. Carius and H. Wagner. *Nucleation and growth of low-temperature fine-crystalline silicon: a scanning probe microscopy and Raman spectroscopy study of the influence of hydrogen and different substrates.* Mat. Sci. Eng., **B72**, 1–6 (2000).

[167] A. Okabe, B. Boots and K. Sugihara, editors. *Spatial tessellations: Concepts and applications of Voronoi diagrams.* J. Wiley & Sons,, New York, USA (2000).

[168] R.W. Collins, A.S. Ferlauto, G.M. Ferreira, Chi Chen, Joohyun Koh, R.J. Koval, Yeeheng Lee, J.M. Pearce and C.R. Wronski. *Evolution of microstructure andphase in amorphous, protocrystalline, and microcrystalline silicon studied by real time spectroscopic ellipsometry.* Sol. Energy Mater. Sol. Cells, **78**, 143–180 (2003).

[169] J. Kočka, H. Stuchlíková, J. Stuchlík, V. Švrček B. Rezek, P. Fojtík, I. Pelant and A. Fejfar. *Microcrystalline silicon - relation of transport and microstructure.* Solid State Phenomena, **80–81**, 213–224 (2001).

[170] M.V. Chukichev, P.A. Forsch, W. Fuhs and A.G. Kazanskii. *Creation of metastable defects in microcrystalline silicon films by keV electron irradiation.* J. Non-Crystal. Solids, **337-340**, 378 (2004).

[171] T. Mates, P.C.P. Bronsveld, A. Fejfar, B. Rezek, J. Kočka, J.K. Rath and R.E.I. Schropp. *Detailed structural study of low temperature mixed-phase Si films by X–TEM and ambient conductive AFM.* J. Non-Crystal. Solids, **in press** (2006).

[172] D.M. Tanenbaum, A.L. Laracuente and A. Gallagher. *Surface roughening during plasma-enhanced chemical-vapor deposition of hydrogenated amorphous silicon on crystal silicon substrates.* Phys. Rev. B, **56**(7), 4243 (1997).

[173] B. Rezek, T. Mates, E. Šípek, J. Stuchlík, A. Fejfar and J. Kočka. *Influence of combined AFM/current measurement on local electronic properties of silicon thin films.* J. Non-Crystal. Solids, **299–302**, 360–364 (2002).

[174] B. Rezek, T. Mates, J. Stuchlík, J. Kočka and A. Stemmer. *Charge storage in undoped hydrogenated amorphous silicon by ambient atomic force microscopy.* Appl. Phys. Lett., **83**(9), 1764–1766 (2003).

[175] Tomáš Mates. *Unpublished results.* Combined AFM measurements on a–Si:H with memory effect (2001).

[176] H. Overhof, M. Otte, M. Schmidtke, U. Backhausen and R. Carius. *The transport mechanism in micro-crystalline silicon.* J. Non-Crystal. Solids, **227–230**, 992 (1998).

[177] K. Shimakawa. *Percolation-controlled electronic properties in microcrystalline silicon: effective medium approach.* J. Non-Crystal. Solids, **266–269**, 223–226 (2000).

[178] E. Vallat-Sauvain, U. Kroll, J. Meier, N. Wyrsch and A. Shah. *Microstructure and surface roughness of microcrystalline silicon prepared by very high frequency-glow discharge using hydrogen dilution.* J. Non-Crystal. Solids, **266–269**, 125–130 (2000).

[179] P.C.P. Bronsveld, J.K. Rath and R.E.I. Schropp. *Effect of hydrogen dilution on the structual and electronic properties of a–Si:H layers deposited at very low temperature (37° C).* In *Proceedings of the 19th European Photovoltaic Solar Energy Conference and Exhibition*, page 3DV.1.61, Paris, France (2004). WIP–Münich and ETA–Florence.

[180] J. Kočka, H. Stuchlíková, J. Stuchlík, B. Rezek, T. Mates, V. Švrček, P. Fojtík, I. Pelant and A. Fejfar. *Model of transport in microcrystalline silicon.* J. Non-Crystal. Solids, **299–302**, 355–359 (2002).

[181] C. Boehme and K. Lips. *A pulsed EDMR study of hydrogenated microcrystalline silicon at low temperatures.* phys. stat. sol. (c), **1**, 1255–1274 (2004).

[182] J. Musil, J. Vyskočil and S. Kadlec. *Hard coatings.* Academia, Prague, Czech Republic (1992).

[183] K.S. Stevens and N.M. Johnson. *Intrinsic stress in hydrogenated amor hous silicon deposited with a remote hydrogen plasma.* J. Appl. Phys., **71**, 2628 (1992).

[184] A.J.M.M. van Zutphen, P. Šutta, F.D. Tichelaar, A. von Keitz, M. Zeman and J.W. Metselaar. *Structure of thin polycrystalline silicon films on ceramic substrates.* J. Cryst. Growth, **223**(3), 332–340 (2001).

[185] M.M. de Lima Jr., R.G. Lacerda, J. Vilcarromero and F.C. Marques. *Coefficient of thermal expansion and elastic modulus of thin films.* J. Appl. Phys., **86**(9), 4936–4932 (1999).

[186] A. Dargys and J. Kundrotas. *Handbook on physical properties of Ge, Si, GaAs and InP.* Science and Encyclopedia Publishers, Vilnius, Lithuania (1994).

[187] S. Veprek, F.A. Sarott and Z. Iqbal. *Effect of grain boundaries on the Raman spectra, optical absorption and elastic light scattering in nanometer–sized crystalline silicon.* Phys. Rev. B, **36**(6), 3344–3350 (1987).

[188] H. Fujiwara, M. Kondo and A. Matsuda. *Stress–induced nucleation of microcrystalline silicon from amorphous phase.* Jpn. J. Appl. Phys., **41**, 2821–2828 (2002).

[189] O. Madelung and M. Schulz. *Landboldt-Börnstein, Numerical data and functional relationships in science and technology*, volume 22 of *Semiconductors.* Springer–Verlag, Berlin, Germany (1987).

[190] D.R. Lide (ed.). *Chemical Rubber Company handbook of chemistry and physics*, volume 79th edition of *accessed via www.webelements.com.* CRC Press, Boca Raton, Florida, USA (1998).

[191] Präzisions Glas & Optik GmbH, Iserlohn, Germany. *Producer of optical materials.* http://www.pgo-online.com (2003). Products – Technical glass – Sheet glass & Flat glass – 7059.

[192] F. Jansen, M.A. Machonkin, N. Palmieri and D. Kuhman. *Thermal expansion and elastic properites of plasma–deposited amorphous silicon and silicon oxide films.* Appl. Phys. Lett., **50**, 16 (1987).

[193] J. Kočka, T. Mates, H. Stuchlíková, J. Stuchlík and A. Fejfar. *Characterization of grain growth, nature and role of grain boundaries in microcrystalline silicon – review of typical features.* Thin Sol. Films, **501**, 107 (2006).

[194] T. Mates, M. Ledinský, K. Luterová, P. Fojtík, Ha Stuchlíková, A. Fejfar, J. Kočka, M. Ito, K. Ro and H. Uyama. *Structure and properties of thin silicon films deposited at very low substrate temperatures.* In *PV in Europe Conference and Exhibition: From PV Technology to Energy Solutions*, Rome, Italy (2002). WIP–Münich and ETA–Florence.

[195] L. Li, Y-M. Li, J.A. Anna Selvan, A.E. Delahoy and R.A. Levy. *Correlations between structural properties and performance of microcrystalline silicon solar cells fabricated by conventional RF-PECVD.* J. Non-Crystal. Solids, **347**, 106–113 (2004).

[196] J.K. Rath, H. Meiling and R.E.I. Schropp. *Low–temperature deposition of polycrystalline silicon thin films by hot–wire CVD.* Sol. Energy Mater. Sol. Cells, **48**, 269 (1997).

[197] A. Fejfar, T. Mates, P. Fojtík, M. Ledinský, K. Luterová, H. Stuchlíková, I. Pelant, J. Kočka, V. Baumruk, A. Macková, M. Ito, K. Ro and H. Uyama. *Structure and properties of silicon thin films deposited at low substrate temperatures.* Jpn. J. Appl. Phys., **42**, L987–L989 (2003).

[198] J. Schwarzkopf, B. Selle, W. Bohne, J. Röhrich, I. Sieber and W. Fuhs. *Disorder in silicon films grown epitaxially at low temperature.* J. Appl. Phys., **93**(9), 5215–5221 (2003).

[199] J. Kočka, T. Mates, S. Honda, M. Ledinský, K. Luterová, H. Stuchlíkovva, J. Stuchlík and A. Fejfar. *Effect of hydrogen and crystallinity on transport properties of microcrystalline silicon.* In *Proceedings of the 19th European Photovoltaic Solar Energy Conference and Exhibition*, volume II, page 1371, Paris, France (2004). WIP–Münich and ETA–Florence.

[200] J. Kočka, T. Mates, M. Ledinský, K. Luterová, H. Stuchlíková, J. Stuchlík, A. Poruba and A. Fejfar. *Properties of microcrystalline silicon prepared at high growth rate and the new way how to increase nucleation.* In *Proceedings of the 20th European Photovoltaic Solar Energy Conference and Exhibition*, page 3DV.3.30, Barcelona, Spain (2005). WIP–Münich and ETA–Florence.

[201] J. Kočka, T. Mates, M. Ledinský, H. Stuchlíková, J. Stuchlík and A. Fejfar. *Transport properties of microcrystalline silicon prepared at high growth rate.* J. Non-Crystal. Solids, **in press** (2006).

[202] J. Kočka, T. Mates, M. Ledinský, H. Stuchlíková, J. Stuchlík and A. Fejfar. *Detail characterization of the properties of microcrystalline silicon prepared at high growth rate.* In *Proceedings of the 4rd World Conference on Photovoltaic Energy Conversion*, Waikoloa, Hawaii, USA (2006). WCPEC.

[203] J. Kočka, J. Stuchlík, H. Stuchlíková, V. Švrček, P. Fojtík, T. Mates, K. Luterová and A. Fejfar. *Amorphous/microcrystalline silicon superlattices - the chance to control isotropy and other transport properties.* Appl. Phys. Lett., **79**(16), 2540–2542 (2002).

[204] S. Honda, T. Mates, M. Ledinský, J. Oswald, A. Fejfar, J. Kočka, T. Yamazaki, Y. Uraoka and T. Fuyuki. *Effect of hydrogen passivation on polycrystalline silicon thin films.* Thin Sol. Films, **487**, 152 (2005).

About the author

Curriculum Vitae

Personal data

Name:	Tomáš Mates
Date of birth:	29th November 1975
Place of birth:	Pilsen, Czech Republic
Nationality:	czech
e-mail:	mates@fzu.cz
www:	http://www.fzu.cz/~mates

Education

1999–2006	Post-graduate studies at the Faculty of Mathematics and Physics, Charles University in Prague. (specialization: Electronics and vacuum physics) PhD thesis on *Structure and properties of thin silicon films for solar cells.*
1994–1999	Graduate studies at the Faculty of Applied Sciences, University of West Bohemia in Pilsen, engineer degree 'Ing.'. (specialization: Physics of plasma and thin films.) Master thesis on *Deposition of thin silicon films by magnetron sputtering.*
1994–1999	"English for engineering professions" (5 years' course for the students of technical faculties).
1996–1998	"Pedagogical minimum" (2 years' course for the students of technical faculties).

Research interests

- Structure and electrical properties of amorphous and microcrystalline silicon thin films, application to solar cells.
- Atomic force microscopy and related scanning probe techniques.
- Preparation of thin films by PECVD and sputtering.

Work experience

since 1999	Research worker at Department of Thin Films, Institute of Physics, Academy of Sciences of the Czech Republic, Prague.

Languages

Czech, English, German

List of Publications

Impacted scientific journals

1. T. Mates, P.C.P. Bronsveld, A. Fejfar, B. Rezek, J. Kočka, J.K. Rath, R.E.I. Schropp, *Detailed structural study of low temperature mixed-phase Si films by X-TEM and ambient conductive AFM*, Journal of Non-Crystalline Solids (2006) in press

2. M. Ledinský, J. Stuchlík, T. Mates, A. Fejfar, J. Kočka, *Characterization of mixed phase silicon by Raman spectroscopy*, Journal of Non-Crystalline Solids (2006) in press

3. J. Kočka, T. Mates, M. Ledinský, H. Stuchlíková, J. Stuchlík, A. Fejfar, *Microcrystalline silicon prepared at magnetic field modified nucleation*, Journal of Non-Crystalline Solids (2006) in press

4. J. Kočka, T. Mates, M. Ledinský, H. Stuchlíková, J. Stuchlík, A. Fejfar, *Transport properties of microcrystalline silicon prepared at high growth rate*, Journal of Non-Crystalline Solids (2006) in press

5. S. Honda, T. Mates, M. Ledinský, A. Fejfar, J. Kočka, T. Yamazaki, Y. Uraoka, T. Fuyuki, H. Boldyryeva, A. Macková and V. Peřina, *Defects generation by hydrogen passivation of polycrystalline silicon thin films*, Solar Energy (2006) in press

6. H. Boldyryeva, S. Honda, A. Macková, T. Mates, A. Fejfar, J. Kočka, *Characterization of hydrogen contained in passivated poly-Si and microcrystalline-Si by ERDA technique*, Surface and Interface Analysis **38**, 819 (2006).

7. J. Kočka, T. Mates, H. Stuchlíkovva, J. Stuchlík, A. Fejfar, *Characterization of grain growth, nature and role of grain boundaries in microcrystalline silicon – review of typical features*, Thin Solid Films **501**, 107 (2006).

8. S. Honda, T. Mates, K. Knížek, M. Ledinský, A. Fejfar, J. Kočka, T. Yamazaki, Y. Uraoka, T. Fuyuki, *Hydrogenation of polycrystalline silicon thin films*, Thin Solid Films **501**, 144 (2006).

9. I. Pelant, T. Ostatnický, J. Valenta, K. Luterová, E. Skopalová, T. Mates, R.G. Elliman, *Waveguide cores containing silicon nanocrystals as active spectral filters for silicon-based photonics*, Applied Physics B: Lasers and Optics, **83**, 87 (2006)

10. A. Fejfar, J. Stuchlík, T. Mates, M. Ledinský, S. Honda, J. Kočka, *Patterning of hydrogenated microcrystalline silicon growth by magnetic field*, Applied Physics Letters **87**, 011901 (2005).

11. S. Honda, T. Mates, M. Ledinský, J. Oswald, A. Fejfar, J. Kočka, T. Yamazaki, Y. Uraoka, T. Fuyuki *Effect of hydrogen passivation on polycrystalline silicon thin films*, Thin Solid Films **487**, 152 (2005).

12. J. Kočka, T. Mates, P. Fojtík, M. Ledinský, K. Luterová, H. Stuchlíková, J. Stuchlík, I. Pelant, A. Fejfar, M. Ito, K. Ro, H. Uyama, *Formation of Microcrystalline Silicon at Low Temperatures and Role of Hydrogen*, Journal of Non-Crystalline Solids **338–340**, 287 (2004).

13. A. Fejfar, T. Mates, O. Čertík, B, Rezek, J. Stuchlík, I. Pelant, J. Kočka, *Model of Electronic Transport in Microcrystalline Silicon and Its Use for Prediction of Device Performance*, Journal of Non-Crystalline Solids **338–340**, 303 (2004).

14. J. Kočka, A. Fejfar, T. Mates, P. Fojtík, K. Dohnalová, K. Luterová, J. Stuchlík, H. Stuchlíková, I. Pelant, B. Rezek, A. Stemmer, M. Ito, *The physics and technological aspects of the transition from amorphous to microcrystalline and polycrystalline silicon*, physica status solidi (c) **1**, 1097 (2004).

15. K. Luterová, V. Švrček, T. Mates, M. Ledinský, M. Ito, A. Fejfar, J. Kočka *Thin silicon films deposited at low substrate temperatures studied by surface photovoltage technique*, Thin Solid Films **451-452**, 408 (2004).

16. M. Ito, K. Ro, S. Yoneyama, Y. Ito, H. Uyama, T. Mates, M. Ledinský, K. Luterová, P. Fojtík, H. Stuchlíková, A. Fejfar, J. Kočka *Silicon thin films deposited at very low substrate temperatures*, Thin Solid Films **442**, 163 (2003).

17. B. Rezek, T. Mates, J. Stuchlík, J. Kočka, A. Stemmer *Charge storage in undoped hydrogenated amorphous silicon by ambient atomic force microscopy*, Applied Physics Letters **83**, 1764 (2003).

18. A. Fejfar, T. Mates, P. Fojtík, M. Ledinský, K. Luterová, H. Stuchlíková, I. Pelant, J. Kočka, V. Baumruk, A. Macková, M. Ito, K. Ro, H. Uyama *Structure and properties of silicon thin films deposited at low substrate temperatures*, Japanese Journal of Applied Physics **42**, L987 (2003).

19. J. Kočka, A. Fejfar, H. Stuchlíková, J. Stuchlík, P. Fojtík, T. Mates, B. Rezek, K. Luterová, V. Švrček, I. Pelant, *Basic features of transport in microcrystalline silicon*, Solar Energy Materials and Solar Cells **78**, 493 (2003).

20. P. Fojtík, K. Dohnalová, T. Mates, J. Stuchlík, I. Gregora, J. Chval, A. Fejfar, J. Kočka, I. Pelant, *Rapid crystallization of amorphous silicon at room temperature*, Philosophical Magazine B **82**, 1785 (2002).

21. T. Mates, A. Fejfar, I. Drbohlav, B. Rezek, P. Fojtík, K. Luterová, J. Kočka, C. Koch, M.B. Schubert, M. Ito, K. Ro, H. Uyama, *Role of Grains in Protocrystalline Silicon Layers Grown at Very Low Substrate Temperatures and Studied by Atomic Force Microscopy*, Journal of Non-Crystalline Solids **299–302**, 767 (2002).

22. B. Rezek, T. Mates, E. Šípek, J. Stuchlík, A. Fejfar, J. Kočka, *Influence of Combined AFM/Current Measurement on Local Electronic Properties of Silicon Thin Films*, Journal of Non-Crystalline Solids **299–302**, 360 (2002).

23. V. Švrček, A. Fejfar, P. Fojtík, T. Mates, A. Poruba, H. Stuchlíková, I. Pelant, J. Kočka, Y. Nasuno, M. Kondo, A. Matsuda, *Importance of the Transport Isotropy in mc-Si:H Thin Films for Solar Cells Deposited at Low Substrate Temperatures*, Journal of Non-Crystalline Solids **299–302**, 395 (2002).

24. J. Kočka, H. Stuchlíková, J. Stuchlík, B. Rezek, T. Mates, V. Švrček, P. Fojtík, I. Pelant, A. Fejfar, *Model of Transport in Microcrystalline Silicon*, Journal of Non-Crystalline Solids **299–302**, 355 (2002).

25. J. Kočka, J. Stuchlík, H. Stuchlíková, V. Švrček, P. Fojtík, T. Mates, K. Luterová, A. Fejfar, *Amorphous/microcrystalline silicon superlattices – the chance to control isotropy and other transport properties*, Applied Physics Letters **79**, 2540 (2001).

Conference proceedings

26. A. Fejfar, T. Mates, B. Rezek, J. Stuchlík, V. Švrček, V. Vorlíček, K. Drbohlav, I. Pelant, J. Kočka, *Influence of Crystallinity and Grains on the Transport Properties of Microcrystalline Silicon*, Proceedings of the 16th European photovoltaic Solar Energy Conference and Exhibition, Glasgow, 1.-5. 5. 2000 (editors H. Scheer, B. McNelis, W. Palz, H.A. Ossenbrink and P. Helm) **1**, 470 (2000) James & James, London, United Kingdom.

27. A. Fejfar, T. Mates, C. Koch, B. Rezek, V. Švrček, P. Fojtík, H. Stuchlíková, J. Stuchlík, J. Kočk, *Microscopic Aspects Of Charge Transport In Hydrogenated Microcrystalline Silicon*, Proceedings of Mat. Res. Soc. Symp., Amorphous and Heterogeneous Silicon-Based Films, March 2001 (editors J.B. Joyce, J.D. Cohen, R.W. Collins, J. Hanna, M. Stutzman) **664**, A16.1.1 (2001) MRS Warrendale, San Francisco, USA.

28. J. Kočka, H. Stuchlíková, J. Stuchlík, B. Rezek, T. Mates, V. Švrček, P. Fojtík, I. Pelant, A. Fejfar, *Microcrystalline silicon - critical points of model of transport*, Technical Digest of the Review meeting for research with overseas country research institutes, 2. 2. 2001, p. 27 (2001) NEDO, Tokyo, Japan.

29. J. Kočka, H. Stuchlíková, J. Stuchlík, B. Rezek, T. Mates, A. Fejfar, *Role of Grain Boundaries in Model of Transport in μc-Si:H*, Technical Digest of the International PVSEC - 12, April 2001, p. 469 (2001) Jeju, Korea.

30. A. Fejfar, H. Stuchlíková, J. Stuchlík, T. Mates, P. Fojtík, V. Švrček, K. Luterová, B. Rezek, I. Pelant, J. Kočka, *Model of charge transport in hydrogenated microcrystalline silicon*, Proceedings of the 17th European Photovoltaic Solar Energy Conference, Münich, 22.-26. 10. 2001 (editors B. McNelis, W. Palz, H.A. Ossenbrink and P. Helm) **3**, 2880 (2002) WIP-Münich and ETA-Florence, Germany.

31. T. Mates, M. Ledinský, K. Luterová, P. Fojtík, Ha Stuchlíková, A. Fejfar, J. Kočka, M. Ito, K. Ro, H. Uyama, *Structure and Properties of Thin Silicon Films Deposited at Very Low Substrate Temperatures*, Proceedings of the PV in Europe Conference and Exhibition: From PV Technology to Energy Solutions, Rome, 7.-11. 10. 2002, WIP-Münich and ETA-Florence, Italy.

32. T. Mates, A. Fejfar, M. Ledinský, K. Luterová, P. Fojtík, H. Stuchlíková, I. Pelant, J. Kočka, A. Macková, M. Ito, K. Ro, H. Uyama, *Effect of Substrate*

Temperature and Hydrogen dilution on Thin Silicon Films Deposited at Low Substrate Temperatures, Proceedings of the 3rd World Conference on Photovoltaic Energy Conversion, Osaka, 11.-18. 5. 2003, WCPEC-3, Japan.

33. A. Fejfar, T. Mates, S. Honda, B. Rezek, J. Stuchlík, J. Kočka, J. Matějková, P. Hrnčiřík, J. Valenta, *Growth of Microcrystalline Grains in Mixed Phase Silicon Thin Films For Solar Cells*, Proceedings of the 19th European Photovoltaic Solar Energy Conference, Paris, 7.-11. 6. 2004, 3DV.1.49, II, 1564 (2004) WIP-Münich and ETA-Florence, Germany.

34. J. Kočka, T. Mates, S. Honda, M. Ledinský, K. Luterová, H. Stuchlíkovva, J. Stuchlík, A. Fejfar, *Effect of Hydrogen and Crystallinity on Transport Properties of Microcrystalline Silicon*, Proceedings of the 19th European Photovoltaic Solar Energy Conference, Paris, 7.-11. 6. 2004, 3AO.7.6, II, 1371 (2004) WIP-Münich and ETA-Florence, Germany.

35. J. Kočka, T. Mates, M. Ledinský, K. Luterová, H. Stuchlíková, J. Stuchlík, A. Poruba, A. Fejfar, *Properties of Microcrystalline Silicon Prepared at High Growth Rate and the New Way How to Increase Nucleation*, Proceedings of the 20th European Photovoltaic Solar Energy Conference, Barcelona, 6.-10. 6. 2005, 3DV.3.30 (2005) WIP-Münich and ETA-Florence, Germany.

36. M. Ledinskyl, L. Feketel, S. Hondal, T. Matesl, A. Fejfarl, J. Kockal, *Evaluation of crystallinity of mixed phase silicon thin films from Raman scattering spectra*, Proceedings of the 20th General Conference, Condensed Matter Division of the European Physical Society, Prague, 19.-23.7. 2004, S4Y107 (2004) CMD EPS, Czech Republic.

37. H. Stuchlíková, J. Stuchlík, T. Mates, M. Ledinský, A. Fejfar, J. Kočka, *Magnetic Field – Important Factor for the Growth of Thin Films of Microcrystalline Silicon*, Proceedings of the 17th International Symposium on Plasma Chemistry, Toronto, 8.-12. 8. 2005, ISPC-17, Canada.

38. J. Kočka, T. Mates, M. Ledinský, H. Stuchlíková, J. Stuchlík, A. Fejfar, *Properties of Microcrystalline Silicon Prepared at High Growth Rate*, Proceedings of the 4th World Conference on Photovoltaic Energy Conversion, Waikoloa, 7.-12. 5. 2006, WCPEC-4, Hawaii.

39. A. Hospodková, V. Křápek, T. Mates, K. Kuldová, J. Pangrác, E. Hulicius, J. Oswald, K. Melichar, J. Humlíček, T.Šimeček, *Lateral shape of InAs/GaAs*

quantum dots in vertically correlated structures, Proceedings of the 13th International Conference on Metal Organic Vapor Phase Epitaxy, Miyazaki, 22.-26. 5. 2006, ICMOVPE-13, Japan.

Czech scientific journals

40. B. Rezek, A. Fejfar, T. Mates, J. Stuchlík, J. Kočka, *Studium transportu náboje v mikrokrystalickém křemíku s vysokým prostorovým rozlišením*, Československý časopis pro fyziku **1**, 62 (2001).

41. P. Fojtík, I. Pelant, A. Fejfar, B. Rezek, T. Mates, J. Kočka, *Luminiscence buzená hrotem rastrovacího tunelovacího mikroskopu*, Československý časopis pro fyziku **1**, 4 (2002).

42. T. Mates, A. Fejfar, I. Drbohlav, B. Rezek, P. Fojtík, K. Luterová, J. Kočka, C. Koch, M.B. Schubert, M. Ito M., K. Ro, H. Uyama, *Studium struktury a růstu nízkoteplotního protokrystalického křemíku pomocí AFM mikroskopu*, Československý časopis pro fyziku **2**, 93 (2003).

43. P. Fojtík, F. Charra, A. Svoboda, T. Mates, A. Fejfar, J. Kočka, I. Pelant, *Experimentální aspekty luminiscence/fotonové emise buzené hrotem STM*, Československý časopis pro fyziku **2**, 113 (2003).

Czech conference proceedings

44. A. Fejfar, B. Rezek, J. Stuchlík, H. Stuchlíková, V. Švrček, P. Fojtík, T. Mates, I. Pelant, J. Kočka, *Transport elektrického náboje v mikrokrystalickém křemíku pro sluneční články*, Sborník ze semináře OS Polovodiče FVS JČMF, Liblice, 31.1. - 2.2. 2000 (editor E. Hulicius), p. 84, FZÚ AV ČR, Praha (2000).

45. K. Dohnalová, P. Fojtík, T. Mates, J. Stuchlík, I. Gregora, J. Kočka, I.Pelant, *Nová levná metoda niklem indukované krystalizace a-Si:H za pokojové teploty*, Sborník z konference Juniormat'01, Brno, 19.-20. 9. 2001, p. 154, FSI VUT, Brno (2001).

46. T. Mates, A. Fejfar, I. Drbohlav, B. Rezek, P. Fojtík, K. Luterová, J. Kočka, C. Koch, M. B. Schubert, M. Ito, K. Ro, H. Uyama *Grains in Protocrystalline Silicon Grown at Very Low Substrate Temperature* Proceedings of the International

Summer School – Role of Physics in Future Applications: From Nanotechnology to Macroelectronics, Tři Studně, 10.-15. 6. 2002, (editors J. Švec, A. Fejfar), FZÚ AV ČR, Praha (2002).

47. T. Mates, A. Fejfar, B. Rezek, P. Fojtík, I. Drbohlav, K. Luterová, I. Pelant a J. Kočka, *Studium mikrokrystalického křemíku pomocí kombinovaného AFM mikroskopu*, Sborník ze 14. konference českých a slovenských fyziků, 9.-12. 9. 2002 (editors P. Baroch, M. Kubásek, Š. Potocký), p. 363, FAV ZČU, Plzeň (2002).

48. T. Mates, A. Fejfar, M. Ledinský, K. Luterová, P. Fojtík, H. Stuchlíková, J. Stuchlík, S. Honda, J. Florian, B. Rezek, I. Drbohlav, I. Pelant, J. Kočka *Role of nano-grain boundaries in thin (local conductivity and topography) Si films discovered by combined AFM* Proceedings of the International Summer School – Science and Technology at Nanoscale, Tři Studně, 6.-11. 6. 2005, (editors A. Vetushka, A. Fejfar), FZÚ AV ČR, Praha (2005).

Unpublished conference contributions

49. A. Fejfar, T. Mates, B. Rezek, J. Stuchlík, V. Švrček, V. Vorlíček, K. Drbohlav, I. Pelant, J. Kočka, *Influence of crystallinity and grains on the transport properties of microcrystalline silicon*, presented at NATO Advanced Study Institute, Properties and Applications of Amorphous Materials, 25. 6.-7. 7. 2000, Seč, Iron Mountains, Czech Republic.

50. A. Fejfar, A. Poruba, B. Rezek, T. Mates, H. Stuchlíková, J. Stuchlík, M. Vaněček, J. Kočka, *Growth, Structure and Transport Properties of Hydrogenated Microcrystalline Silicon for Solar Cells*, presented at the Flemish-Hungarian Workshop "Advanced concepts for low-thermal budget processing of crystalline Si solar cells", 13.-14. 3. 2001, IMEC, Leuven, Belgium.

51. P. Fojtík, K. Dohnalová, T. Mates, J. Stuchlík, I. Gregora, J. Chval, K. Knížek, J. Kočka, I. Pelant, *Electric Field Induced Crystallization of Ni-covered Hydrogenated Amorphous Silicon at Room Temperature*, presented at the 19th International Conference on Amorphous and Microcrystalline Semiconductors, 27.-31. 8. 2001, Nice, France.

52. T. Mates, A. Fejfar, P. Fojtík, K. Luterová, M. Ledinský, K. Dohnalová, M. Dienstbier, I. Pelant, J. Kočka, *Zrna v tenkých vrstvách mikrokrystalického*

křemíku studovaná kombinovanou AFM mikroskopií, prezentováno na Národní konferenci NANO'02, 19-21. 11. 2002, FSI VUT, Brno.

53. J. Kočka, T. Mates, M. Ledinský, H. Stuchlíková, A. Fejfar, *Role of grain boundaries in microcrystalline silicon*, presented at 2nd aSiNet Workshop on Thin Silicon held jointly with 9th Euroregional Workshop on Thin Silicon Devices, 19.-21. 2. 2003, Lisbon, Portugal.

54. P. Fojtík, K. Dohnalová, T. Mates, J. Stuchlík, A. Fejfar, J. Kočka, I. Pelant, *Room Temperature Electric Field Induced Crystallization of Hydrogenated Amorphous Silicon*, presented at 2nd aSiNet Workshop on Thin Silicon held jointly with 9th Euroregional Workshop on Thin Silicon Devices, 19.-21. 2. 2003, Lisbon, Portugal.

55. T. Mates, B. Rezek, P. Fojtík, I. Drbohlav, M. Ledinský, K. Luterová, K. Dohnalová, H. Stuchliková, J. Stuchlík, S. Honda, L. Fekete, A. Fejfar, J.Kočka, *Structure and Properties of Thin Silicon Films Deposited at Low Substrate Temperatures*, presented at 3rd aSiNet Workshop on Thin Silicon, 25.-27. 2. 2004, Bratislava, Slovak Republic.

56. T. Mates, A. Fejfar, M. Ledinský, K. Luterová, P. Fojtík, H. Stuchlíková, J. Stuchlík, S. Honda, J. Florian, B. Rezek, I. Drbohlav, I. Pelant, J. Kočka *Role of nano-grain boundaries in thin (local conductivity and topography) Si films discovered by combined AFM*, East European Workshop, A*Star Institute, 16.-20. 11. 2005, Singapore.

57. T. Mates, A. Fejfar, I. Drbohlav, B. Rezek, S. Honda, L. Fekete, J. Florian, J. Kočka, *Artefakty v topografii a lokální vodivosti při měření mikrokrystalického křemíku kombinovaným AFM mikroskopem*, zvaná přednáška na 4. konferenci o metodách blízkého pole, 4.-6. 10. 2005, Lázně Bohdaneč.

58. T. Mates, A. Fejfar, I. Drbohlav, B. Rezek, S. Honda, L. Fekete, J. Florian, J. Kočka, *Artefacts in topography and local conductivity in the measurements of thin Si films by AFM*, invited talk to International workshop of Czech Metrology Institute, 21.-22. 3. 2005, ČMI Brno

To be published...

59. P.C.P. Bronsveld, T. Mates, A. Fejfar, B. Rezek, J. Kočka, J.K. Rath, R.E.I. Schropp, *Internal structure of mixed phase hydrogenated silicon thin films made at 39° C*, accepted for publication in Applied Physics Letters (2006).

60. A. Hospodková, E. Hulicius, J. Oswald, J. Pangrác, T. Mates, K. Kuldová, T.Šimeček, K. Melichar, *Properties of MOVPE InAs/GaAs quantum dots overgrown by InGaAs*, to appear in Journal of Crystal Growth (2006).

Author's participation in the publications:

The author prepared the publications 1, 21 and 31 in a cooperation with Dr. A. Fejfar, publication 32 in a cooperation with Dr. Jan Kočka and publication 42 in a cooperation with prof. Ivan Pelant. The author took an active part in the experiments and preparations of all the other publications in the list given above.

The author presented the results at several local (42, 46, 47, 48, 52) and international conferences (1, 31, 55 - oral presentations, 21, 32, 56 - poster presentations), obtained 3 best poster awards (29, 33, 35) and gave 2 invited talks (57, 58).